EFFECT OF PCM SELECTION ON THE THERMAL PERFORMANCE OF A COIL-IN-SHELL STORAGE SYSTEM

by

Ryan L. Callaghan
Submitted in partial fulfillment of the requirements
for the degree of Master of Applied Science

at

Dalhousie University
Halifax, Nova Scotia
December 2023

Dalhousie University is located in Mi'kma'ki,
the ancestral and unceded territory of the Mi'kmaq.
We are all Treaty people.

DEDICATION PAGE

This thesis is dedicated to my mother, father, brothers and to my loving partner, Shannon, who have provided moral, emotional and financial support throughout the entirety of this process and who have inspired me to push forward even when I didn't think I could.

Table of Contents

List of Tables vii

List of Figures viii

Abstract xii

List of Abbreviations Used xiii

Acknowledgements xvi

Chapter 1: Introduction 1

1.1 Background on Thermal Energy Storage 1

1.2 Research Objectives 3

1.3 Organization of Thesis 3

Chapter 2: Literature Review 5

2.1 Latent Heat Thermal Energy Storage Systems 5

2.2 Working Principles of LHTES Systems 5

2.2.1 Charging 5

2.2.2 Discharging 6

2.3 Types of PCM Used 6

2.3.1 Organics 7

2.3.2 Inorganics 10

2.3.3 Eutectics 11

2.4 Common Heat Exchanger Geometries Employed 11

2.4.1 Shell-and-tube 12

2.4.2 Packed bed 15

2.4.3 Plate type heat exchangers 16

2.5 Container Materials for LHTES systems 16

2.6 Techniques for Improving Heat Transfer for PCM Heat Exchangers 17
2.6.1 Nano-enhanced PCM 17
2.6.2 Metal foam 18
2.6.3 Fins 18
2.6.4 Orientation 19
2.6.5 Eccentricity 19
2.7 Key Operating Parameters to study in LHTES systems 19
2.7.1 Inlet temperature 19
2.7.2 Flow rate 20
2.8 Characterization of PCM Heat Exchangers 20
2.9 Key Performance Indicators for LHTES systems 22
2.9.1 ε-NTU Method 22
2.9.2 Dimensionless numbers 27
2.9.3 *UA* Approach 28
2.9.4 Normalized Power 29
2.9.5 Other Performance Indicators 30
2.10 Conclusion 31
Chapter 3: Experimental Setup and Procedure 33
3.1 Materials 33
3.1.1 Phase Change Material Selection 33
3.1.2 Phase Change Material Properties 35
3.2 Heat Exchanger Design 37
3.2.1 Container 37
3.2.2 Coil Design 37
3.2.3 Insulation 40

3.3 Workbench and HTF Setup 40
3.3.1 Circulating Thermal Bath 42
3.3.2 HTF Loop 42
3.3.3 Booster Pump 43
3.4 Sensors 43
3.4.1 Temperature Measurement 43
3.4.2 Flow Rate Measurement 45
3.4.3 Temperature Measurement Calibration 45
3.4.4 Data Acquisition 46
3.5 Experimental Procedure 47
3.5.1 Experimental Operating Parameters 48
3.6 Power and Energy Calculations 50
3.6.1 Power 50
3.6.2 Heat Loss/Gain 50
3.6.3 Energy 52
3.6.4 Uncertainty Analysis 52
3.7 Experiment Repeatability 55
3.8 Conclusion 55
Chapter 4: Dodecanoic Acid Results 60
4.1 Temperature Results 60
4.2 Charging Results 62
4.3 Discharging Results 65
4.4 High Flow Rate Results 67
4.5 Theoretical Energy Storage Capacity 71
4.6 Conclusion 72

Chapter 5: 1-Octadecanol Results....73
5.1 Temperature Results....73
5.2 Charging Results....75
5.3 Discharging Results....78
5.4 Theoretical Energy Storage Capacity....80
5.5 Conclusion....80
Chapter 6: PCM Comparison and Data Reduction....82
6.1 Charging Results....82
6.2 Discharging Results....87
6.3 Energy Profiles....90
6.4 Data Reduction Approaches....92
6.4.1 Effectiveness-NTU approach....92
6.4.2 Comparing discharging results using Fourier number....92
6.4.3 Comparison of PCMs using Nusselt number....95
6.4.4 Comparison of PCMs using average power over total energy stored/discharged....97
6.4.5 Comparison of PCMs using normalized average power over total energy stored/discharged....100
6.5 Conclusion....103
Chapter 7: Conclusion....105
References....109
Appendix-A Engineering Drawings....117
Appendix-B Equipment Data Sheets....119
Appendix-C Copyright License....134

List of Tables

Table 2.1: Types of PCM Advantages and Disadvantages 8
Table 2.2: Experimental characterization studies of PCM Heat Exchangers 23
Table 2.3: Numerical characterization studies of PCM Heat Exchangers 24
Table 3.1: Comparison of PCM found in literature to dodecanoic acid (green: high deviation, yellow: intermediate deviation, red: poor deviation) 34
Table 3.2: Thermophysical Properties of dodecanoic acid (Desgrosseilliers *et al.*, 2013) and 1-octadecanol (Kahwaji *et al.*, 2017b; Yaws, 2003) 36
Table 3.3: Calibration values for thermocouples and RTDs 46
Table 3.4: List of experiments run for both PCMs 49
Table 4.1: Theoretical vs experimental energy stored for dodecanoic acid 72
Table 5.1 Theoretical vs experimental energy stored for 1-ocatdecanol 81

List of Figures

Figure 2.1: Cylindrical shell-and-tube PCM heat exchangers (Zayed *et al.*, 2020) 12
Figure 2.2: Triplex tube with longitudinal fins (Mat et al., 2013) 13
Figure 2.3: Helical tube geometry (Wołoszyn *et al.*, 2021).....14
Figure 2.4: Packed bed LHTES with spherical capsules (Amin et al., 2014).....15
Figure 2.5: Plate-and-frame heat exchanger (Medrano *et al.*, 2009) 16
Figure 3.1: DSC thermograms for a) dodecanoic acid and b) 1-octadecanol (Kahwaji *et al.*, 2017a) 37
Figure 3.2: Carlon junction box 12" x12" x 6" 38
Figure 3.3: Coil in shell geometry; a) coil CAD design b) box CAD design c) single coil d) 3 coils in box.....38
Figure 3.4: a) Front b) side and c) top view of the coil(s) with various dimensions 39
Figure 3.5: Workbench view of (a) fully insulated and (b) partially insulated heat exchanger 40
Figure 3.6: Experimental setup a) CAD diagram b) photo of physical setup.....41
Figure 3.7: Polyscience SD15R-30 circulating bath.....42
Figure 3.8: Little Giant pump (model no. 5-MD).....43
Figure 3.9: Thermocouple placement 44
Figure 3.10: Thermocouple holder 44
Figure 3.11: BV2150 Vision turbine flowmeter.....45
Figure 3.12: Ni-cDAQ-9174 chassis and modules 47
Figure 3.13: Charging and discharging experimental trials based on the melting temperature 48
Figure 3.14: Heat loss/gain plot.....51
Figure 3.15: Power vs time demonstrating maximum, minimum and uncertainty values for a typical a) charging experiment and b) discharging experiment 54
Figure 3.16: Repeatability dodecanoic acid charging experiments a) power vs time b) power vs energy 56
Figure 3.17: Repeatability for dodecanoic acid discharging experiments a) power vs time b) power vs energy.....57
Figure 3.18: Repeatability for 1-octadecanol charging experiments a) power vs time b)

power vs energy 58
Figure 3.19: Repeatability for 1-octadecanol discharging experiments a) power vs time b) power vs energy 59
Figure 4.1: Typical trend of various temperature sensors for dodecanoic acid a) charging experiment b) discharging experiment.....61
Figure 4.2: Equivalent energy charging results for dodecanoic acid.....63
Figure 4.3: T_i identical T_R different charging results for dodecanoic acid.....64
Figure 4.4: T_R identical T_i different charging results for dodecanoic acid.....64
Figure 4.5: Equivalent energy discharging results for dodecanoic acid 66
Figure 4.6: T_i identical T_R different discharging results for dodecanoic acid 66
Figure 4.7: T_R identical T_i different discharging results for dodecanoic acid 67
Figure 4.8: Equivalent energy discharging results varying flow rate 68
Figure 4.9: T_i identical T_R different charging results varying flow rate.....68
Figure 4.10: T_R identical T_i different charging results varying flow rate.....69
Figure 4.11: Equivalent energy discharging results varying flow rate 69
Figure 4.12: T_i identical T_R different discharging results varying flow rate 70
Figure 4.13: T_R identical T_i different discharging results varying flow rate 70
Figure 5.1: Typical trend of various temperature sensors for 1-octadecanol a) charging experiment b) discharging experiment.....74
Figure 5.2: Equivalent energy charging results 1-octadecanol.....76
Figure 5.3: T_i identical T_R different charging results for 1-octadecanol 77
Figure 5.4: T_R identical T_i different charging results for dodecanoic acid.....77
Figure 5.5: Equivalent energy discharging results for 1-octadecanol.....79
Figure 5.6: T_i identical T_R different discharging results for 1-octadecanol 79
Figure 5.7: T_R identical T_i different discharging results for 1-octadecanol 80
Figure 6.1: Heat transfer rate during charging with dodecanoic acid and 1-octadecanol T_m-17°C; T_m+7°C a) vs time b) vs energy 82
Figure 6.2: Heat transfer rate during charging with dodecanoic acid and 1-octadecanol T_m-17°C; T_m+12°C a) vs time b) vs energy 83
Figure 6.3: Heat transfer rate during charging with dodecanoic acid and 1-octadecanol T_m-12°C; T_m+12°C a) vs time b) vs energy 83

Figure 6.4: Heat transfer rate during charging with dodecanoic acid and 1-octadecanol T_m-12°C; T_m+12°C a) vs time b) vs energy 84
Figure 6.5: Heat transfer rate during charging with dodecanoic acid and 1-octadecanol T_m-7°C; T_m+12°C a) vs time b) vs energy 84
Figure 6.6: Heat transfer rate during charging with dodecanoic acid and 1-octadecanol T_m-7°C; T_m+12°C a) vs time b) vs energy 85
Figure 6.7: Heat transfer rate during charging with dodecanoic acid and 1-octadecanol T_m-2°C; T_m+22°C a) vs time b) vs energy 85
Figure 6.8: Dynamic viscosity of 1-octadecanol and dodecanoic acid vs melting temperature differential (Yaws, 2003) 86
Figure 6.9: Heat transfer rate during discharging with dodecanoic acid and 1-octadecanol T_m+7°C; T_m-17°C a) vs time b) vs energy 87
Figure 6.10: Heat transfer rate during discharging with dodecanoic acid and 1-octadecanol T_m+12°C; T_m-17°C a) vs time b) vs energy 87
Figure 6.11: Heat transfer rate during discharging with dodecanoic acid and 1-octadecanol T_m+12°C; T_m-12°C a) vs time b) vs energy 88
Figure 6.12: Heat transfer rate during discharging with dodecanoic acid and 1-octadecanol T_m+17°C; T_m-12°C a) vs time b) vs energy 88
Figure 6.13: Heat transfer rate during discharging with dodecanoic acid and 1-octadecanol T_m+17°C; T_m-12°C a) vs time b) vs energy 89
Figure 6.14: Heat transfer rate during discharging with dodecanoic acid and 1-octadecanol T_m+17°C; T_m-7°C a) vs time b) vs energy 89
Figure 6.15: Heat transfer rate during discharging with dodecanoic acid and 1-octadecanol T_m+2°C; T_m -22°C a) vs time b) vs energy 90
Figure 6.16: Energy vs time for charging experiments 91
Figure 6.17: Energy vs time for discharging experiments 91
Figure 6.18: Heat transfer vs Fourier number for discharging experiment a) T_m +7°C; T_m -17°C b) T_m +12°C; T_m-17°C 94
Figure 6.19: Nusselt number vs time for T_m-17°C; T_m+12°C 95
Figure 6.20: Nusselt number vs time for T_m-17°C; T_m+17°C 96
Figure 6.21: Nusselt number vs time for T_m-7°C; T_m+17°C 96

Figure 6.22: Q_{mean} vs a) melting temperature differential and b) solidification temperature differential 98
Figure 6.23: Q_{mean} vs a) melting Stefan number and b) solidification Stefan number 99
Figure 6.24: Q_{mean} vs total Stefan number for a) charging and b) discharging 99
Figure 6.25: Q_{norm} vs a) melting Stefan number and b) solidification Stefan number 101
Figure 6.26: Q_{norm} vs total Stefan number for a) charging and b) discharging 101
Figure 6.27: $Q_{norm,t}$ vs a) melting Stefan number and b) solidification Stefan number ... 102
Figure 6.28: $Q_{norm,t}$ vs total Stefan number for a) charging and b) discharging 103

Abstract

The lack of design rules for the design and selection of phase change material based thermal energy storage (PCM-TES) systems using heat exchangers is a major impediment to the development and general acceptance of such systems. In order to get to design rules, the thermal storage community must first determine and agree on PCM-TES performance comparison metrics. It appears logical that the properties of PCM could play a role in the determination of comparison metrics.

This research presents results of a study performed on a TES using a coil-in-shell heat exchanger using two different PCMs, dodecanoic acid and 1-octadecanol. Characterization of this TES was performed over a range of initial and final temperatures, both for charging and discharging, comparing results of each. An attempt is made to compare different experiments using Nusselt number, Fourier number, melting and solidification Stefan number (Ste_m, Ste_s), total Stefan number (Ste_t), average heat transfer rate (Q_{mean}) and two normalized heat transfer rates (Q_{norm}) and ($Q_{norm,t}$).

List of Abbreviations Used

Abbreviations

HTF	Heat Transfer Fluid
LHTES	Latent Heat Thermal Energy Storage
NTU	Number of Transfer Units
PCM	Phase Change Material
PCM-HX	Phase Change Material based Heat Exchanger
PCM-TES	Phase Change Material based Thermal Energy Storage
PEG	Polyethylene Glycol
SHS	Sensible Heat Storage
TCS	Thermochemical Storage
TES	Thermal Energy Storage

Symbols

A	Heat transfer surface area (m^2)
Bi	Biot number (-)
c_p	Specific heat of the HTF (kJ/kg·K)
$c_{p,l}$	Specific heat capacity of the liquid PCM (kJ/kg·K)
$c_{p,s}$	Specific heat capacity of the solid PCM (kJ/kg·K)
E_{ch}	Ratio of energy retrieved by the system to energy stored (-)
E_{latent}	Theoretical latent energy stored by the PCM (kJ)
$E_{sensible}$	Theoretical sensible energy stored by the PCM (kJ)
E_{tot}	Total energy stored/discharged (kJ)
E_{total}	Total theoretical energy stored by the PCM (kJ)
Fo	Fourier number (-)
h	Convection coefficient of ambient air ($W/m^2·K$)
k_l	Thermal conductivity of the liquid PCM (W/m·K)
k_s	Thermal conductivity of the solid PCM (W/m·K)
L	Latent heat of the PCM (kJ/kg)
L_c	Effective length (m)
m_{pcm}	Mass of PCM (kg)
$Q_{adjusted}$	Adjusted heat transfer rate (W)
Q_{avg}	Average heat transfer rate (W)
$Q_c(t)$	Heat Transfer rate between the PCM and HTF during charging (W)

$Q_{d(t)}$	Heat Transfer rate between the PCM and HTF during discharging (W)
Q_{gain}	Heat gain (W)
Q_{loss}	Heat loss (W)
Q_{max}	Maximum heat storage capacity (W)
Q_{mean}	Average heat transfer rate per unit energy stored (W)
Q_{norm}	Normalized average heat transfer rate (W)
Q_{therm}	Average thermal power (W)
s	Thickness of PCM layer (m)
St	Stanton number (-)
Ste	Stefan number (-)
Ste_m	Melting Stefan number (-)
Ste_s	Solidification Stefan number (-)
Ste_t	Total Stefan number (-)
T_c	Cold side PCM temperature (°C)
t_{final}	End time of trial (s)
T_{amb}	Ambient air temperature (°C)
T_h	Hot side PCM temperature (°C)
$T_{HTF,in}$	HTF inlet temperature (°C)
$T_{HTF,out}$	HTF outlet temperature (°C)
T_i	Initial PCM temperature (°C)
T_{in}	HTF inlet temperature (°C)
$t_{initial}$	Start time of trial (s)
t^{LTES}_{sol}	Solidification time (s)
T_m	PCM melting temperature (°C)
T_{out}	HTF outlet temperature (°C)
T_R	HTF reservoir temperature (°C)
T_{ref}	Reference temperature (°C)
V_{PCM}	Volume of the PCM (m^3)
$\dot{V}$	Volumetric flow rate (m^3/s)
α	Thermal diffusivity of the PCM (m^2/s)
δE_j	Absolute uncertainty of instantaneous energy stored (kJ)
δE_{total}	Absolute uncertainty of total energy stored (kJ)
Δp	Pressure drop (kPa)
δQ	Absolute uncertainty of heat transfer (W)
$\delta Q/Q$	Relative uncertainty of heat transfer (-)
ΔT	Temperature difference between HTF and PCM (°C)
Δt	Time difference between data recordings (s)
ΔT_1	Temperature difference between HTF inlet and reference (°C)
ΔT_2	Temperature difference between HTF outlet and reference (°C)
ΔT_{avg}	Average temperature difference between HTF and PCM (°C)
ΔT_m	Melting temperature differential (°C)

ΔT_s	Solidification temperature differential (°C)
$\delta \dot{V}$	Absolute uncertainty of volumetric flow rate (m^3)
$\delta \Delta T$	Absolute uncertainty of temperature difference (°C)
E	Effectiveness of the PCM-TES (-)
H	Performance factor for plate type PCM-TES (-)
ρ_l	Density of liquid PCM (kg/m^3)
ρ_s	Density of solid PCM (kg/m^3)
τ	Charging/ discharging time (s)

Acknowledgements

I would like to thank my supervisor Dr. Dominic Groulx, for his guidance throughout this process, and my committee members, Dr. Alain Joseph and Dr. Jesse Maassen, for their time and feedback.

I would also like to acknowledge the technical and support staff in the Department of Mechanical Engineering, especially Kate Hide, Jonathan MacDonald and Peter Jones who helped me overcome many obstacles over the course of this project.

Thanks are also owed to my colleagues Gino de Andrade, Elisangela D'Oliveira, Abiola Akinnibosun and Max Belinson for their constant support and help with the many challenges I faced on this journey.

I want to thank the people who helped inspire me to pursue my goals in this field namely Dr. Edwin MacLellan and Dr. Larry Hughes.

Lastly, I am grateful to the Nova Scotia Department of Natural Resources and Renewables, Dalhousie University, the Province of Nova Scotia as well as the Natural Science and Engineering Research Council (NSERC), who have provided necessary funding for the undertaking of this project.

Chapter 1: Introduction

1.1 Background on Thermal Energy Storage

With increasing development into renewable energy such as solar and wind technology, a deficiency that must be addressed involves the intermittent nature of these energy sources. Solar and wind energy cannot be relied on to supply energy at all times to every sector due to discontinuities in their natural energy supply. Energy storage must therefore be integrated with renewable energy in order to optimize these systems. Chemical batteries are useful in storing and delivering electrical work but can be expensive for large scale storage (Herbinger & Groulx, 2022). Thermal storage systems are typically a lot less expensive than batteries due to the nature and cost of the materials needed (Cabeza, 2021). In certain instances, it may be cost-effective and more efficient to employ thermal storage systems when heat is the required output. This approach is particularly suitable for circumstances where renewable energy is generated thermally, such as in solar thermal systems, or geothermal systems or when the intended use of the energy is thermal, such as for space heating, domestic hot water supply, or various thermal industrial processes. In such cases, it is reasonable to consider the utilization of a thermal energy storage (TES) system.

Thermal energy storage can also be used to optimize the industrial sector. Up to 50% of energy input into industrial applications across the world is dissipated in the form of exhaust gases, cooling water and other losses to the environment (Xu *et al.*, 2017); known as waste heat. Waste heat recovery systems can utilize this leftover thermal energy to supply space heating. Integrating waste heat recovery with TES enables the system to offset the time delay between supply and demand. This can lead to improved thermal efficiency and enhanced economic viability of industrial processes.

Another potential use of thermal energy storage systems is its use in load shifting in order to decouple the production of heat from its usage. Residential homeowners and businesses alike could utilize thermal energy storage and electric heating (which is already becoming

increasingly popular in most regions) and adopt a time-of-day electricity pricing model in order to reduce the cost of heating and ultimately reduce the cost of their electricity bills (Xu *et al.*, 2021). Heat could be generated and stored during off-peak hours and released during on-peak hours, thereby reducing the total cost of electricity to supply the same amount of heat. Utilizing thermal energy storage for load shifting can be a mutual interest for both the user and the supplier, as reducing peak demand will create increased flexibility on the demand side and alleviate grid stress (Xu *et al.*, 2021).

There are multiple types of TES systems, including sensible heat storage systems (SHS), latent heat thermal energy storage (LHTES) systems, and thermochemical storage (TCS) systems. Sensible heat storage systems involve the use of storage materials which are not subject to phase change during the energy storage process. These systems are widely researched and use materials such as water, rock, brick and thermal oils. These systems have inherent drawbacks including low energy densities and heat losses or self discharge (Tatsidjodoung *et al.*, 2013). LHTES systems utilize phase change materials (PCMs), which, as their name indicates, exhibit phase change during the storage process. This phase change can be of the solid-solid, solid-liquid, solid-gas, or liquid-gas form in which energy is stored or released in the form of latent heat. LHTES systems offer advantages over sensible heat storage systems including high energy storage densities and relatively constant operating temperature ranges. Lasty, TCS systems involve a reversible chemical reaction excited by an initial heat source. The reversal of this reaction, typically involving a catalyst, releases the energy in the form of heat. TCS has the advantages of having very high energy density values (up to 10 times that of PCMs) and exhibit no self discharge (Sadeghi, 2022; Tatsidjodoung *et al.*, 2013). This technology, however, is still in its infancy and according to Sadeghi (2022) research in this area is still under fundamental investigation. Due to LHTES offering greater energy density, less heat losses and a low range of operating temperatures when compared with SHS while being much further developed than TCS systems, LHTES appears to be a promising technology in the field of energy storage.

1.2 Research Objectives

The focal point of this research is to address the issue that, currently, there is no standard for comparing PCM based thermal energy storage systems, making a comparison of systems for different applications very difficult. Some form of standard procedure must be developed so that the findings of a particular test can be utilized for new efforts (Agyenim *et al.*, 2010). Developing standard comparison metrics will help engineers match an ideal latent heat energy storage system with a given application using driving parameters such as storage size, operating temperatures, storage time, etc. (Groulx *et al.*, 2021). A set of design rules must then be crafted from these comparison metrics. Without these rules, these systems must be designed using experimental trial and error for each new iteration. This iterative design process would be very expensive and engineering firms would need to undergo extensive modelling and experimental tests in order to properly size a system. It is for this reason that design rules are a necessity for this application.

This research attempts to deepen the current framework of LHTES design rules through assessing the significance of PCM properties in the design process. This involves the running of experiments with the same LHTES system under identical operating conditions (temperature range, flow rate) and varying only the PCM type used in the system. Two different PCMs were used in this study, by keeping other variables constant, any discrepancies observed from the behaviour of the system can be attributed to the thermophysical properties of the chosen PCMs. A comparison between the performance of the system operating with two different PCMs can lead to new understanding of how PCM properties affect LHTES operation.

1.3 Organization of Thesis

This thesis is broken down into 7 chapters. Including:

- Chapter 1: Introduction

  The background of thermal energy storage and its significance in fields of renewable energy, industrial process and buildings is discussed. LHTES is introduced and an explanation as to why it is viewed as a superior option to other

TES technologies is provided. The objectives of this study are presented.

- Chapter 2: Literature Review

  Recent literature in the field of LHTES is discussed at length. Including: the operation of LHTES systems, types of PCMs and their advantages and disadvantages, geometries used in LHTES systems, techniques for improving heat transfer and performance indicators used to analyze LHTES systems.

- Chapter 3: Experimental Setup and Procedure

  A detailed account of the equipment, materials, experimental procedure and the data analysis methods used in the operation of the experiment are provided in this Chapter as well as the construction methods and design process of the experimental setup.

- Chapter 4: Dodecanoic acid results

  Results of experiments using dodecanoic acid are presented and discussed with regard to theoretical concepts and expectations from similar experiments in literature.

- Chapter 5: 1-octadecanol results

  Results of 1-octadecanol experiments are similarly discussed in this chapter.

- Chapter 6: PCM comparison and data reduction

  In this Chapter, the data is reduced using methods examined in literature and a comparison of the two PCMs analyzed in this study is undertaken.

- Chapter 7: Conclusion

  A conclusion to the study is presented discussing all aspects considered in this analysis.

Chapter 2: Literature Review

2.1 Latent Heat Thermal Energy Storage Systems

Latent heat thermal energy storage systems are designed to store thermal energy by transferring heat into a phase change material. LHTES systems are essentially classical heat exchangers where one of the working fluids is replaced by a PCM. When this material undergoes a phase transition, a large amount of thermal energy is stored isothermally in the form of latent heat. This isothermal heat is beneficial in order to maintain temperature control for applications which require it. Due to the temperature difference through the heat exchanger, which drives the heat transfer process, sensible heat is also stored in the system. LHTES systems are always comprised of a PCM and container which houses it. A heat exchanger which is responsible for transferring energy from a heat transfer fluid (HTF) to the PCM are often employed in these systems as well. Some applications for these types of systems include optimization of building heating, (Garg *et al.*, 2018; Morovat *et al.*, 2019) solar thermal energy (Joseph *et al.*, 2016; Yang *et al.*, 2017) and waste heat recovery (Yan *et al.*, 2020).

2.2 Working Principles of LHTES Systems

2.2.1 Charging

Charging describes the melting of the PCM which in turn stores thermal energy in the form of latent and sensible heat. The charging process of a PCM in LHTES systems involves heating the PCM beyond its melting point causing it to transition from its solid to its liquid phase. This is an endothermic process and requires energy supplied to the PCM. This energy is carried by some form of HTF in most instances. The charging process of PCM exhibits two modes of heat transfer. The initial stages of charging when the PCM is solid are dominated by conduction; however as melting is initiated, natural convection begins to occur (Azad *et al.*, 2022). The development of natural convection results in an enhancement of the heat transfer in the system by moving already hot liquid away from the contact surface resulting in more heat being transferred to cooler liquid, thereby augmenting the overall heat transfer due to the increase in temperature gradient (Groulx, 2018). When

observing the experimentally determined power curve of LHTES systems, charging processes typically present a plateaued region in which this power increase occurs (Groulx *et al.*, 2021). Due to the upwards motion of the liquid from natural convection, care needs to be taken when designing LHTES systems so that there is significant heat transfer surface area at the bottom of the container to make up for the lack of natural convection in this region.

2.2.2 Discharging

Discharging is the physical process of solidification in which the thermal energy stored by the PCM is released. In discharging, the PCM is cooled below its solidification point, where it undergoes solidification and changes phase from liquid to solid. This is an exothermic process and in heating applications, is responsible for supplying heat to the system, usually through the means of an HTF. The heat transfer during solidification is greatly dominated by conduction (Groulx, 2018). A problem that presents itself when it comes to the discharging process is the phenomenon of supercooling which can occur in some PCMs such as salt hydrates and sugar alcohols (Pielichowska & Pielichowski, 2014; Tomassetti *et al.*, 2022). Supercooling occurs when a PCM fails to solidify at its solidification temperature and instead cools below this temperature while remaining in the liquid phase. In LHTES systems where predictability of system behaviour is critical to facilitate design, the supercooling phenomenon could cause the operation of the system to be compromised if it were to occur to a large degree (Groulx, 2018).

2.3 Types of PCM Used

PCM selection is an important part of the design of any LHTES system. In carrying out this selection a number of important factors must be considered, including (Tomassetti *et al.*, 2022):

- Adequate melting temperature for the application
- High Latent heat energy
- High Specific heat
- High Thermal conductivity
- Low Degree of supercooling

- Good Thermal stability
- Container compatibility
- Non-toxicity
- Low vapour pressure
- Low volume change during phase change
- Recyclability
- Cost effectiveness
- Availability

If possible, a PCM should have most if not all of the above properties, however this is not usually the case. Therefore, it is important to consider which properties are the most significant to the specific application. In order to select a PCM for a given application, information about the application, including desired operating temperature, container material, volume/mass constraints, desired power and stored energy, environmental and economic constraints must be known. Table 1 demonstrates the advantages and disadvantages of various types of PCMs found in literature. These types of PCMs are divided into general categories of organics, inorganics and eutectics.

2.3.1 Organics

- *Fatty Acids*

Fatty acids are carboxylic aliphatic acids with the general formula $H(CH_2)_nCOOH$. They are viewed to have superior properties to most other PCMs due to their good melting temperature range for passive solar applications and for use in buildings, high latent heat storage capacity, lack of supercooling during phase transition, non-toxicity, low vapour pressure, low cost and small change in volume during melting. Fatty acids also have good thermal and chemical stability and any change in the latent heat or melting temperature found can be attributed to impurities in PCMs (Yuan *et al.*, 2014). These PCMs are also ecologically harmless as they are biologically based.

Table 2.1: Types of PCM Advantages and Disadvantages

	Organic Materials					Inorganic Materials		Eutectics
	Fatty Acids	Paraffins	Sugar Alcohols	Fatty Alcohols	PEGs	Salt Hydrates	Metallics	
Advantages	•High Latent Heat •No supercooling •Recyclable •Good thermal stability •Good chemical stability •Repeatable melting and solidification •Low volume change	•High Latent Heat •No supercooling •Recyclable •Good thermal stability •Good chemical stability •Non-corrosive	•High Latent Heat •Non-toxic •Non-flammable •Recyclable	•High latent heat •Low degree of supercooling •Low cost •Non-toxic •Good thermal stability	•Good latent heat •Non-toxic •Non-corrosive •Good biocompatibility •Easily chemically modified	•High volumetric latent heat value •Good thermal conductivity •Non-flammable •Low environmental impact •Low cost	•High volumetric latent heat value •High thermal conductivity	•High volumetric latent heat value •Good thermal conductivity •No phase segregation at melting temperature
Disadvantages	•Low thermal conductivity •Mildly corrosive •Pungent odour	•Low thermal conductivity Incompatible with plastic containers •Large volume change	•Poor thermal stability •High degree of supercooling •Degradation of melting point and latent heat	•Low thermal conductivity	•Low thermal conductivity	•High degree of supercooling •Thermal degradation •Incongruent phase separation •Poor thermal stability	•High degree of supercooling •Leakage •Corrosive •High volume change •Low latent heat per weight	•Low latent heat per weight •Can suffer from supercooling •Can be expensive •Limited data of thermophysical properties

Fatty acids do however have poor thermal conductivity and it is recommended to either combine them with materials of high thermal conductivity as either composite PCMs or by utilizing PCM heat exchangers comprised of highly conductive materials with large surface areas. Fatty acids are also mildly corrosive and emit an unpleasant odour (Pielichowska & Pielichowski, 2014).

- *Paraffins*

Paraffins are saturated hydrocarbons with a C_nH_{2n+2} chemical formula. They possess high latent heat storage capacities and are therefore highly researched as PCMs. Paraffins have various phase change temperatures dependant on their molar mass. They are considered to be non-toxic, non-reactive and compatible with metal containers due to their non-corrosive nature. They demonstrate little to no supercooling and have good thermal stability over a large number of cycles. Paraffins are derived from crude oil, which puts into question their long term environmental impact (Pielichowska & Pielichowski, 2014). They are not however compatible with some types of plastics due to their chemical similarity. Paraffins share the same drawback as fatty acids in having low thermal conductivities making it necessary to increase the heat transfer of the PCM-TES system they comprise in other ways (Castellón *et al.*, 2011; Pielichowska & Pielichowski, 2014). Paraffins also have a relatively large change in volume during phase change which can create problems in container storage (Tatsidjodoung *et al.*, 2013).

- *Polyethylene Glycols (PEGs)*

Polyethylene Glycols or PEGs are semi-crystalline polymers, used as PCMs due to their large heat of fusion which is attributed to a high degree of crystallinity. PEGs have melting points which vary from 4°C to 70°C. The heat of fusion and melting point varies with molecular weight (Pielichowska & Pielichowski, 2014). PEGs share properties with other organic PCMs including non-toxicity, non-corrosiveness, and good biocompatibility. PEGS have similar thermal conductivities to other organic PCMs, making them poor conductors (Kou *et al.*, 2019).They are also easily chemically modified leading researchers to synthesize new PCMs based on PEGs by combining them with other materials such as fatty acids as well as carbon nanotubes and nano-particles to increase thermal properties (Pielichowska & Pielichowski, 2014).

- *Sugar Alcohols*

Sugar alcohols are described by the general chemical formula $C_nH_{2n+2}O$ and belong to a low molecular weight carbohydrate group. They can have melting temperatures ranging from 18°C to 230°C, with most melting points occurring above 90°C (Shao *et al.*, 2023). In use as PCMs, sugar alcohols generally have a higher latent heat storage capacity than other organic substances such as paraffins. They are also non-flammable, non-toxic, and non corrosive and can be readily available in large quantities (Tomassetti *et al.*, 2022). However, some sugar alcohols can suffer from supercooling as well non-spontaneous crystallization. These PCMs also suffer from poor thermal stability and can show signs of degradation of both melting point and latent heat. (Shao *et al.*, 2023)

- *Fatty Alcohols*

Fatty alcohols have a relatively high latent heat value in respect to other organic PCMs, high energy storage densities, low degree of supercooling, are naturally available and are of low cost (Zhang *et al.*, 2021). They have suitable melting temperatures for low temperature applications, which range from approximately 21-56°C. They are also non-toxic and according to Sharma *et al.* (2020), have good thermal stability under large number of thermal cycles. However, like all organic PCMs they suffer from low thermal conductivity.

2.3.2 Inorganics

- *Salt Hydrates*

Salt hydrates are inorganic salts containing water of crystallization and have the chemical formula $AB{\cdot}nH_2O$. Salt hydrates are promising materials for use as PCMs for low temperature applications (0-100°C) due to their high volumetric storage capacities and phase change temperature within this desirable range. Salt hydrates also possess slightly higher thermal conductivities when compared to organic PCMs. Unfortunately, salt hydrates have concerns surrounding their thermal stability and exhibit a high degree of supercooling. Incongruent phase separation can occur for these materials which leads to degradation of thermal performance over time. Supercooling occurs when these materials do not undergo re-solidification as they are cooled back down to their melting point which can be detrimental to LHTES systems where predictable performance is a necessity

(Kumar *et al.*, 2019). In order to combat the challenges facing these materials it is proposed that gelling agents be added to the material to reduce sedimentation and segregation of the heavier phase and promote congruent melting, while nucleating agents could be added to combat supercooling issues (Pielichowska & Pielichowski, 2014).

- *Metallics*

Metallic PCMs cover a wide range of melting temperatures from roughly 18°C to 25°C to greater than 1000°C. Metallic PCMs have advantages over other forms of PCMs due to their thermal conductivities being 1 to 2 orders of magnitude greater than organics and salt hydrates (Shamberger & Bruno, 2020). They also have good thermal stability. They do however face the issue of supercooling which can lead to complications in the controlled release of the latent thermal energy. Metallic PCMs are also susceptible to leakage, corrosion and volume change. Low temperature metallic PCMs include alloys of gallium, bismuth, tin and indium. These PCMs have high latent heat storage capacity per unit volume but low latent heat storage capacity per unit weight relative to organic PCMs and salt hydrates (Wang *et al.*, 2022).

2.3.3 Eutectics

Eutectics are a mixture of two different PCMs which melt congruently at the same melting temperature. They can be comprised of organic-organic, inorganic-organic or inorganic-inorganic. Eutectics melt without phase segregation at their singular melting temperature (Tatsidjodoung *et al.*, 2013). Eutectic PCMs can have high latent heat and high thermal conductivity but can be expensive and some eutectics can suffer from supercooling (Tomassetti *et al.*, 2022).

2.4 Common Heat Exchanger Geometries Employed

The goal of any type of PCM heat exchanger, or any heat exchanger for that matter, is to optimize the heat transfer rate between the two working fluids, or in the case of PCM heat exchangers, between the HTF and the PCM. In general, PCMs suffer from low thermal conductivity. Therefore, other methods of increasing heat transfer must be utilized. Using highly conductive materials such as copper or aluminum and increasing the heat transfer

surface area are some methods of optimizing the heat transfer in the system (Diaconu *et al.*, 2023).

2.4.1 Shell-and-tube

Shell-and-tube heat exchangers are among the most prevalent types of PCM heat exchangers and are comprised of two primary design components: the container (shell) and the tube. There are a variety of different designs used for shell-and-tube heat exchangers including various shell geometries (usually cylindrical or rectangular), as well as different configurations of the tubes themselves such as helical or conical geometries, or multiple tubes in a single shell.

2.4.1.1 Shell Design

Cylindrical shells are the most popular container design for shell-and-tube PCM heat exchangers. For simple cylinder-shaped PCM heat exchangers with a single tube pass, two common configurations for the placement of the PCM relative to the heat transfer fluid are used in literature. The first configuration involves having the PCM inside the shell of the heat exchanger, with a single pipe or tube circulating the heat transfer fluid through the center. This method is the most prevalent and is often referred to as a "pipe model" or "double pipe heat exchanger" (Alnakeeb *et al.*, 2021; Gasia *et al.*, 2017; Pahamli *et al.*, 2018; Safari *et al.*, 2022). The other method would be to reverse the location of the PCM and HTF so that the HTF circulates within the cylindrical shell and the PCM is contained in the inner pipe or tube. This configuration is sometimes referred to as a cylindrical model (Han *et al.*, 2017; Kalapala & Devanuri, 2018; Zayed *et al.*, 2020). Figure 2.1 shows both configurations mentioned.

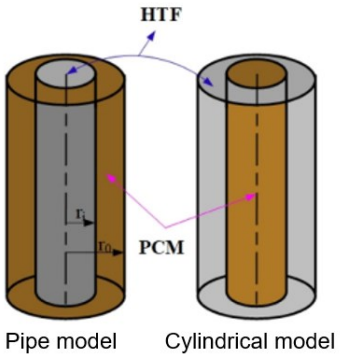

Figure 2.1: Cylindrical shell-and-tube PCM heat exchangers (Zayed *et al.*, 2020)

A third type of cylindrical shelled PCM heat exchanger involves the use of three total concentric tubes and is referred to as a triple concentric tube heat exchangers or triplex tube heat exchanger. The middle tube contains PCM while the inner and outer tubes contain the HTF. Triplex tube heat exchangers increase the surface area in contact with the PCM and thus increase heat transfer in the system. This design is viewed as advantageous for simultaneously charging and discharging the PCM (Kalapala & Devanuri, 2018). Through numerical simulation and experimental validation, Mat *et al.* (2013) found that adding internal and external fins to the triplex tube heat exchanger could reduce the melting time by more than half compared to an un-finned arrangement as seen in Figure 2.2.

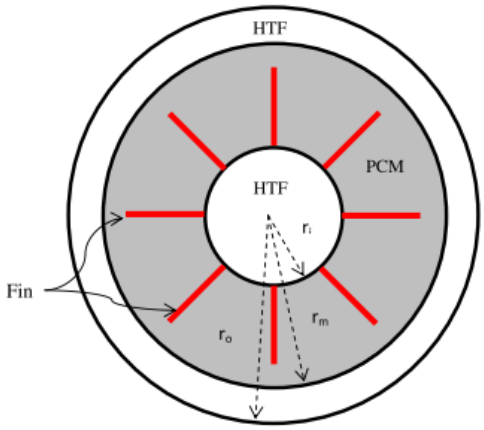

Figure 2.2: Triplex tube with longitudinal fins (Mat et al., 2013)

Rectangular geometries for shell-and-tube heat exchangers are another widely researched geometric configuration (Mao *et al.*, 2022; Nguyen *et al.*, 2022). Patil (2020) used a rectangular shell geometry with a varying number of tubing coils in an experimental investigation. Herbinger and Groulx (2022) performed an experimental study on a rectangular shelled geometry with multiple finned-tubes. Zivkovic and Fujii (2001), in a numerical study, found that rectangular containers had a melting time of half that of cylindrical containers of the same volume and heat transfer area. Safari *et al.* (2022) investigated numerically the effects of shell geometry and tube eccentricity in a shell and tube PCM heat exchanger. The types of shells analyzed included square, rhombus, horizontal rectangle, vertical rectangle, equilateral and inverted equilateral triangle shells. Their results found that a horizontally oriented rectangular geometry provided the best results compared with these other geometrical orientations for a concentric tube.

2.4.1.2 Tube Design

Modifications to the geometry of the tube can greatly increase the surface area of the heat exchanger. Helical tube geometries, demonstrated in Figure 2.3, have been investigated in a number of experimental studies as these configurations can greatly increase the surface area of the heat exchanger (Joseph *et al.*, 2016; Yang *et al.*, 2017). Wołoszyn *et al.* (2021) numerically studied the effects of helical, conical and a combination of the two geometries as pipe model shell-and-tube PCM heat exchangers. It was found that conical tube geometries reduced melting time greatly but resulted in reductions of exergy efficiencies. The conical geometry also resulted in a linear increase in the PCM liquid fraction until the PCM was fully melted. The combined helical and conical geometries with added spiral fins resulted in the greatest reduction in melting time. Mahdi *et al.* (2020) compared numerically a helical double pipe shell-and-tube with its horizontal and vertical straight tubes. The helical coil decreased the melt time to a great effect and was found to combine the superior features of melting of both horizontal and vertical oriented models.

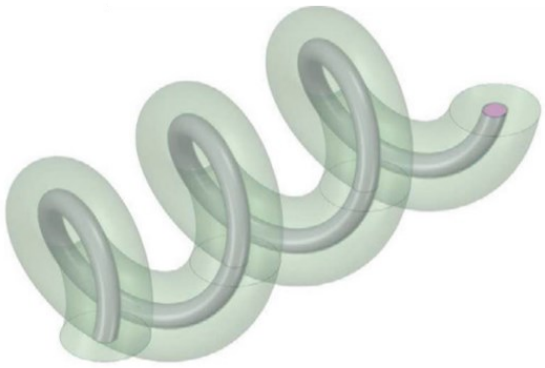

Figure 2.3: Helical tube geometry (Wołoszyn *et al.*, 2021)

Studies have also utilized multiple tubes in shell-and-tube heat exchangers and analyzed the effects of both the number of tubes and their arrangement. Kousha *et al.* (2019) performed an experimental study which analysed the effects of increasing the number of tubes in a cylindrical shelled double tube PCM heat exchanger. The study found that increasing the number of HTF tubes enhanced both the melting and solidification processes, with a greater effect demonstrated in solidification. It was also determined that increasing the number of tubes negatively affected the average Nusselt number due to disruption of the melt movement by the upper tubes. Natural convection plays a large role

in the melting of PCM and placement of the HTF tubes can have a significant effect on the extent to which natural convection affects the melting process. Mahdi *et al.* (2021) performed a numerical study investigating the effect of HTF tube arrangement in cylindrical shelled multi-tube PCM heat exchanger. It was demonstrated that arrangements with tube placement near the bottom of the shell correlated with decreased melting times by upwards of 70%.

2.4.2 Packed bed

Packed bed is another type of geometry which has been studied for use in LHTES systems (Amin *et al.*, 2014; Li *et al.*, 2018; Mao & Zhang, 2020; Trevisan *et al.*, 2022). Packed bed thermal energy storage systems are composed of solid materials surrounded by circulating heat transfer fluid. The solid materials can be rock or steel for sensible heat storage systems (Liang *et al.*, 2022), however, for LHTES systems PCM filled capsules are employed. Figure 2.4 illustrates a packed bed LHTES system with spherical PCM capsules. Packed bed geometries involve the use of a large number of spherical or ellipsoidal capsules which increase the surface area to volume ratio of the PCM thus increasing heat transfer. In a study by Liang *et al.* (2022), it was determined that in comparison to shell-and-tube heat exchangers, packed bed based LHTES systems are better suited for applications requiring high flow rates, such as concentrated solar power plants. In contrast shell-and-tube heat exchangers were determined to be superior for low flow applications. A significant parameter in the design of packed bed systems was the ratio of tank diameter to the capsule diameter.

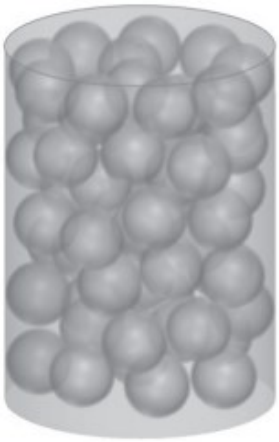

Figure 2.4: Packed bed LHTES with spherical capsules (Amin et al., 2014)

2.4.3 Plate type heat exchangers

Plate type heat exchangers involve the use of layers of PCM plates with layers of HTF flowing between them (Li *et al.*, 2023; Morovat *et al.*, 2019). The plates are generally flat rectangles, however, various plate geometries can be used in order to increase heat transfer rate. Gürel (2020) utilized a zigzag geometry in a numerical study which varied both PCM type and thickness, as well as heat transfer fluid inlet temperature. It was discovered that as the PCM layer thickness decreased, melting time was reduced. Li *et al.* (2023) performed a numerical study with experimental validation, for a plate type PCM heat exchanger. It was found that a 3:1 aspect ratio (height to width) of the plates was optimal for reducing melt time and increasing the number of plates and reducing plate thickness increased heat transfer. In an experimental study performed by Medrano *et al.* (2009), commercial heat exchangers were filled with PCM in an effort to determine their effectiveness as PCM heat exchangers. A compact finned coil-in-shell heat exchanger, typically used as an evaporator or condenser, as well as a gasketed plate-and-frame heat exchanger (illustrated in Figure 2.5) were examined and compared to different variations of double piped shell and tube heat exchangers. Compared to the compact heat exchanger, it was found that the plate-and-frame heat exchanger did not possess high enough storage capacity relative to heat exchanger volume to be useful, while the compact heat exchanger exhibited good results with exceptional heat transfer.

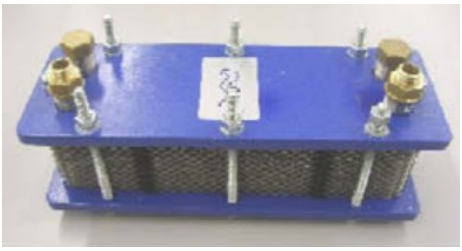

Figure 2.5: Plate-and-frame heat exchanger (Medrano *et al.*, 2009)

2.5 Container Materials for LHTES systems

For low and medium temperature thermal storage applications, bulk storage containers and encapsulated storage containers are the most highly used types of containers. Different geometries are used for bulk storage containers in order to improve heat transfer area and thusly increase the heat exchanger effectiveness (Zayed *et al.*, 2020). Container material is

one of the most crucial aspects in container design as they must be compatible with both the type of PCM used as well as the operating temperature of the system. Materials used as PCM containers include aluminum, stainless steel, copper, carbon steel, acrylics and other plastics and ceramics (Punniakodi & Senthil, 2021). Some plastic containers are not compatible with paraffins due to their chemical similarity (Castellón *et al.*, 2011), while some metal containers can be damaged by the slightly corrosive fatty acids. Aluminum and stainless steel, due to their corrosion resistance is viewed to be compatible with all types of organic PCMs (Pielichowska & Pielichowski, 2014; Punniakodi & Senthil, 2021). Vasu *et al.* (2017) studied the effects of various container material compatibility with inorganic PCMs and found that stainless steel shows good compatibility with all types of salt hydrates PCMs, while aluminum alloys are suitable for use with organic PCMs due to their corrosion resistance but show high levels of corrosion when used with salt hydrate PCMs. Copper and brass containers show good compatibility with salt hydrates and other inorganics, however the long-term stability of this container material is an area of concern. Acrylics, and other plastics can be used for low temperature applications, while for high temperature applications materials such as ceramics and stainless steel should be used as they can withstand high thermal stresses. (Punniakodi & Senthil, 2021).

2.6 Techniques for Improving Heat Transfer for PCM Heat Exchangers

2.6.1 Nano-enhanced PCM

Particles less than 100 nm in size are considered nano-particles. Below this critical length, the surface area to volume ratio is great, and in comparison to normal grained particles, nano-particles exhibit superior, thermal, optical, magnetic and electrical properties (Das *et al.*, 2007). The use of nano-particles in PCMs has been a highly researched topic in literature of late. These nano-particles can increase the overall thermal conductivity of PCMs through addition due to their high thermal conductivity and low density. Common types of nano-particles include, graphene (Tariq *et al.*, 2020), carbon nanotubes (Kumar *et al.*, 2022), and metals and metal oxides (Martin *et al.*, 2019). A problem with nanoparticle addition however is the reduction of the latent heat value of the PCM. This value continues to decrease as the concentration of nano-particles increases (Hayat *et al.*, 2022).

Nano-enhanced PCM can also exhibit poor cycle stability and thermal stability due to the separation of the nano-particles from the PCM. A surfactant is often used to help combat this problem however this leads to a further reduction of latent heat values (Kumar *et al.*, 2022).

2.6.2 Metal foam

Additions of porous media to PCM can be used as techniques to stabilize the form of PCMs and to prevent leakage of molten PCMs. They are also used to enhance heat transfer by increasing heat transfer area. The extent to which porous media can increase the heat transfer is dependant on their thermal conductivity. Porous media with high thermal conductivity and therefore high potential for increasing heat transfer in PCMs are metal foams (Diaconu *et al.*, 2023). Metal foams are easily fabricated, are of low cost, and have a low environmental impact. They do, however, considerably repress the convective heat transfer effect observed during melting. Their occupying of space in a LHTES system also results in the reduction of thermal energy capacity. Xiao *et al.* (2019) experimentally studied the use of copper foam as an enhancement technique in a sodium acetate trihydrate based composite PCM. They found a 176% increase in thermal conductivity with the use of the metal foam in comparison to the PCM composite alone. However, the addition of the foam caused a 22% reduction in latent heat (Xiao *et al.*, 2019).

2.6.3 Fins

Fins are included on PCM heat exchangers as a method of increasing heat transfer surface area, thereby increasing heat transfer. Fins are an enticing method of enhancing heat transfer in LHTES systems due to their low cost, availability, and proven effectiveness. Fins can also be combined with other heat transfer enhancement techniques including nano-particles or metal foam to greatly increase heat transfer. The effect of fin parameters can be an important design variable when choosing to add fins to a PCM heat exchanger. Generally, increasing the number of fins and length of fins results in an increase in heat transfer, however, due to the effect of fin geometry on natural convection, an optimal value for both fin length and fin number exists (Eslami *et al.*, 2021). Fin thickness, in general, plays little to no role in heat transfer enhancement and an increase in fin thickness can

actually be detrimental to heat transfer during melting (Eslami *et al.*, 2021). For melting processes, fin orientation is significant in that it is more successful to have more fins in the lower half of the container (Eslami *et al.*, 2021).

2.6.4 Orientation

Orientation of the HTF tubes or geometry can be significant to the heat transfer of the PCM as it changes phase. Han *et al.* (2017) performed a study addressing the orientation of shell-and-tube heat exchangers, either vertical or horizontal, which included shell-and-tube heat exchangers of both cylindrical and pipe model. It was determined that for the pipe model, vertical orientation with the inlet at the bottom provided the highest heat transfer rates, while for the cylindrical model the orientation and inlet placement did not have a large effect (Han *et al.*, 2017).

2.6.5 Eccentricity

The effects of eccentricity were also examined in literature. Alnakeeb *et al.* (2021) performed a numerical study to investigate the effect of increasing eccentricity on an inner flat tube in a pipe model LHTES system. Their results found that an eccentricity of 0.75 resulted in the maximum melting time reduction. Safari *et al.* (2022) investigated the effects of shell geometry and tube eccentricity in a shell-and-tube PCM heat exchanger. Their results found that the maximum reduction in melt time was found to be the case with a circular shell with a tube eccentricity of 0.5. They found that there was in fact an optimal range of eccentricity as their results analysed eccentricities up to 0.7. It was also determined that increasing the eccentricity prolongs convection dominated melting time and shortens the conduction dominated melting time, making for a more uniform heat transfer rate (Safari *et al.*, 2022).

2.7 Key Operating Parameters to study in LHTES systems

2.7.1 Inlet temperature

The driving force during the latent stage of heat transfer in PCM heat exchangers is the temperature difference between the HTF and the PCM melting temperature. For this

reason, increasing this temperature difference will have a large effect on the overall heat transfer in the LHTES system. Many authors have found this to be true and that by increasing HTF inlet temperatures during charging melting times were reduced, while decreasing HTF temperatures during discharging, solidification times were reduced (Herbinger & Groulx, 2022; Patil, 2020; Rathod & Banerjee, 2014; Yang *et al.*, 2017).

2.7.2 Flow rate

Varying mass flow rate is a method some authors have experimented with in order to study the effects on LHTES system heat transfer rate. The effects of mass flow rate on heat transfer rate for PCM-based systems have been mixed with some papers concluding that the variation of mass flow rate showed a negligible effect on the heat transfer of the system (Patil, 2020; Seddegh *et al.*, 2017; Yang *et al.*, 2017). Conversely, other authors have determined that there is a correlation between increased mass flow rate and decreased solidification time (Agarwal & Sarviya, 2016; Wang *et al.*, 2013) and decreased melting time (Rathod & Banerjee, 2014; Wang *et al.*, 2013). Theoretically, with an increase in fluid velocity, the convection coefficient of the internal flow of the HTF will increase due to the relationship with the Reynolds number (Bergman *et al.*, 2017). Rathod and Banerjee (2014) explained that the transition from laminar to turbulent flow can also lead to an increase in the convection coefficient and should increase the heat transfer experienced in LHTES systems. Nevertheless, the effect viewed from an increase in flow rate has been reported to be small, especially in comparison to the effect of increasing the inlet temperature. This can be attributed to the dominant effect of the conduction heat transfer between the PCM and the heat exchanger surface making a change in the thermal resistance of the HTF have a negligible effect on the overall heat transfer process in the LHTES (Kalapala & Devanuri, 2018; Patil, 2020). With the thermal conductivity of the PCM being the bottleneck in the thermal resistance circuit, increasing the HTF flow rate may only increase the overall heat transfer in the LHTES by a small degree.

2.8 Characterization of PCM Heat Exchangers

The central problem in the development of PCM heat exchangers today is caused by the difficulties in modelling the complex nature of the heat transfer of these systems. In order

to combat what is referred to as the *rate problem* (Groulx, 2018), researchers have attempted to characterize LHTES using both experimental and numerical methodologies. The variation of key operating parameters as well as the use of different geometries are some methods used to characterize LHTES systems found profusely throughout the literature. Few researchers have varied the type of PCM in the system as a method of characterization. Table 2.2 (experimental) and Table 2.3 (numerical) clearly articulate the different characterization studies of PCM heat exchangers found in literature today. In which the type of PCM used, the temperature range, the characterization method, the method of analyzing heat transfer, the numerical methods and the findings of the study are presented. Cells highlighted in green indicate the use of multiple PCMs while cells highlighted in red show the use of multiple geometries.

As mentioned in Section 2.7 many researchers have analyzed the variation of both flow rate and inlet temperature. In contrast, initial PCM temperature has not had significant impact on heat transfer of the system (Herbinger & Groulx, 2022; Patil, 2020). There have also been researchers that have varied geometry with results indicating that increasing heat transfer surface area proved to increase the heat transfer of the system (Patil, 2020; Safari *et al.*, 2022; Wołoszyn *et al.*, 2021).

One aspect that has not been thoroughly addressed is the impact of PCMs on the system itself. Gürel (2020) varied the types of PCM in a numerical study of a plate type heat exchanger and found that heat transfer for *n*-octadecane was superior compared to RT35. However, no performance evaluation was performed by this author to determine why this may be. Azad *et al.* (2021) experimentally studied the onset of natural convection for both dodecanoic acid and *n*-octadecane and found that the former required a larger amount of liquid for natural convection to begin. Raud *et al.* (2017) developed an optimization method for designing shell-and-tube and fin-and-tube LHTES systems. The study compared two different eutectic salts and found that thermal conductivity was the most significant property for shell-and-tube geometries, while for finned tube geometries energy density was much more significant in optimizing the design. In a previous publication by this author, a coil-in-shell PCM heat exchanger was used to analyze two types of PCM.

Dodecanoic acid was found to result in slightly better heat transfer compared to OM55, however the properties of these two PCMs were too similar to form definitive results (Callaghan *et al.*, 2023). Aside from these studies, to the authors knowledge, no other authors have analyzed the effect of using multiple PCMs in a fully characterized LHTES system and even fewer have done so experimentally. The effect of PCM properties could affect the system in ways not yet apparent to researchers.

2.9 Key Performance Indicators for LHTES systems

In order to design an LHTES system, design characteristics must be determined in a way that is useful for engineers to integrate these systems into various applications. Difficulties in numerically modelling full 3D LHTES systems, with the added complexities of convection and conduction as well as phase change, have led to the notion that experimental validation must be utilized as a method of characterization for these systems. This experimental design process is costly and time consuming and for this reason cannot be a long-term successful method of integrating these systems into an industrial landscape. The similarity of PCM heat exchangers to traditional heat exchangers leads to the conclusion that perhaps similar design rules used for traditional heat exchangers can be created for LHTES systems (Groulx, 2018).

2.9.1 ε-NTU Method

The effectiveness of a given heat exchanger can be determined by how its actual heat transfer rate compares to the maximum heat transfer rate that could possibly be delivered by the heat exchanger (Bergman *et al.*, 2017). Since LHTES heat exchangers are essentially standard heat exchangers with one of the working fluids replaced with PCM, it is logical that an effectiveness approach could be used to evaluate LHTES systems. This method often requires the process to be steady-state. However, a problem when applied to LHTES is the dynamic nature of charging and discharging of the PCM, resulting in an outlet temperature, and thus the heat transfer rate, constantly changing (Groulx *et al.*, 2021). Effectiveness used in practice to categorize PCM heat exchangers often assumes that there is no change in internal energy of the heat transfer fluid, as well as neglecting the sensible portion of the heat transfer (Beyne *et al.*, 2023).

Table 2.2: Experimental characterization studies of PCM Heat Exchangers

PCM Used	Geometry	Characterization Method	Temperature Range	Method of analyzing heat transfer	Findings	Reference
Paraffin wax T_m: 46°C Onset 48°C End L: 153 kJ/kg	Rectangular shell and tube with fins	Varied inlet temperature as well as flow rate for trials. Varied fin thickness and material.	T_i: 20°C. T_R: 50°C, 60°C, 70°C.	Heat transfer rate is calculated by thermal resistance method using: $R_{overall} = \frac{T_{ave,water} - T_{ave,PCM}}{\dot{Q}}$	Varying the inlet temperature by 10 degrees increased heat transfer greatly. Increasing the flow rate showed little to no effects. Heat transfer rate is enhanced when fin thickness increases, however storage capacity is sacrificed. Graphite fins offer more advantages compared to copper.	Nguyen *et al.* (2022)
RT35 T_m: 29°C (Solidus) 35°C (Liquidus) L: 170 kJ/kg	Cylindrical multitube	Varied inlet temperature as well as the number of inner tubes.	T_R Melting: 70°C, 75°C, 80°C T_R Solidification: 10°C	Heat transfer rate was calculated using $\dot{Q} = \dot{m}c_p\lvert T_{out} - T_{in}\rvert$ where T_{out} and T_{in} are the outlet and inlet temperatures of the HTF.	Increasing the number of inner tubes enhances both melting and solidification rates. Increasing the number of tubes can decrease average Nusselt number caused by upper tubes hampering the flow of natural convection.	Kousha *et al.* (2019)
Dodecanoic Acid T_m: 43.3°C L: 184 kJ/kg	Rectangular shell and tube with fins	Varied number of fins, as well as mass flow rate, inlet temperature and initial PCM temperature for charging and discharging experiments.	T_i: 41°C, 36°C, 31°C, 26°C, 21°C T_R: 65°C, 60°C, 55°C, 50°C, 45°C	Heat transfer rate was calculated using $\dot{Q} = \dot{m}C_p\lvert T_{out} - T_{in}\rvert$ where T_{out} and T_{in} are the outlet and inlet temperatures of the HTF.	The difference between the HTF temperature and the melting point of the PCM plays a large role in the heat transfer rate of the system. The systems initial temperature has a much less significant impact on the system's heat transfer rate.	Herbinger and Groulx (2022)
Dodecanoic Acid T_m: 43.3°C L: 184 kJ/kg	Coil in rectangular shell with multiple coils	Varied number of coils in shell, as well as initial temperature, final temperature and HTF flow rate.	T_i: 41°C, 36°C, 31°C, 26°C, 21°C T_R: 65°C, 60°C, 55°C, 50°C, 45°C	Heat transfer rate was calculated using $\dot{Q} = \dot{m}C_p\lvert T_{out} - T_{in}\rvert$ where T_{out} and T_{in} are the outlet and inlet temperatures of the HTF.	The difference between the HTF temperature and the PCM melting temperature has a significant impact on the heat transfer of the system. Initial temperature plays a very minor role in the effect on the heat transfer of the system. Change in flow rate is observed to have little to no effect on the power of the system. Heat transfer rate increases with each additional coil.	Patil (2020)
RT 82 T_m 82°C L: 176 kJ/kg	Triplex Tube	Variation of HTF inlet temperature and mass flow rate.	T_i: 30°C T_R: 85°C, 90°C, 95°C, 100°C	Measured charging and discharging time vs temperature in order to determine when the system was fully charged or discharged.	For charging an increase in heat transfer only when the mass flow rate was increased to 16 kg/min. For discharging an increase in heat transfer was associated with each increase in mass flow rate.	Al-Abidi *et al.* (2014)

					An increase in HTF temperature proved to have a significant effect on the melting time.	
Dodecanoic Acid T_m: 43.3°C L: 184 kJ/kg OM55 T_m: 55°C L: 188 kJ/kg	Coil in shell	Varied PCM type as well as initial temperature, final temperature.	T_i: 41°C, 36°C, 31°C, 26°C, 21°C 33°C, 38°C, 43°C, 48°C T_R: 65°C, 60°C, 55°C, 50°C, 45°C 77°C, 72°C, 67°C, 62°C	Heat transfer rate was calculated using $\dot{Q} = \dot{m}C_p\lvert T_{out} - T_{in}\rvert$ where T_{out} and T_{in} are the outlet and inlet temperatures of the HTF.	Heat transfer rate for dodecanoic acid is slightly higher than for OM55. The difference between the heat transfer of the two PCMs is small mostly due to their similar physical properties.	Callaghan *et al.* (2023)

Table 2.3: Numerical characterization studies of PCM Heat Exchangers

PCM Used	Geometry	Characterization Method	Temperature Range	Numerical modelling techniques	Findings	Reference
Paraffin Tm: 27°C L: 231.2 kJ/kg	Plate type	Effects of aspect ratio, plate thickness, number of plates as well as HTF velocity and inlet temperature are investigated. The influence of thermocouples is also assessed.	Ti: 12°C TR: 60°C, 50°C, 45°C, 40°C, 35°C	Enthalpy-porosity method is used to track the solid liquid interface. Boussinesq approximation is used to simulate natural convection.	Thermocouples accelerated PCM melting process by 6% on average. An aspect ratio of 3:1 allows for the fastest melting rate, while an aspect ratio of 2:3 demonstrates the slowest. Increasing the number of plates, and reducing their thickness, increased heat transfer. Increasing HTF flow rate and inlet temperature increased heat transfer.	Li et al. (2023)
Paraffin Tm: 43-55°C L: 153.2 kJ/kg	Shell and Tube with various shell geometries	Shell geometry was varied as well as inner tube eccentricity.	Ti: 25°C. TR: 95°C.	Enthalpy-porosity method is used to simulate the melting of the PCM.	For the concentric case the rectangular shell shows the greatest reduction of melt time compared to the cylindrical case. Increasing eccentricity factor reduces melt time up to an optimum point.	Safari et al. (2022)
RT 60 Tm: 55-61°C L: 160 kJ/kg	Shell and Tube	The ratio of shell to tube radius was varied for geometries of various heights.	Ti Melting: 88°C Ti Solidification: 28°C	Boussinesq approximation is used to simulate natural convection. Enthalpy-porosity method was applied to simulate phase changing.	For both varying the tube diameter and the shell diameter, thermal behavior is similar. An optimal ratio of shell to tube diameter is determined to be approximately 5. The height exhibits a negligible effect on the optimal ratio.	Shen et al. (2020)

RT54HC /2% expanded graphite composite Tm: 54°C L: 168 kJ/kg	Helical coil shell-and-tube	HTF inlet temperature was varied as well as flow rate. The heat transfer process was modeled with and without natural convection.	Ti: 30°C TR: 70°C, 65°C, 60°C, 55°C	Enthalpy-porosity method was applied to model the dynamic melting process. Boussinesq approximation was applied to account for natural convection.	Inlet temperature had a great effect on the mean power of the system. The effect of increasing flow rate is negligible. The effect of natural convection is significant for PCM melting cases.	Yang et al. (2017)
RT35 Tm: 28°C-40°C L: 157 kJ/kg n-octadecane Tm: 28.2°C L: 243.5 kJ/kg	Plate type	Studied effects of plate thickness, inlet temperature, HTF velocity and PCM thickness. Geometry and the type of PCM was also varied for this study.	Ti: 22°C TR: 52°C, 57°C, 62°C	Enthalpy- porosity method was used to evaluate the solid-liquid interface. Boussinesq approach was used to model density variations.	Decreasing PCM layer thickness reduced melting time. Increasing inlet temperature increases average heat transfer. Heat transfer is superior for n-octadecane as the PCM compared to RT-35. Optimal plate thickness was found to be 0.6 mm.	Gürel (2020)
RT50 Tm: 45°C (Solidus) 51°C (Liquidus) L: 170 kJ/kg	Various double tube	Employed various geometrical enhancement techniques such as spiral fins, helical and conical geometry, while keeping the same PCM mass to determine effect on PCM melt time and exergy efficiency.	Ti: 30°C TR: 75°C	Enthalpy-porosity method used to simulate phase change. Boussinesq approximation used to account for natural convection.	Combined conical, helical and spiral finned design significantly reduces PCM melt time. The use of fins reduces melting time for helical geometries. Conical geometries increase melting at the inlet and linearly increase melt fraction until the PCM is fully melted.	Wołoszyn et al. (2021)
Paraffin Wax Tm: 61°C L: 191 kJ/kg	Shell and tube	Varied, inlet temperature, mass flow rate as well as tube thickness and radii.	Ti: 25°C TR: 85°C	Iterating between temperatures and thermal resistances was used to obtain a solution. $\dot{Q} = \dot{m}C_p\lvert T_{out} - T_{in}\rvert$ was used to calculate heat transfer rate.	Inlet temperature strongly influences PCM's solidification and melting, while the mass flow rate has minimal impact. The effect of tube thickness is minimal. Tube radius affects operating time and outlet temperature.	Kibria et al. (2014)
NaCl + Na2CO3 Tm: 630°C L: 283 kJ/kg NaCl + Na2SO4 Tm: 630°C L: 266 kJ/kg	Shell and tube/Finned Shell and tube	Compared two different PCMs and two different geometries using an analytically based optimization method.	Ti: 630°C TR: 660°C	Darcy's law with an isotropic resistance tensor based on the Carman–Kozeny equation is adopted. Boussinesq approximation used to account for natural convection	Thermal conductivity was found to be more significant in the optimization of basic shell and tube geometries, while for finned shell and tube energy density of the PCM was more significant.	Raud et al. (2017)

If we consider only the latent stage of the heat transfer, energy is transferred from the HTF to a constant temperature medium. This means that the maximum heat transfer will occur when the HTF leaves the heat exchanger at the PCM melting temperature. This resulted in the development of Eq. (2.1) (Castell *et al.*, 2011)

$$\varepsilon = \frac{T_{in} - T_{out}}{T_{in} - T_m} \tag{2.1}$$

where T_{in} and T_{out} are the inlet and outlet temperatures of the HTF. This gives a maximum effectiveness of 1 when the HTF exits at the phase change temperature. An average value of effectiveness is taken over the duration of the charging and discharging experiment due to the constant changing of the HTF temperatures throughout these processes.

Many authors have utilized the average effectiveness taken over time as a means of comparing various types of LHTES systems. Castell *et al.* (2011) studied a coil-in-tank PCM heat exchanger in which the ε-NTU method was used to find a relationship with the ratio of mass flow rate over the heat transfer surface area. Tay *et al.* (2012b) expanded on this average effectiveness relation by plotting it for an array of multiple tube banks, with multiple PCMs for melting and solidification experiments. Amin *et al.* (2012) defined average effectiveness equations for an experimental packed bed LHTES system with encapsulated PCM spheres of a given diameter. Amin *et al.* (2014) created a more general ε-NTU based semi-analytical numerical model using the proportion of isothermal to parallel thermal resistances in a tank of PCM spheres. This approach was also used for a LHTES system with radial finned tubes (Tay *et al.*, 2014). Aziz *et al.* (2022) extended this work further by using a semi analytical ε-NTU correlation to optimize the design of a packed bed LHTES system. Fang *et al.* (2019) developed an analytical method of determining optimal length of a tube-in-tank LHTES system using ε-NTU theory. This method was validated using numerical results. López-Navarro *et al.* (2014) developed two separate correlations for average effectiveness, one for melting and another for solidification, in a study on a coil-in-tank LHTES system. Chen *et al.* (2014) applied the ε-NTU method to characterize a finned tube in tank LHTES system. Allouche *et al.* (2015) experimentally studied a tube in tank LHTES system equipped with a manual stirrer and compared results to those found in literature using an ε-NTU model.

Average effectiveness has also been calculated using the proportion of material which has yet to change phase, or phase change fraction as the independent variable instead of time. Tay *et al.* (2012a) experimentally studied a coil in tank LHTES system with one, two and four coils and averaged the effectiveness over the phase change fraction instead of time. Belusko *et al.* (2012) similarly determined an equation for instantaneous effectiveness using the phase change fraction which was validated using experimental results.

Effectiveness NTU method is promising as a method of evaluating PCM heat exchangers, however there is no one method which can be applied to every geometry and several assumptions are made including neglecting any sensible heat storage as well as assuming the PCM is at a uniform temperature. In reality the non-uniformity of the PCM as well as sensible storage before and after phase change could led to the outlet temperature leaving the heat exchanger at a temperature below or above the PCM melting temperature. This would lead to an effectiveness greater than one, defying the definition of effectiveness.

2.9.2 Dimensionless numbers

Bastani *et al.* (2014), in a study investigating the thermal performance of PCM wallboards, looked at the relationship between Stephan number (which is defined as the ratio of sensible energy stored to latent energy stored), Biot number (defined as the ratio of convection heat transfer at the surface of a body to the conduction through the body) and Fourier number (defined as the ratio of conductive transport rate to the sensible energy storage rate) in order to optimize the design wallboard thickness. Stephan number was used to represent PCM properties and was altered by varying latent heat and heat capacity values while the ΔT remained constant. Biot number was used to represent wallboard thickness. Fourier number was used as a dimensionless charging time. It was found that by decreasing the Stefan number, Fourier number was increased and by increasing Biot number Fourier number was decreased.

Kuznik *et al.* (2015) performed a dimensionless analysis of a PCM to air heat exchanger in an attempt to optimize its design. This approach utilized Biot number, Stefan number, Stanton number (defined ratio of convective heat transfer to the thermal storage capacity

in a liquid state) as the and Fourier number in which relations of $1/Bi \cdot Fo$ and Ste were used as material properties while Bi/St was considered a property of the system geometry. These relations guided the design of the air to PCM heat exchanger in order to determine channel length and air flow rate. This is done by plotting these dimensionless parameters against the power value measured at the end of the discharging period, in an attempt to be condense the performance of the system into a single power value. However, by plotting only this final power the transient power of the system is not considered which may omit significant details relating to key design characteristics.

2.9.3 *UA* Approach

The overall heat transfer coefficient, *U* helps determine the heat transfer through a variety of resistive mediums and is defined as the reciprocal of the total thermal resistance of a system. This value is used to help determine the effectiveness of traditional heat exchangers and therefore was sought to be applied to PCM-HX systems. Lazaro *et al.* (2019) utilizes an approach for evaluating heat transfer performance using the *UA*-value of the system. In which

$$Q(t) = UA \cdot \frac{\Delta T_2 - \Delta T_1}{ln\left(\frac{\Delta T_2}{\Delta T_1}\right)} \tag{2.2}$$

with the log mean temperature term being defined by

$$\Delta T_1 = T_{HTF,in} - T_{ref} \tag{2.3}$$

$$\Delta T_2 = T_{HTF,out} - T_{ref} \tag{2.4}$$

The determination of which reference temperatures were acceptable was investigated in this study. As major discrepancies in the *UA*-values were seen from the use of different reference temperatures, it is uncertain which value to use in defining this log mean temperature term in the comparison of different experimental data using *UA*-values.

König-Haagen and Diarce (2023), in a numerical study analyzing a plate type LHTES system, developed two methods of utilizing the *UA*-value to determine solidification time of LHTES systems. The first method utilizes only the material properties of the PCM, the geometry and the initial boundary conditions to calculate a discharging time using:

$$UA = 2\frac{A \cdot k}{s} \tag{2.5}$$

where k is the thermal conductivity of the PCM, A is the heat transfer surface area and s is the thickness of the PCM layer. The second method utilizes the results of an experiment or numerical simulation in order to estimate the UA for different boundary conditions using:

$$UA = \frac{Q}{t_{sol}^{LTES} \cdot (T_m - T_{in}) - \frac{Q}{\dot{m} \cdot c_p}} \tag{2.6}$$

where t_{sol}^{LTES} is the solidification time measured, Q is the thermal energy of the system, $\dot{m}$ is the mass flow rate, T_m is the PCM melting temperature, T_{in} is the inlet temperature of the HTF and c_p is the specific heat. This approach was verified using numerical simulations and gave promising results; however, it is useful for a simple plate type geometry alone and may be difficult to be applied to more complicated geometries.

2.9.4 Normalized Power

Medrano *et al.* (2009) defined a metric called Q_{therm}, for comparing various PCM heat exchangers using average thermal power and dividing it by the average temperature difference between the HTF and the PCM, ΔT and the effective heat transfer surface area, A.

$$Q_{therm} = \frac{Q_{avg}}{A \cdot \Delta T_{avg}} \tag{2.7}$$

Similarly, Lazaro *et al.* (2019) introduced a normalized power Q_{norm}, which is equal to a mean power, Q_{mean} (the average power of the system integrated on an energy basis) divided by the temperature difference, ΔT and the system volume, V_{PCM},.

$$Q_{norm} = \frac{Q_{mean}}{V_{PCM} \cdot \Delta T} \tag{2.8}$$

$$Q_{mean} = \frac{\int_0^{E_{tot}} Q(E)dE}{E_{tot}} \tag{2.9}$$

Based on numerical results, this metric was plotted against the Stefan number, Biot number, HTF volume and NTU

Herbinger and Groulx (2022) plotted the Q_{mean} of an experimental finned multitube system against different Stefan numbers, one for charging and one for discharging and found promising results. As the Stefan number was increased, Q_{mean} also increased. This led to the notion that Q_{mean} could possibly be used as a comparative metric for PCM systems.

Patil (2020), in an experimental coil-in-shell PCM heat exchanger, plotted Q_{mean} against the melting Stefan number (Ste_m). The Q_{norm} was also plotted versus the melting Stefan number. The ΔT in the Q_{norm} equation was replaced with the difference between the HTF temperature and the melting temperature. The average heat transfer rate or Q_{mean} was found to increase parabolically with increasing Ste_m, while for discharging this trend linear. It is also worth noting that the results showed a large degree of uncertainty for low Stefan number values.

2.9.5 Other Performance Indicators

Li *et al.* (2023) defined a performance factor for melting in a plate-type heat exchanger, η. The researchers compared the average power of the PCM heat exchanger, taken as the energy stored divided by the melting time, with the power supplied by the pump, taken as the pressure drop multiplied by the flow rate.

$$\eta = \frac{E_{tot}/_{\tau}}{\Delta p \cdot \dot{V}} \tag{2.10}$$

Equation (2.10) defines the performance factor where, E_{tot} is the total energy stored, τ is the melt time, Δp is the pressure drop throughout the system and q is the volumetric flow rate.

Shen *et al.* (2020) simply calculated an energy storage ratio for a shell-and-tube heat exchanger. The ratio of the energy retrieved by the system to the energy stored by the system was defined as

$$E_{ch} = \frac{Q(t)}{Q_{max}} \tag{2.11}$$

where $Q(t)$ is the accumulated energy by the system and Q_{max} is the maximum heat storage capacity of the system. This value is plotted against the charging time of the system for various shell to tube radius ratios.

Bauer (2011) developed an approximate analytical solution to determine solidification time for a PCM-based LHTES system with a finned shell-and-tube geometry. Results are based on thermophysical properties of the PCM and the geometrical dimensions of the container. Raud *et al.* (2017) extended this work further by utilizing liquid PCM properties to determine melting time for shell-and-tube/finned shell-and-tube heat exchangers. These models are incomplete for addressing the entirety of the LHTES design process as assumptions made neglecting natural convection and using the PCM melting as the temperature at which all heat transfer occurred could limit the validity of this method.

2.10 Conclusion

This chapter presented the current literature significant to the design, comparison, and performance of LHTES systems. The author attempted to relate the current work with the state-of-the-art research being performed today in the context of continuing upon what has been previously researched. Researchers have developed LHTES systems of many configurations and have varied operating parameters in order to get a better understanding of how the design of these systems could be optimized. There is, however, no set of design rules standardized for the construction of these systems. Many types of performance indicators have been developed as an initial method of building design rules, however no parameter that has been developed has been able to capture all of the significant parameters of LHTES systems into one criterion. For this reason, multiple elements of the design process must be analyzed separately for now until a true universal LHTES performance indicator can be developed.

One element of the design of LHTES is the selection of the PCM. The study of PCM materials for use in LHTES systems has been well documented and many PCMs have been considered by researchers. The selection of one PCM over another is usually done by evaluating system parameters, design constraints and financial implications. Very few

researchers have compared LHTES systems' performance using various PCMs and none have come up with a clear method of evaluating the performance of these systems. Therefore, the comparison of the performance of LHTES systems using different PCMs is something that has not been done before in a systematic way, and a clear methodology for doing so has not been established.

Chapter 3: Experimental Setup and Procedure

3.1 Materials

3.1.1 Phase Change Material Selection

The first PCM selected to be used in this research was dodecanoic acid. Many previous research projects done at the Lab of Applied Multiphase Thermal Engineering (LAMTE) have used this PCM. (Azad *et al.*, 2021; Herbinger & Groulx, 2022; Patil, 2020; Skaalum & Groulx, 2020) A variety of phase change materials found in literature were considered to be used as the second PCM in the present study, including all of those mentioned in Table 3.1. These PCMs were selected having melting points within the range of operation of the laboratory equipment (15°C-80°C). The most important factors considered when choosing the second PCM were the degree of difference of thermophysical properties from dodecanoic acid, the cost and whether supercooling was a possibility. The thermophysical properties considered in the selection of the PCM were the latent heat, the thermal conductivity, and the specific heat. Table 3.1 displays literature based PCMs, listing their melting points, PCM types, and the deviations of their thermophysical properties from dodecanoic acid.

The PCMs considered to be the most ideal for this comparison were those which displayed properties with the furthest deviations from those of dodecanoic acid. Some PCMs, however, were taken out of consideration due to their underlying problematic attributes or afflictions. PCMs which exhibit supercooling were not considered due to the possibility that it would interfere with the temperature, power and energy storage measurements in the system. The inorganic eutectics and salt hydrates listed in Table 3.1 were subsequently withdrawn from consideration as the second PCM due to their known exhibition of supercooling. Commercial PCMs purchased from a supplier, including P116 and P37, can sometimes have misrepresented thermophysical properties. Due to this commercial PCMs were also removed from being considered as the second PCM.

Table 3.1: Comparison of PCM found in literature to dodecanoic acid (green: high deviation, yellow: intermediate deviation, red: poor deviation)

Material	Type	Melting temperature (°C)	Percent Difference from Dodecanoic Acid			Reference
			Latent heat	Thermal Conductivity	Specific Heat	
Caprylic acid	Fatty Acid	16	**-19%**	**0.67%**	**8.41%**	(Cabeza & Heinz, 2005)
Polyglycol E600	PEG	22	**-31%**	**26.67%**	-	(Cabeza & Heinz, 2005)
Paraffin C13-C24	Paraffin	23	**3%**	**40.00%**	-	(Cabeza & Heinz, 2005)
34% Mistiric acid + 66% Capric acid	Fatty Acid	24	**-20%**	**9.33%**	-	(Cabeza & Heinz, 2005)
n-Octadecane	Paraffin	28	**9%**	**-1.33%**	-	(Cabeza *et al.*, 2011)
Nonadecane	Paraffin	31.8	**-2%**	**20.00%**	**-11.79%**	(Kahwaji *et al.*, 2017b)
Decanoic (capric) acid	Fatty Acid	32	**-21%**	**13.33%**	**1.03%**	(Kahwaji *et al.*, 2017b)
PT37	Commercial	36.4	**12%**	**-13.33%**	**-7.69%**	(Kahwaji *et al.*, 2017b)
PEG-1000	PEG	37.1	**-16%**	**33.33%**	**15.90%**	(Kahwaji *et al.*, 2017b)
Eicosane	Paraffin	37.5	**34%**	**53.33%**	**3.08%**	(Kahwaji *et al.*, 2017b)
Docosane	Paraffin	43.8	**27%**	**60.00%**	**-14.36%**	(Kahwaji *et al.*, 2017b)
P116	Commercial	47	**22%**	**60.00%**	**23.08%**	(Alawadhi, 2008)
Paraffin Wax SA327204	Paraffin	48.2	**-15%**	**33.33%**	**17.95%**	(Kahwaji *et al.*, 2017b)
Paraffin C20-C33	Paraffin	49	**3%**	**40.00%**	-	(Cabeza & Heinz, 2005)
Paraffin Wax SA327212	Paraffin	51.2	**-7%**	**33.33%**	**3.59%**	(Kahwaji *et al.*, 2017b)
61.5% Mg(NO3)2 + 38.5% NH4NO4	Inorganic eutectic	52	**-32%**	**229.33%**	-	(Cabeza *et al.*, 2011)
61.5% Mg(NO3)2 + 38.5% NH4NO3	Inorganic eutectic	52	**-32%**	**229.33%**	-	(Cabeza *et al.*, 2011)
Tetradecanoic (myristic) acid	Fatty Acid	54.7	**1%**	**40.00%**	**-2.05%**	(Kahwaji *et al.*, 2017b)
Paraffin Wax SA411663	Paraffin	57.7	**7%**	**0.00%**	**3.59%**	(Kahwaji *et al.*, 2017b)
Na(CH3COO)·3 H2O	Salt hydrate	58	**33%**	**320.00%**	-	(Cabeza *et al.*, 2011)

62.5% Mg(NO3)2 + 37.5% NH4NO3	Inorganic eutectic	58	**45%**	**320.00%**	-	(Cabeza *et al.*, 2011)
1-octadecanol	Fatty Alcohol	58	**18%**	**40.00%**	**-10.26%**	(Kahwaji *et al.*, 2017b)
50% Mg(NO3)2·6H2O + 50% MgCl2·6H2O	Inorganic eutectic	58.5	**-28%**	**240.00%**	-	(Cabeza *et al.*, 2011)
Paraffin C22-C45	Paraffin	59	**3%**	**40.00%**	-	(Cabeza & Heinz, 2005)
58.7% Mg(NO3)2·6H2O + 41.3% MgCl2·6H2O	Inorganic eutectic	59	**-28%**	**240.00%**	-	(Cabeza *et al.*, 2011)
Hexadecanoic (palmitic) acid	Fatty Acid	61.7	**12%**	**46.67%**	**-4.10%**	(Kahwaji *et al.*, 2017b)
Palmitic acid	Fatty Acid	64	**1%**	**8.00%**	**5.61%**	(Cabeza & Heinz, 2005)
Paraffin C21-C50	Paraffin	67	**3%**	**40.00%**	-	(Cabeza & Heinz, 2005)
Octadecanoic (stearic) acid	Fatty Acid	68.4	**15%**	**26.67%**	**-5.64%**	(Kahwaji *et al.*, 2017b)

PCMs mentioned in the literature with melting points below 22°C were excluded as potential secondary PCMs, as the minimum trial temperature (22°C below the PCM melting point) would fall within the freezing range of the heat transfer fluid (water). Of the remaining PCMs, the most compelling options were PEG-1000, eicosane, docosane and 1-octadecanol. Eicosane and docosane were ruled to be too expensive for the study as well as due to the incompatibility of paraffins with the plastic container chosen for the system. PEG-1000 and 1-octadecanol were considered to be both viable options for the secondary PCM, however, in two out of the three significant properties, 1-octadecanol exhibited slightly more favourable deviations from dodecanoic acid than PEG-1000, making it the preferred choice as the second PCM used in this study.

3.1.2 Phase Change Material Properties

Two PCMs were used for this study. Exactly 9.0 kg of PCM was carefully weighed and placed into the container using a scale. The same amount of PCM was used for both PCM

types in this study. The first, as mentioned in the previous section, being dodecanoic acid, an organic fatty acid, with a melting point of 43°C. The second PCM used in the study was 1-octadecanol which was chosen based on its price, thermophysical properties different than those of dodecanoic acid, and its compatibility with the system. Table 3.2 presents the properties of each PCM.

Table 3.2: Thermophysical Properties of dodecanoic acid (Desgrosseilliers *et al.*, 2013) and 1-octadecanol (Kahwaji *et al.*, 2017b; Yaws, 2003)

Thermophysical Properties	**Dodecanoic acid**	**1-octadecanol**
Density (solid)	930 ± 20 kg/m^3	862 ± 86 kg/m^3
Density (liquid)	885 ± 20 kg/m^3	805 ± 81 kg/m^3
Heat capacity (solid)	1.95 ± 0.2 kJ/kg·K	1.75 ± 0.175 kJ/kg·K
Heat capacity (liquid)	2.4 ± 0.03 kJ/kg·K	2.49 ± 0.25 kJ/kg·K
Thermal conductivity (solid)	0.160 ± 0.004 W/m·K	0.29 ± 0.029 W/m·K
Thermal conductivity (liquid)	0.150 ± 0.004 W/m·K	0.21 ± 0.021 W/m·K
Heat of fusion	184 ± 9 kJ/ kg	218 ± 22 kJ/ kg
Melting temperature	43.0 ± 1.5 °C	57 ± 1.5°C
Dynamic viscosity	0.008 Pa·s	0.01 Pa·s

Kahwaji *et al.* (2017b) used differential scanning calorimetry (DSC) thermograms measured at 2°C min^{-1} to determine the onset of melting temperature for both PCMs used in this study. The results of which are presented in Figure 3.1. In Figure 3.1 a) dodecanoic acid is shown to have only one endothermic peak at 43°C demonstrating the solid-liquid melting transition occurring at this temperature. In Figure 3.1b) 1-octadecanol has two endothermic peaks at 55°C and 58°C which signify two separate phase changes occurring: a solid-solid transition and a solid-liquid melting transition. For experimental planning purposes the melting point was taken to be 57°C, splitting the difference between these two phase change points. The DSC thermogram also presents an exothermic heat flow for 1-octadecanol, representing the solidification process, two peaks are shown for this process as well also representing a solid-solid transition at 50°C and a liquid-solid solidification at 58°C.

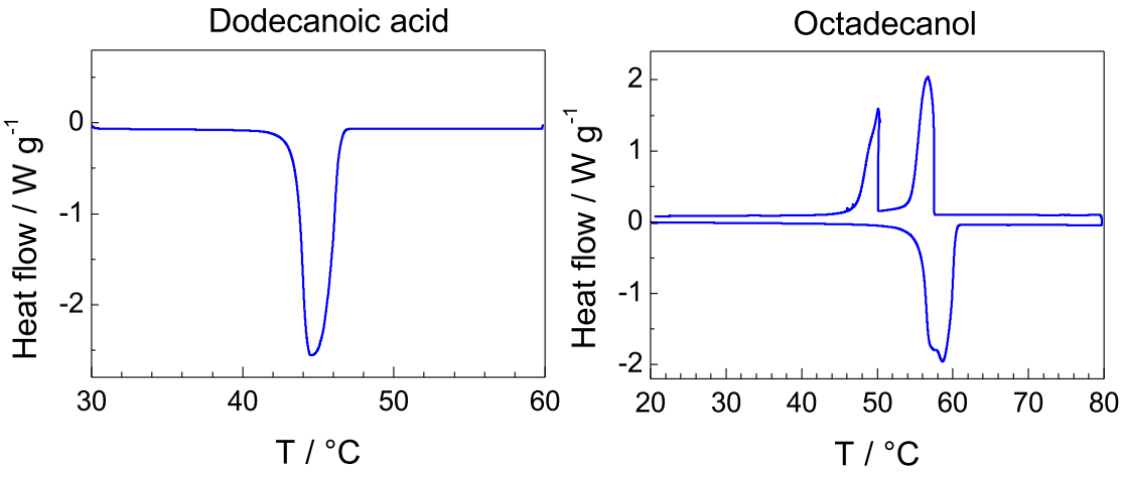

Figure 3.1: DSC thermograms for a) dodecanoic acid and b) 1-octadecanol (Kahwaji *et al.*, 2017a)

3.2 Heat Exchanger Design

3.2.1 Container

A Carlon non-metallic junction box of 12” by 12” by 6” in dimensions, (Figure 3.2), made of PVC (polyvinyl chloride) plastic material, was used to contain the PCM. The inner dimensions of the box are 11 15/16” by 11 7/16” by 6”. The lid is fastened to the container by 4 stainless steel screws and a foam gasket is used to fully seal the box. This junction box holds a NEMA type 6P rating, meaning it can be used for both indoor and outdoor purposes and signifies that it can be trusted to protect against falling dirt, directed water streams, entry of water during prolonged submersion and offers corrosion resistance. For the purposes of this experiment, the features of corrosion resistance and entry/exit of water are significant. The thermal conductivity of PVC is expected to be 0.15 W/m·K (Anderson, 1966).

3.2.2 Coil Design

The heat exchanger used a coil-in-shell design. 3/8” copper tubing was used as material for the coil. The coil was designed to maximize the heat transfer surface area based on the coil size and the box size. This was done by creating a 3D coil geometry with 5 vertical tube passes and 4 rows of tubing. The coils were bent with an Imperial 370-FH Triple Head 180° Tube Bender, which gave a bend radius of 1.125 inches for all bends. The use of a separate 3D printed nylon jig was required for some of the difficult bends in 3 dimensions.

Figure 3.2: Carlon junction box 12" x12" x 6"

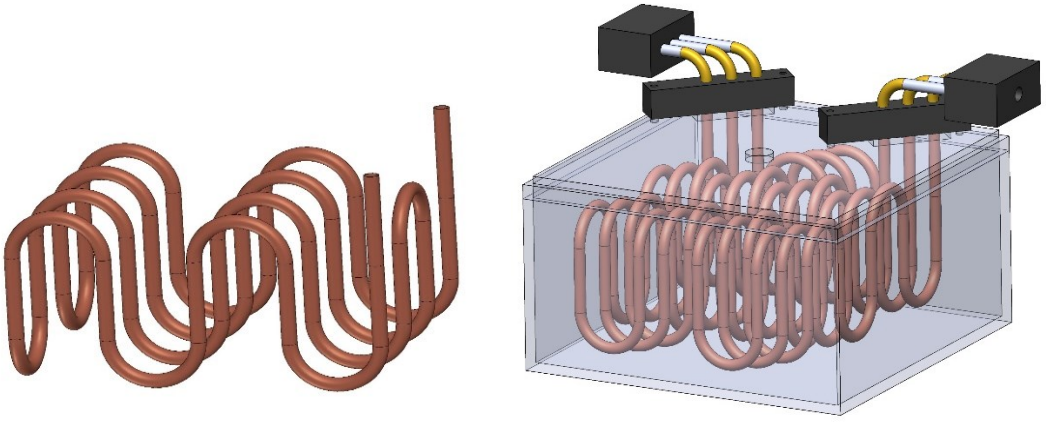

a) b)

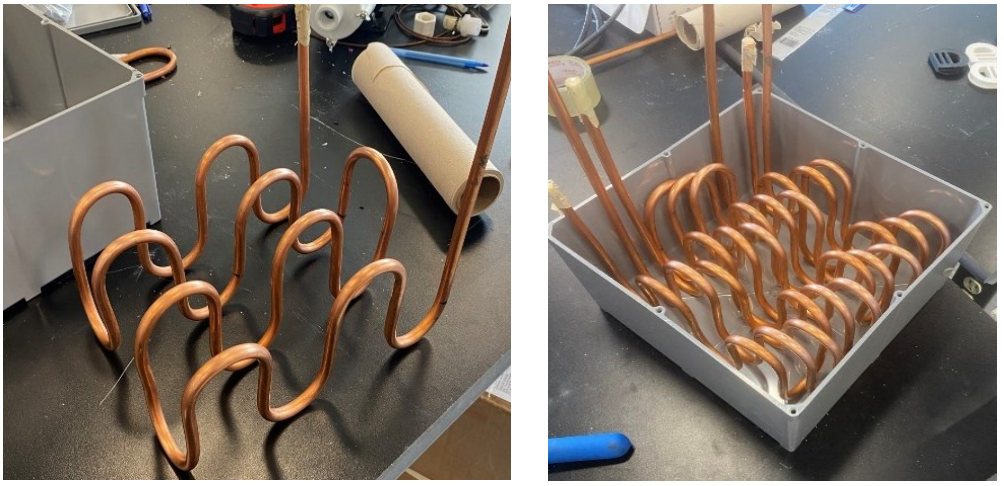

c) d)

Figure 3.3: Coil in shell geometry; a) coil CAD design b) box CAD design c) single coil d) 3 coils in box

An engineering drawing of this jig can be seen in Appendix-A. Figure 3.3 shows both a CAD design as well as photos of the coil used in the system. Three total coils were fitted to the lid of the box, as shown in Figure 3.3b), by using compression fittings and an aluminum block with tapped threads. The coils were evenly spaced apart by 0.62" and layered without contacting one another in the box. Figure 3.4a) and b) show a dimensioned drawing of the coil demonstrating its design. Figure 3.4c) shows the configuration of the coil within the box, including its dimensioned spacing. A complete engineering drawing of the coil design with dimensions can also be seen in Appendix-A.

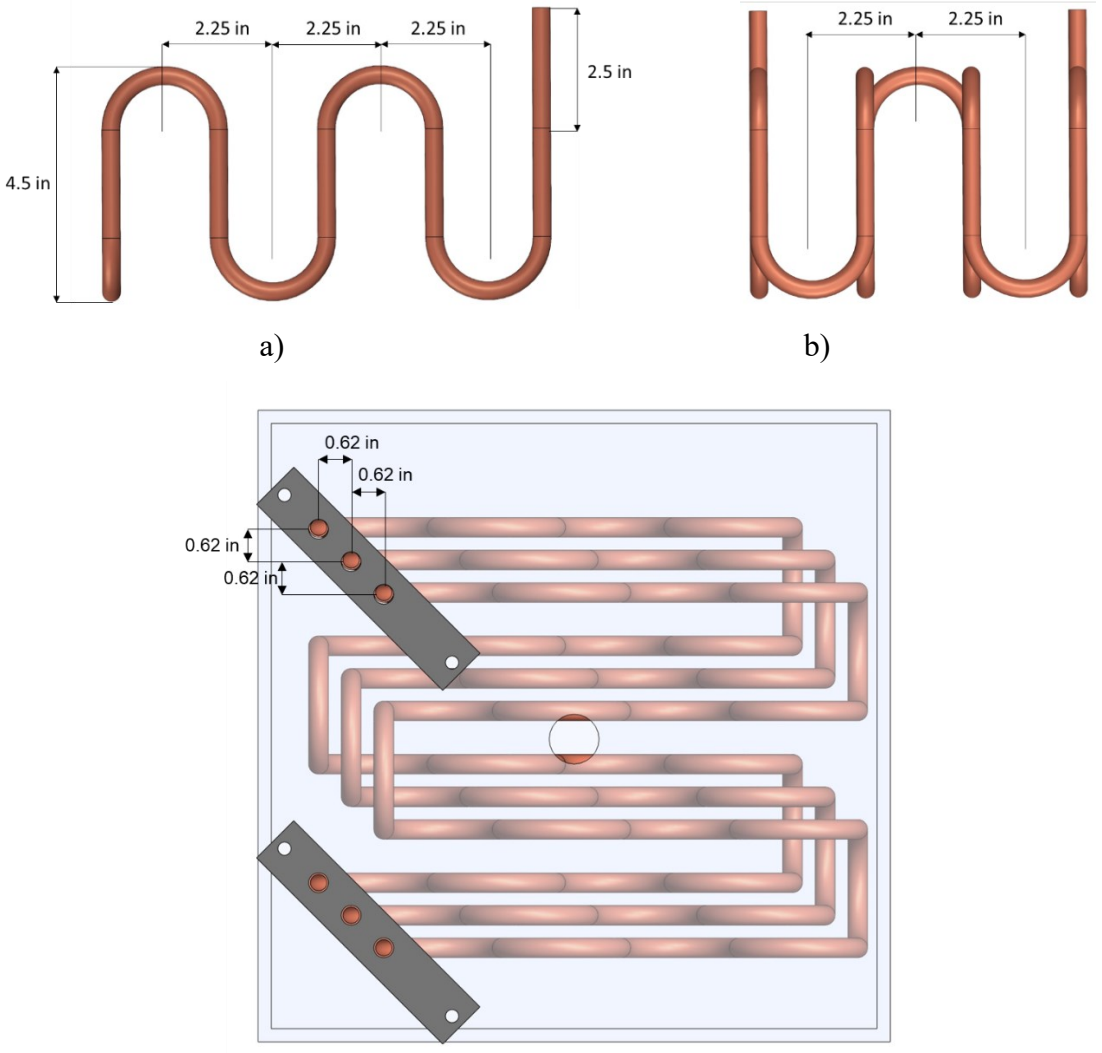

a) b)

c)

Figure 3.4: a) Front b) side and c) top view of the coil(s) with various dimensions

3.2.3 Insulation

To minimize losses between the system and the room, insulation of various types was applied to the container housing the PCM. Rigid polystyrene extruded insulation, 0.5” thick with a thermal resistance of R-5 per inch of thickness was adhered to the exterior of the box. The box was then wrapped fully in reflective duct insulation with a thermal resistance of R-4. Finally, Owens Corning FIBERGLAS insulation, with a thermal resistance of R-12, was added to the outside of the box. The PCM heat exchanger was placed in a larger box so that insulation could be carefully layered without overflowing beyond the workbench. In previous work done at the LAMTE, Herbinger and Groulx (2022) did not insulate the tubing directly connected to the box which led to heavy losses to the environment. Therefore, for this experiment this tubing was also thoroughly insulated using foam insulation. Figure 3.5 shows the insulated heat exchanger.

a) b)

Figure 3.5: Workbench view of (a) fully insulated and (b) partially insulated heat exchanger

3.3 Workbench and HTF Setup

A workbench used in previous research work (Herbinger & Groulx, 2022; Patil, 2020; Skaalum & Groulx, 2020) was used in this experiment to carry the required equipment. The setup was used to run charging and discharging experiments for the PCM heat exchanger. The heat exchanger was mounted atop the workbench and tubing was affixed to the sides of it. Figure 3.6 shows a CAD diagram as well as a photo of the entire experimental setup.

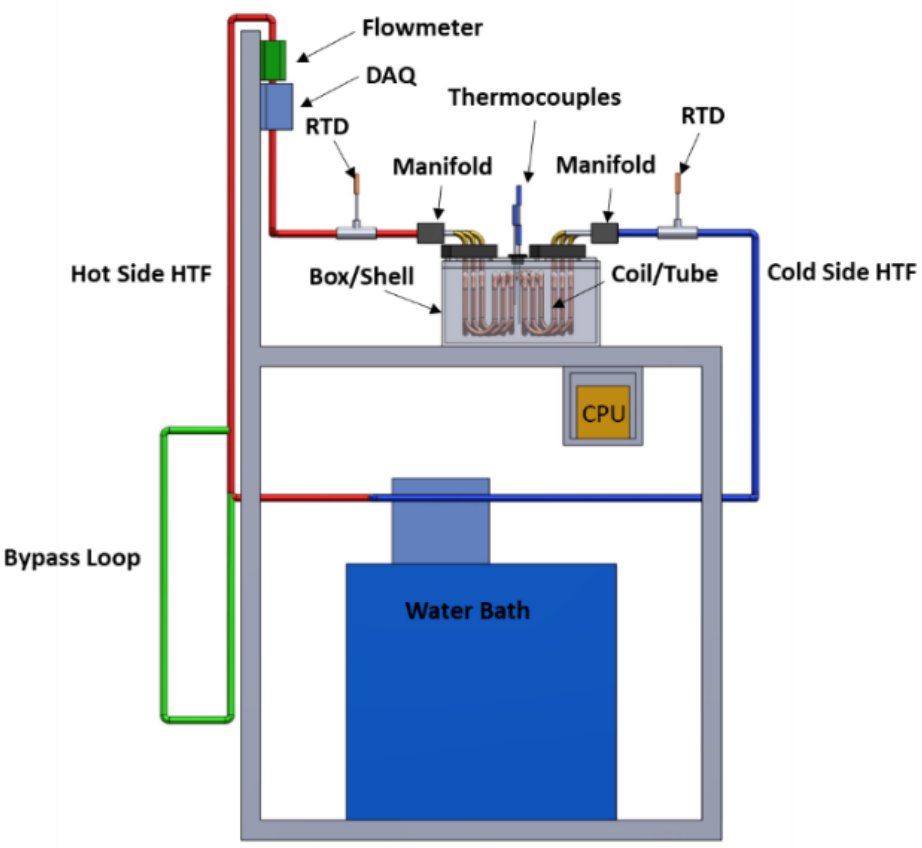

a)

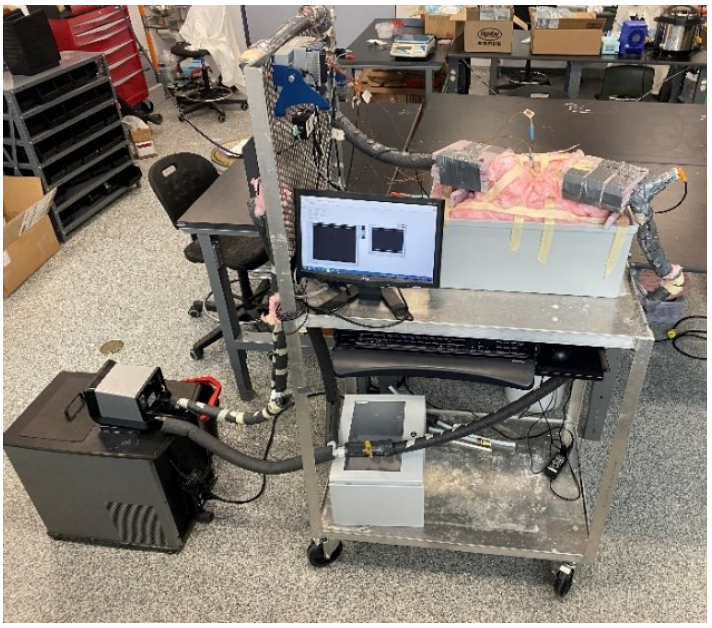

b)

Figure 3.6: Experimental setup a) CAD diagram b) photo of physical setup

3.3.1 Circulating Thermal Bath

A Polyscience Circulating Bath with Standard Digital Temperature Controller (model no. SD15R-30) was used to pump the HTF to the rest of the system. The bath has a tank capacity of 15 litres and can be operated from temperatures of -30°C to 170°C. The temperature stability in the bath is ± 0.04°C. The bath contains a built-in two speed pressure pump which has a maximum pressure of 3.5 psi and can output a maximum flow rate of 11 LPM. The heater is rated at 1100 W. The chiller is rated for 915 W at 20°C, and 505 W at 0°C and 165W at -20°C. These values come from the specifications of the circulating thermal bath which can be seen in Appendix-B. Figure 3.7 displays an image of the circulating thermal bath used in this research.

The circulating bath was placed on the floor adjacent to the workbench setup. The bath was connected to the heat exchanger through flexible plastic tubing. Manifolds were used to connect the inlets and outlets of each coil to the HTF loop.

Figure 3.7: Polyscience SD15R-30 circulating bath

3.3.2 HTF Loop

Water was used as the HTF for this system and was circulated from the bath to the heat exchanger and back to the bath through flexible plastic tubing during each trial run. A

bypass loop was added to the system and was used to isolate the circulating bath from the heat exchanger. This was done so the circulating bath could heat or cool the HTF to the correct temperature before running it through the system. Ball valves were used to change from the main loop to the bypass loop between trials. The bath was able to bring the flow rate of the system to 3.0 LPM.

3.3.3 Booster Pump

A set of trials was conducted using a Little Giant Chemical Transfer Pump (model no. 5-MD) to boost the flow rate of the circulating heat bath, (Figure 3.8). The booster pump is rated for 1/8 horsepower and a performance of 635 GPM at 15' of head. The booster pump was installed in-line with the circulating bath via plastic tubing. Using it, the flow rate of the trials was increased to 7.5 LPM.

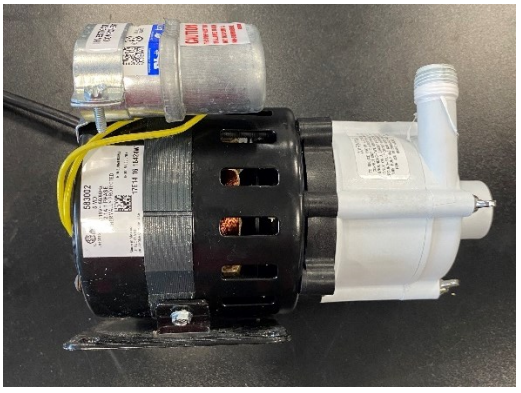

Figure 3.8: Little Giant pump (model no. 5-MD)

3.4 Sensors

3.4.1 Temperature Measurement

The temperature distribution inside the PCM was recorded by three Omega T-type thermocouple probes, 1/16" diameter and 6" length placed at various depths. Thermocouples are placed at a depth of 1.5", 3.0" and 4.5" from the top of the container in order to get an even temperature distribution throughout the entirety of the heat exchanger. Figure 3.9 shows a CAD model of the box displaying the depth of the placement of each thermocouple.

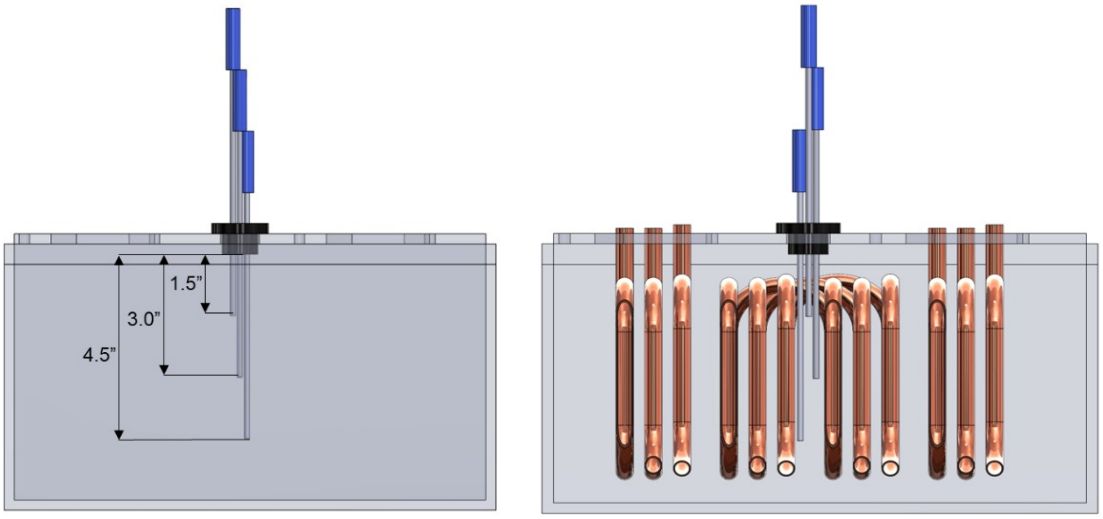

Figure 3.9: Thermocouple placement

These thermocouples were held in place by a 3D-printed nylon thermocouple holder. The holder has three 1/8" holes through which the thermocouples are inserted and held in place using adhesives. The holder was placed into the heat exchanger via a 22 mm hole cut into the top of the cover of the box. A CAD model of the holder can be seen in Figure 3.10. The use of only three thermocouples has limitations as this does not allow for a complete spatial temperature measurement approach and merely provides a sense of the overall PCM temperature.

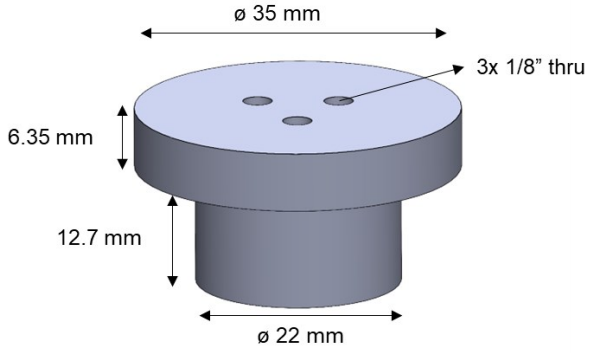

Figure 3.10: Thermocouple holder

A T-type thermocouple wire was also placed in the corner of the box to measure temperature at the furthest point from the heat exchanger tubing in order to determine when the system has fully melted or solidified in each experiment. A second T-type thermocouple wire was used to measure the ambient temperature in the laboratory. These thermocouples have an accuracy of ± 0.5 °C. The inlet and outlet temperatures of the HTF were measured

using two Omega brand RTD Probe sensors, (model no. PR-22-3-100-A-1/8-0300-M12). The RTDs were of 1/8” diameter and 3” length with an uncertainty of ± 0.28 °C.

3.4.2 Flow Rate Measurement

Flow rate is measured by a BV2150 Vision Turbine flowmeter (Figure 3.11), which operates using a mechanical rotor that sends pulses representing a discrete volume of water. The frequency of these pulses occurring is proportional to flow rate. The output frequency signal of the flowmeter can be translated into a flow rate in litres per minute using the turbine k-factor of 2200 pulses per litre. The flowmeter has a range of 1 to 15 LPM with an uncertainty of ± 3% within this range and can operate over temperatures ranging from -20°C to 100 C. Observing the flow rate measurement during trials lead to an observed random error of ± 0.5 LPM. The error of the measurement in the flowmeter was therefore greater than the manufacturer attributed uncertainty. For this reason, this observed error of 0.5 LPM was used in place of the uncertainty of the flowmeter in the further uncertainty calculations.

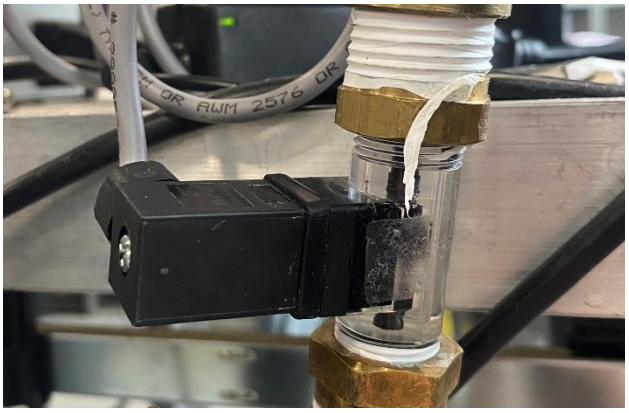

Figure 3.11: BV2150 Vision turbine flowmeter

3.4.3 Temperature Measurement Calibration

Thermocouples and RTDs were calibrated using a Fluke Calibration 7102 MicroBath with a range of -5°C to 125°C. The calibration bath is accurate up to ± 0.25°C and has a stability of ± 0.015°C at -5°C and of ± 0.03°C at 125°C. The uniformity of the bath is 0.02°C. The temperature measuring devices were calibrated between 10°C and 90°C.

When considering the power calculations of the system, however, the temperature difference is measured by taking the difference between the inlet and outlet RTD measurements. This means that the uniformity of the bath (± 0.02°C) would be the sole uncertainty of this ΔT calculation. Calibration data for the thermocouples and RTDs was recorded in LabView and the deviations from the various setpoints, as seen in Table 3.3, were used to form the calibration curve. The ambient temperature thermocouple was uncalibrated, and it is therefore deemed to have an accuracy of ± 0.5 °C as per the manufacturer.

Table 3.3: Calibration values for thermocouples and RTDs

Reference	T_corner	T_bottom	T_middle	T_Top	RTD_in	RTD_out
Recording variations from set points in degrees Celsius (°C)						
10.00	-0.04	0.14	-0.03	-0.06	0.02	-0.03
15.00	-0.03	0.11	-0.04	-0.07	0.05	0.01
20.00	-0.07	0.03	-0.10	-0.11	0.01	0.00
25.00	-0.06	0.01	-0.09	-0.11	0.14	0.10
30.00	-0.01	0.02	-0.06	-0.08	0.17	0.12
35.00	0.00	-0.02	-0.06	-0.07	0.22	0.17
40.00	0.03	-0.03	-0.05	-0.05	0.25	0.19
45.00	0.05	-0.05	-0.04	-0.06	0.27	0.21
50.00	0.06	-0.08	-0.05	-0.05	0.30	0.24
55.00	0.10	-0.09	-0.01	-0.01	0.32	0.26
60.00	0.09	-0.14	-0.03	-0.04	0.32	0.27
65.00	0.16	-0.12	0.01	0.00	0.33	0.28
70.00	0.17	-0.15	0.00	-0.01	0.33	0.28
75.00	0.23	-0.13	0.05	0.05	0.34	0.30
80.00	0.27	-0.14	0.07	0.07	0.35	0.31
85.00	0.27	-0.18	0.05	0.04	0.36	0.32
90.00	0.30	-0.19	0.06	0.06	0.36	0.33

3.4.4 Data Acquisition

A National Instruments Ni-cDAQ-9174 chassis was used to record all experimental measurements from the trials. A total of three input modules were used in order to record the various measurements of the sensors. A NI 9213 module was used to record both wire and probe-based thermocouple data. A NI 9217 was used to record the data from the two

RTDs. A NI 9402 flow rate input module was used to record flow data. The chassis was connected to a PC using LabView Instrument Engineering Workbench as the interface for the data. LabView allowed for a real time data interface in order to view flow rate and temperature data, as well as time-based data plots while experiments were occurring. It was also used for conversions of the flowmeter measurements and output of the data as a Microsoft Excel file. The data was recorded at a rate of 0.25 Hz or every 4 seconds. The chassis and modules can be seen in Figure 3.12.

Figure 3.12: Ni-cDAQ-9174 chassis and modules

3.5 Experimental Procedure

Trials for this experimental work were conducted by completing the following set of steps:

- First, initialize the PCM temperature by turning on the water bath to the correct initial temperature and allowing it to pump HTF through the heat exchanger until it is reached.
- Once the PCM is at the initial temperature (verified using the thermocouples embedded in the PCM) the water bath is changed over from the heat exchanger main loop to the bypass loop using valves.

- The water bath is then set to the final temperature, allowing all of the HTF to reach the final temperature within the bypass loop.
- After the HTF has reached the final temperature, the HTF is allowed to flow back through the main loop as simultaneously the LabVIEW program is started, recording the data.
- The trials are allowed to run for a minimum of 15 hours to ensure full charging/discharging of the system as no notable change to the PCM temperature is observed after this time.
- Once it is ensured that the PCM has reached the final temperature (by measuring the PCM temperature using the thermocouples) the trial is complete and the system is prepared for the next experimental run, essentially starting back at the top of this list.

This experimental procedure was repeated for each of the charging and discharging experiments for each type of PCM experimented upon.

3.5.1 Experimental Operating Parameters

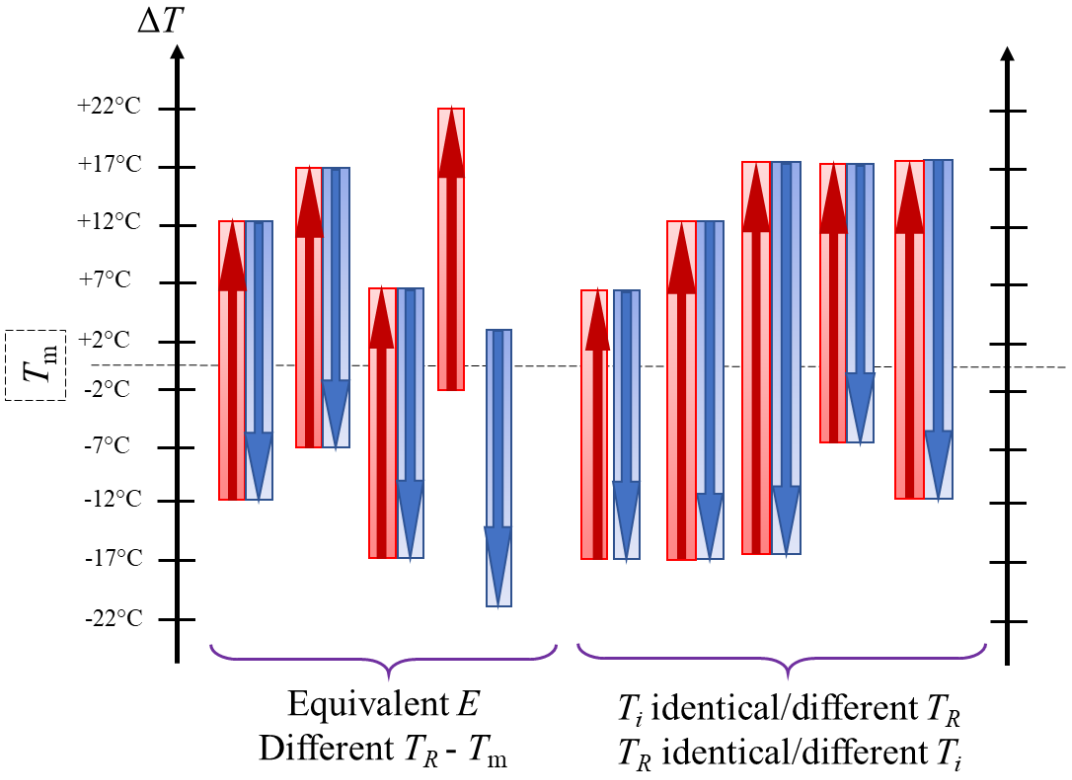

Figure 3.13: Charging and discharging experimental trials based on the melting temperature

Two different types of experiments were performed as Figure 3.13 presents. The first type includes trials with a constant temperature change between initial PCM temperature and final HTF temperature, meaning equivalent energy is stored by the PCM (both from latent and sensible sources). The second set of experiments consists of trials with equal initial temperatures (both for charging and discharging) but varied final HTF temperature. Both the flow rate and the geometry of the heat exchanger remain constant for each set of experiments. The trial temperatures for each PCM were designed in relation to the individual PCM's melting point. Table 3.4 presents the initial and final temperatures involving dodecanoic acid and 1-octadecanol for each experimental trial. A 14°C offset accounted for the difference in their melting points (43°C for dodecanoic acid and 57°C for 1-octadecanol).

Table 3.4: List of experiments run for both PCMs

Type of Experiment	Dodecanoic acid		1-octadecanol	
	T_i	T_R	T_i	T_R
Discharging	55	26	69	40
Charging	26	55	40	69
Discharging	60	26	74	40
Charging	26	60	40	74
Discharging	50	26	64	40
Charging	26	50	40	64
Discharging	60	31	74	45
Charging	31	60	45	74
Discharging	55	31	69	45
Charging	31	55	45	69
Discharging	60	36	74	50
Charging	36	60	50	74
Discharging	45	21	59	35
Charging	41	65	55	79

Trials with increased flow rates were also performed for dodecanoic acid. Using the in-line booster pump described in Section 3.3.3, the flow rate was increased from 3.0 LPM to 7.5 LPM. The entire set of trials listed in Table 3.4 for dodecanoic acid were repeated for these high flow rate trials.

3.6 Power and Energy Calculations

3.6.1 Power

The thermal power transferred to and from the PCM system is calculated using the following relations:

$$Q_c(t) = \dot{m}c_p(T_{in} - T_{out}) \tag{3.1}$$

$$Q_d(t) = \dot{m}c_p(T_{out} - T_{in}) \tag{3.2}$$

where $Q(t)$ is the instantaneous power out of the heat exchanger for charging and discharging experiments, $\dot{m}$ is the mass flow rate of the system, calculated from the measured volumetric flow rate multiplied by the temperature dependent density of the HTF, c_p is the temperature dependent specific heat capacity of the HTF, and T_{in} and T_{out} are the inlet and outlet temperatures of the heat transfer fluid respectively. For charging, instantaneous power is calculated by subtracting the inlet temperature from the outlet temperature while for discharging power is calculated by subtracting the outlet temperature from the inlet temperature.

3.6.2 Heat Loss/Gain

The inevitable loss or gain of heat from the environment to the system must be accounted for in calculating the power and energy stored in the system. Following the approach taken by Skaalum and Groulx (2020), the heat loss or gain of the system is defined by using the assumption that the heat transfer process of the LHTES system reached a steady state at the end of each trial. The power of the system at the end of the trials is then taken to be equivalent to the heat loss or gain at the end of the trial. This value is assumed to be constant for the duration of the trial. The loss or gain is added or subtracted from the measured power in order to get an adjusted heat transfer value which would more accurately define the heat transferred into the system.

$$Q_{adjusted} = Q_{measured} + Q_{loss} \tag{3.3}$$

$$Q_{adjusted} = Q_{measured} - Q_{gain} \tag{3.4}$$

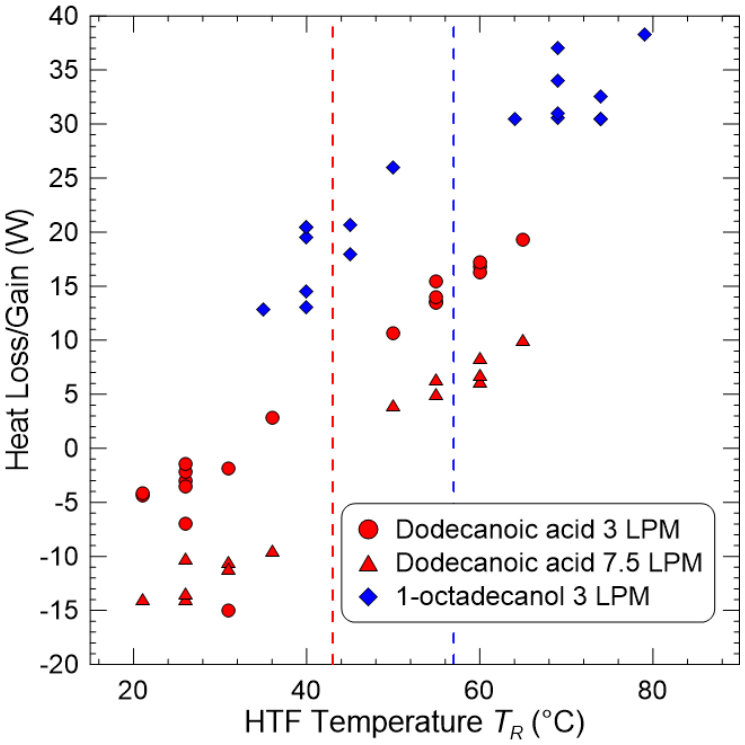

Figure 3.14: Heat loss/gain plot

Figure 3.14 demonstrates the heat loss or gain value from each experiment as a function of HTF temperature. Negative power values signify a heat gain and are apparent for temperatures near or below ambient temperature. The results show a linear trend for each set of trials and the slope of each data set appears to be equivalent. This is logical as the heat loss is determined solely by the temperature difference between the system and the surroundings meaning that as the system temperature increases so should the heat loss, as per Newtons Law of cooling seen in Equation 3.5. The 1-octadecanol trials show much higher values of heat loss compared to the dodecanoic but this is also expected due to the higher operating temperatures observed. The high flow rate trials exhibit a smaller heat loss compared with the low flow rate trials and a larger heat gain. This could be caused by a heat addition from the in line booster pump used to increase the flow rate.

$$Q = h \cdot A(T(t) - T_{amb}) \tag{3.5}$$

3.6.3 Energy

The energy stored or released from the system is defined by integrating the measured power over the total duration of the experiment.

$$E = \int_{t_{initial}}^{t_{final}} Q_{adjusted}(t)dt \tag{3.6}$$

This calculation is performed in practice using a summation of the instantaneous power values measured multiplied by the constant time difference between data recordings of 4 seconds.

$$E = \sum_{i=1}^{n} \Delta t \cdot Q_{i,adjusted}(t) \tag{3.7}$$

The theoretical energy that the system can store, or discharge can also be calculated using the known thermophysical properties of the PCM and the operating temperature range. There are two components of the energy storage of the PCM, the sensible energy and the latent energy.

$$\begin{aligned} E_{total} &= E_{latent} + E_{sensible} \\ &= m_{pcm}L + m_{pcm}\left(c_{p,s}(T_m - T_c) + c_{p,l}(T_h - T_m)\right) \end{aligned} \tag{3.8}$$

where m_{pcm} is the mass of the PCM, L is the latent heat storage of the PCM, $c_{p,s}$ is the specific heat of the solid state of the PCM, $c_{p,l}$ is the specific heat of the liquid state of the PCM, and T_m is the PCM melting temperature. In charging experiments, T_c represents the initial PCM temperature, and T_h stands for the HTF temperature. Conversely, in discharging experiments, T_h corresponds to the initial PCM temperature, while T_c denotes the HTF temperature.

3.6.4 Uncertainty Analysis

The uncertainty of the power calculation is made up of two variables, the uncertainty of the mass flow rate, which comes from the flow meter uncertainty of ± 0.5 LPM, as discussed in Section 3.4.2, and the uncertainty of the temperature difference, which was determined from Section 3.4.3 to be ± 0.02°C. The specific heat and density are calculated using curve

fits for water in the range of 0°C to 100°C and are therefore considered to be highly accurate (White & Xue, 2021). The relative uncertainty was calculated using the root sum squared methodology adopted by Kline and McClintock (Moffat, 1988).

$$\frac{\delta Q}{Q} = \sqrt{\left[\left[\frac{\delta \dot{V}}{\dot{V}}\right]^2 + \left[\frac{\delta \Delta T}{\Delta T}\right]^2\right]} \tag{3.9}$$

$$\frac{\delta Q}{Q} = \sqrt{\left[\left[\frac{0.5}{\dot{V}}\right]^2 + \left[\frac{0.02}{\Delta T}\right]^2\right]} \tag{3.10}$$

For a typical ΔT at the beginning of trials.

$$\frac{\delta Q}{Q} = \sqrt{\left[\left[\frac{0.5}{3.303}\right]^2 + \left[\frac{0.02}{5.578}\right]^2\right]} = 0.151 \; or \; 15.1\% \tag{3.11}$$

For the calculated power of 1.27 kW correlating to this ΔT, this correlates to an absolute error of 0.190 kW or 190 W.

For the energy calculations, the uncertainty was determined by analysing the uncertainty of the two terms in the equation, power and time. The Δt was taken directly from LabView and is known to be accurate, therefore the uncertainty of this energy calculation is entirely dependant on the uncertainty of the power. The uncertainty of the energy is therefore a propagation of the absolute uncertainty of each individual energy term in the summation.

$$\frac{\delta E_j}{E} = \frac{\delta Q_j}{Q} \tag{3.12}$$

$$\delta E_{total} = \sum_{j=1}^{n} \delta E_j \tag{3.13}$$

For a trial of T_i=26°C to T_R=55°C with a total energy value of 2167.59 kJ, the uncertainty of the energy was 362.5 kJ.

Due to the decreasing heat transfer close to the end of the trials (when the systems is nearing steady state), the relative uncertainty of this temperature difference begins to trend towards

infinity as the temperature difference tends towards zero. For this reason, an adjusted uncertanty of ± 4.165 W was used for the uncertainty of the power, δQ_j, when the temperature difference was less than the uncertainty of 0.02°C. This value was calculated using the uncertainty of 0.02°C as the temperature difference in Equation (3.1), neglecting the flow rate uncertainty which would be minimal near the end of the experiment when the power exchange is also tending towards zero. This power value correlated to an energy uncertainty of ± 0.0166 kJ for the uncetainty of the individual energy term, δE_j.

Figure 3.15 demonstrates the trend of the maximum and minimum power observed for a) a charging trial and b) a discharging trial. The absolute uncertainty for each trial can be seen between the maximum and minimum power values and the relative uncertainty is plotted on the same axis. It is noted that while the absolute uncertainty is decreasing with time, the relative uncertainty is increasing throughout the trial duration. This is due to the increasingly small temperature difference values measured throughout the trial which coincide with a larger relative uncertainty.

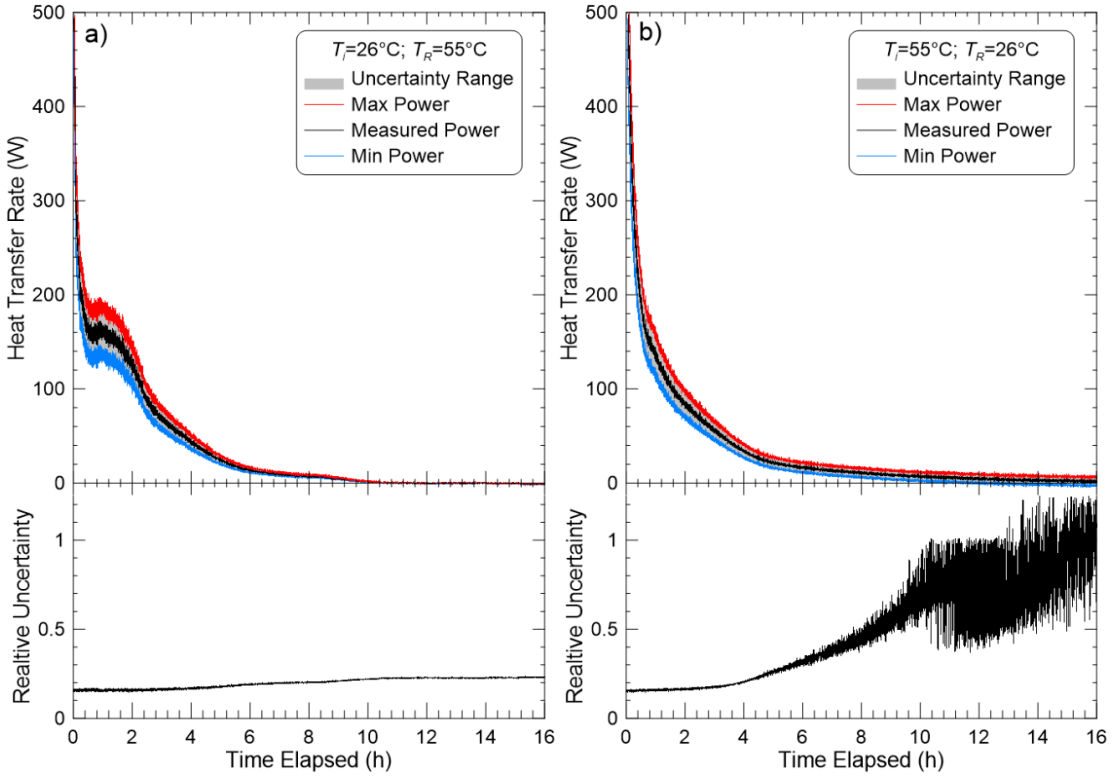

Figure 3.15: Power vs time demonstrating maximum, minimum and uncertainty values for a typical a) charging experiment and b) discharging experiment

3.7 Experiment Repeatability

Prior to conducting the full set of trials, the repeatability of the experiments was examined by running charging and discharging experiments a total of 3 times for each type of PCM. For dodecanoic acid, trials of T_i=26°C to T_R=55°C for charging and T_i=55°C to T_R=26°C for discharging were used. Graphical representations of power versus time and power versus energy were generated to illustrate these experimental outcomes. Figure 3.16 displays the results for the charging experiments, while Figure 3.17 presents the results for the discharging experiments. As seen in the plots, the results for each trial coincide almost completely with one another. This signifies that the repeatability for the dodecanoic acid trials is acceptable to a high degree.

For 1-octadecanol, trials of T_i=40°C to T_R=69°C for charging and T_i=69°C to T_R=40°C for discharging were used. Figure 3.18 displays the results for the charging experiments, while Figure 3.19 presents the results for the discharging experiments. The results for this PCM coincide with one another almost completely also, meaning the repeatability for the 1-octadecanol trials are at a high degree also.

3.8 Conclusion

The design of the experimental setup for this study was comprised of multiple constituents including: the phase change material being tested, the heat exchanger containing the PCM, the workbench and circulating HTF loop and sensors which recorded the data. The design of each of these components was thoroughly laid out in this chapter so that the experiment may be replicated in future studies. The experimental procedure and equations used to analyse the data were described in detail with emphasis on made assumptions. The following Chapters present the results of this study following the methodology displayed in this chapter.

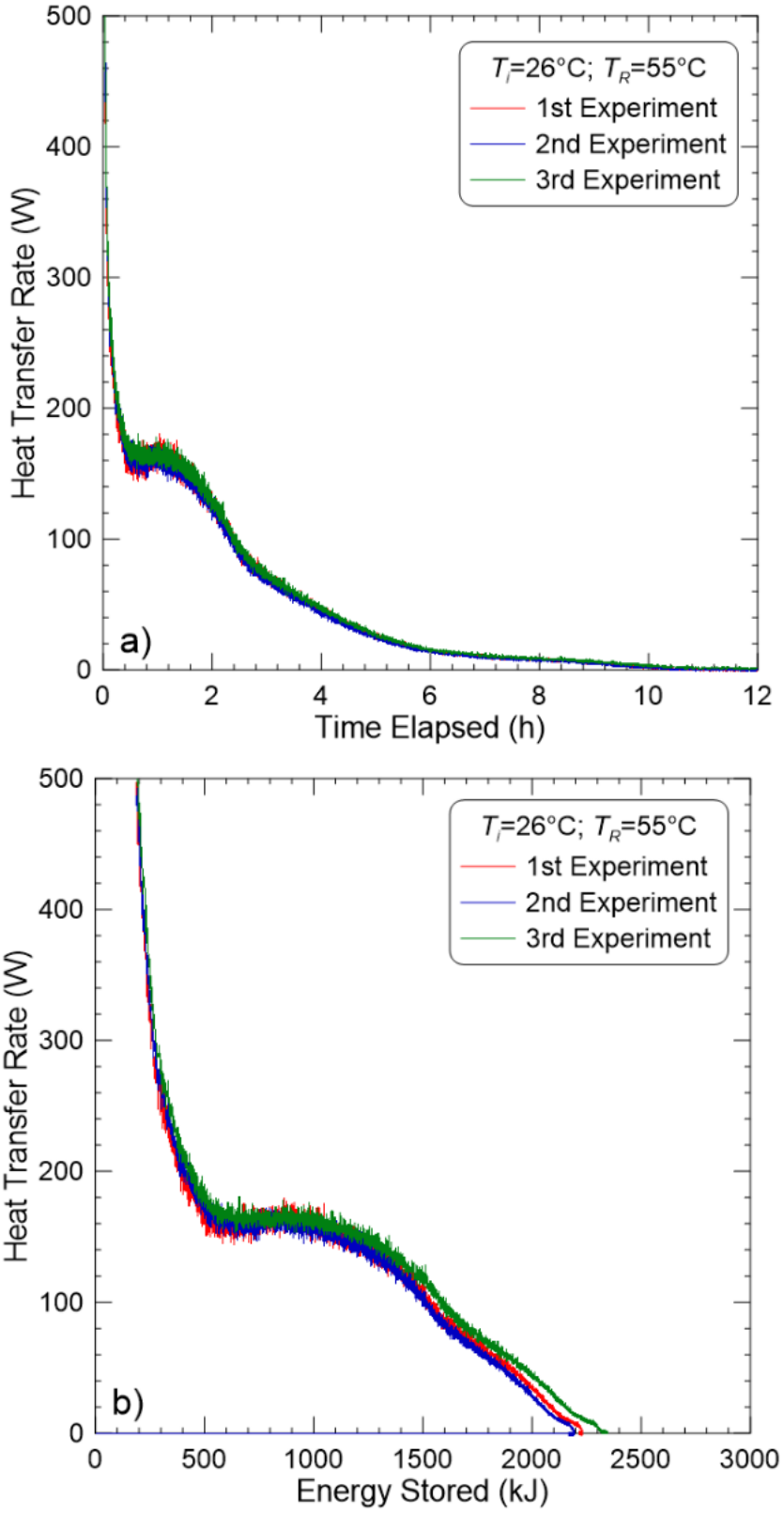

Figure 3.16: Repeatability dodecanoic acid charging experiments a) power vs time b) power vs energy

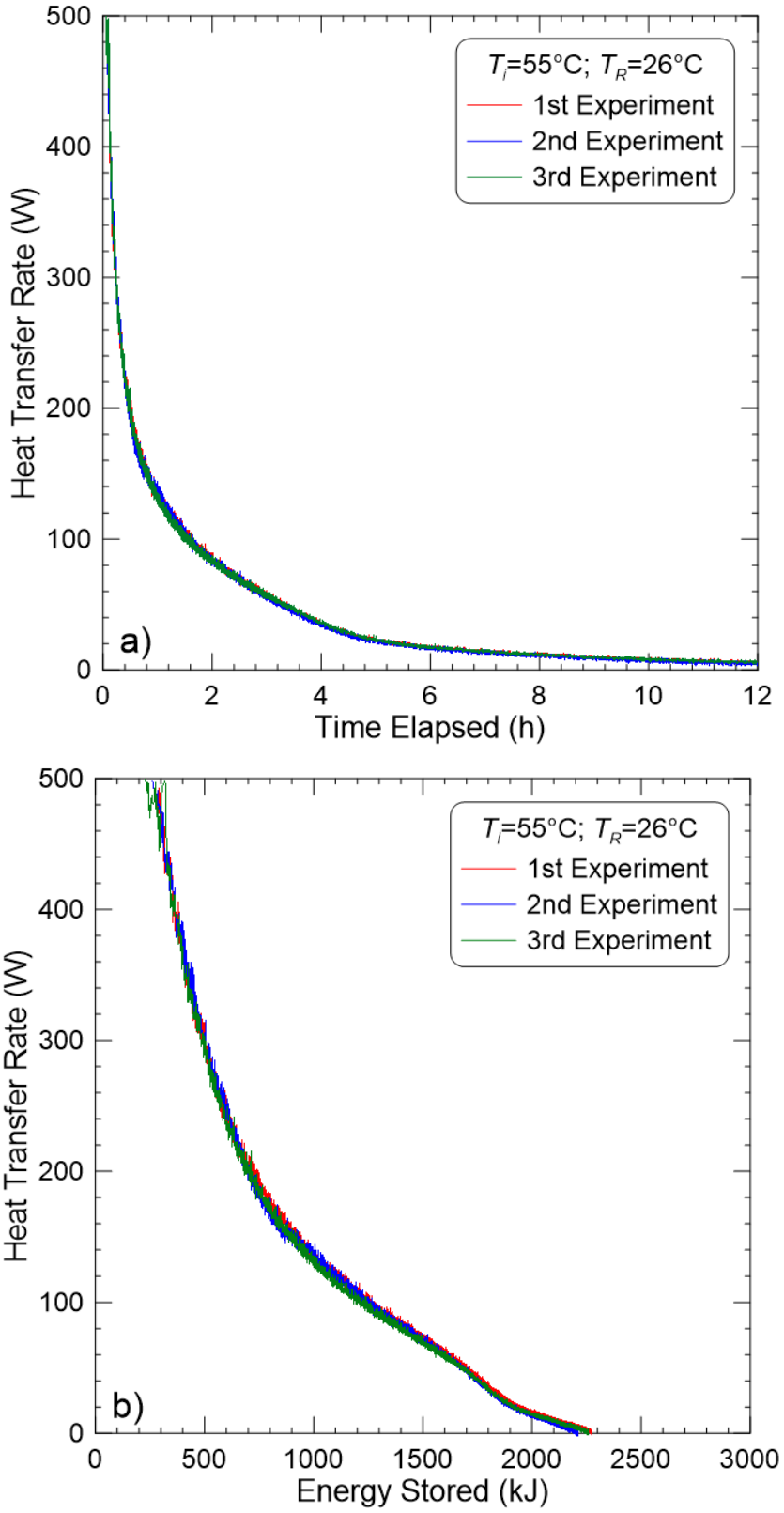

Figure 3.17: Repeatability for dodecanoic acid discharging experiments a) power vs time b) power vs energy

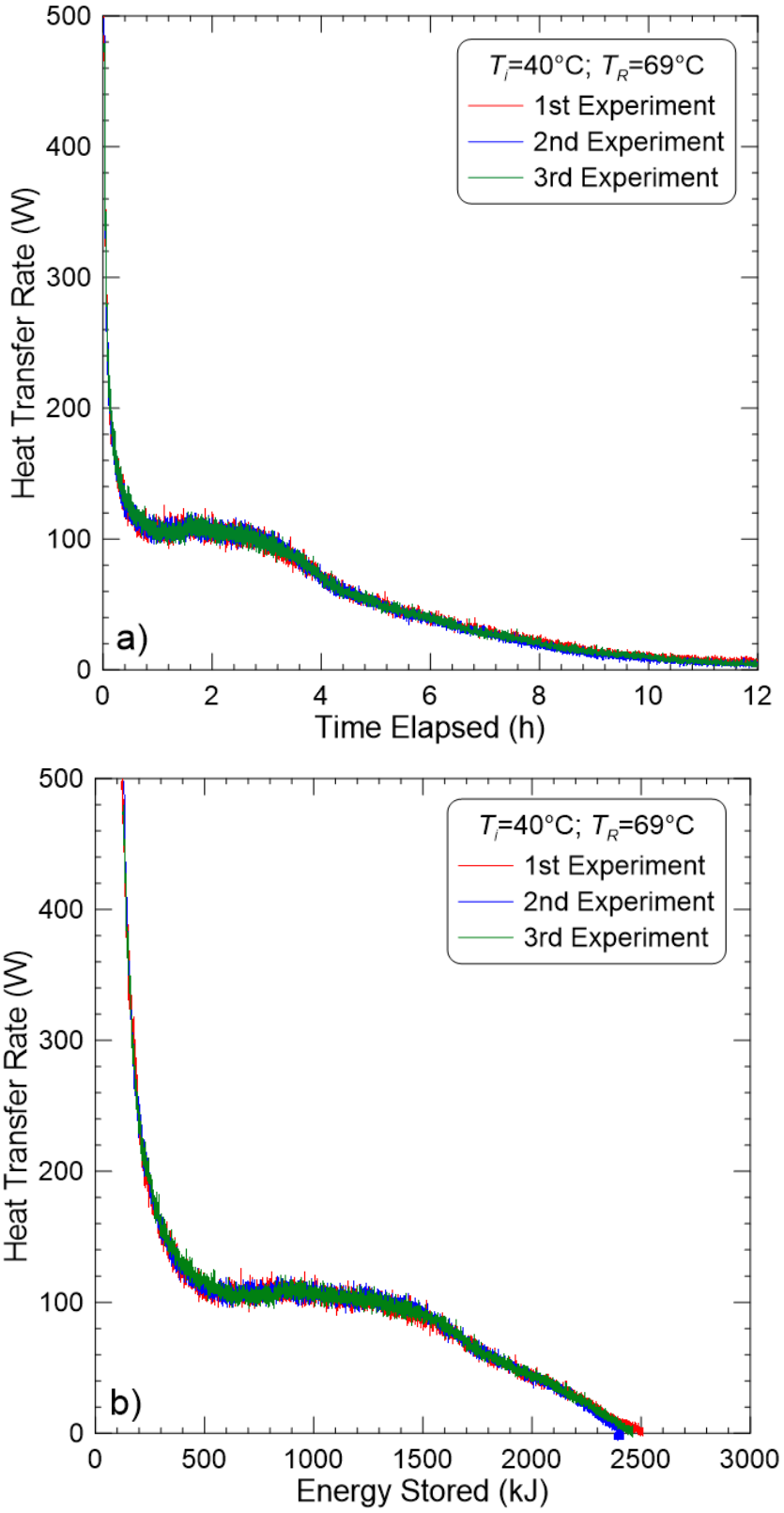

Figure 3.18: Repeatability for 1-octadecanol charging experiments a) power vs time b) power vs energy

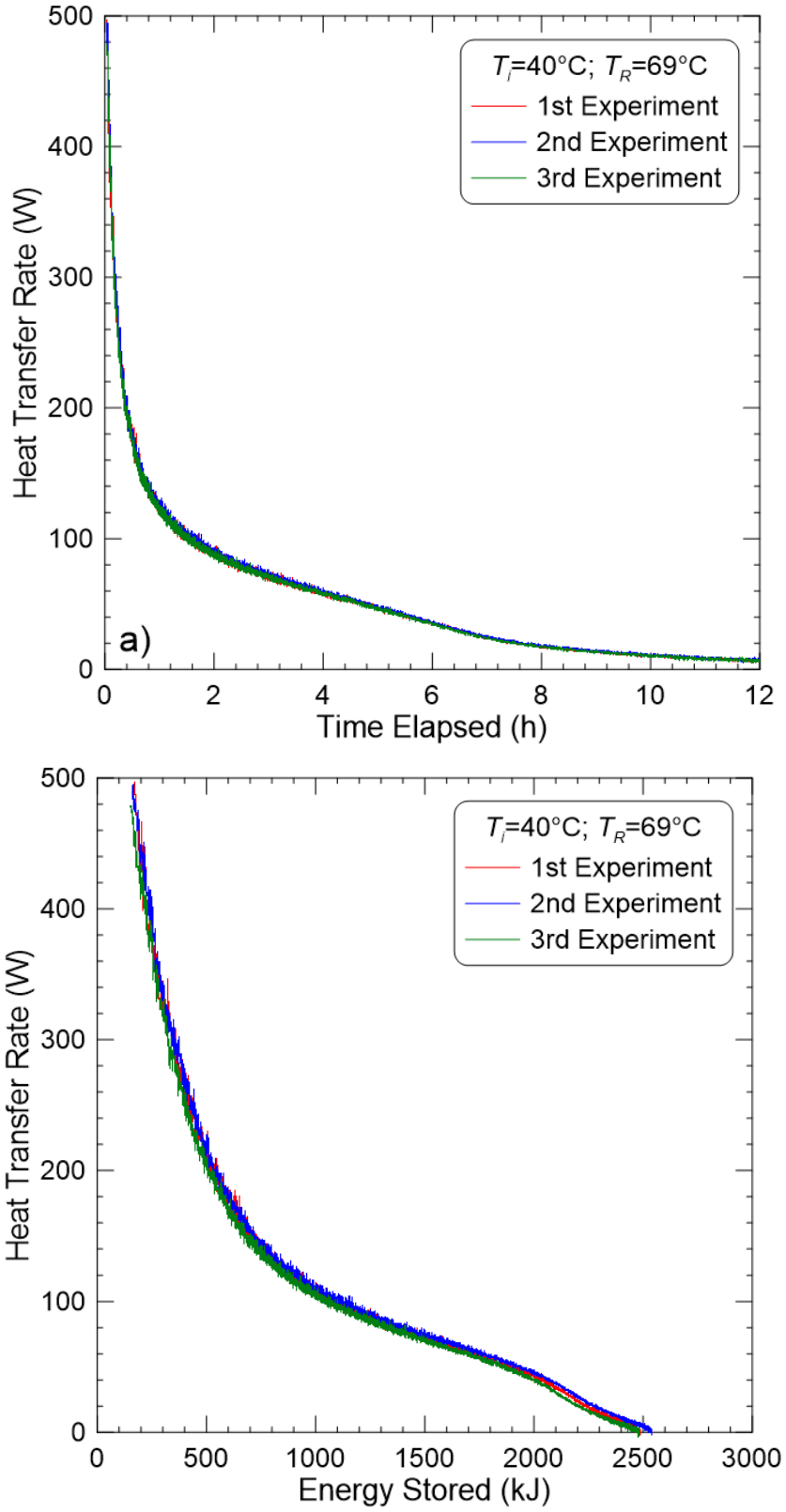

Figure 3.19: Repeatability for 1-octadecanol discharging experiments a) power vs time b) power vs energy

Chapter 4: Dodecanoic Acid Results

This chapter presents the results of the experimental trials introduced in Section 0 using dodecanoic acid as the PCM and two different HTF flow rates. Figures displaying measured temperature, calculated power and energy for both charging and discharging experiments will be presented and discussed in this chapter.

4.1 Temperature Results

Figure 4.1 a) and b) display typical trends for the temperature of the LHTES system using dodecanoic acid for charging and discharging experiments respectively. Two RTDs, one for the inlet and one for the outlet were used to obtain temperature readings of the HTF entering and leaving the heat exchanger. Three T-type thermocouple probes, mounted at various heights, were used to measure the PCM temperature within the heat exchanger and an additional T-type wire thermocouple recorded the temperature of the ambient air in the room. The experiments used for the temperature results represented were a typical charging experiment with T_i= 26°C and T_R= 55°C and a discharging one with T_i= 55°C, T_R= 26°C.

Charging results are presented in Figure 4.1 a). The hot HTF can be seen entering the heat exchanger with an inlet temperature of 55°C. The outlet temperature begins at a temperature of approximately 54°C before increasing asymptotically towards the inlet temperature. The PCM temperature in all three thermocouple positions rises rapidly immediately after the HTF enters the heat exchanger. This is due to the large difference between the cold liquid exiting the heat exchanger (which is still at the initial temperature) and the incoming HTF at the setpoint temperature. This rapid increase is followed by an infection point that coincides with the PCM's melting point, 43°C, in which isothermal phase transition occurs locally around each thermocouple. This inflection point is much more pronounced for the middle and bottom thermocouple which may be due to onset of natural convection causing the hot liquid PCM to rise to the top of the container, speeding the phase change transition as observed by the thermocouple at the top. As the experiment progresses, it is noted that the middle and bottom temperatures reach the HTF temperature while the top thermocouple temperature does not. This could be due to a greater heat loss at the top of the container due to the necessary holes cut in the box to install the fittings.

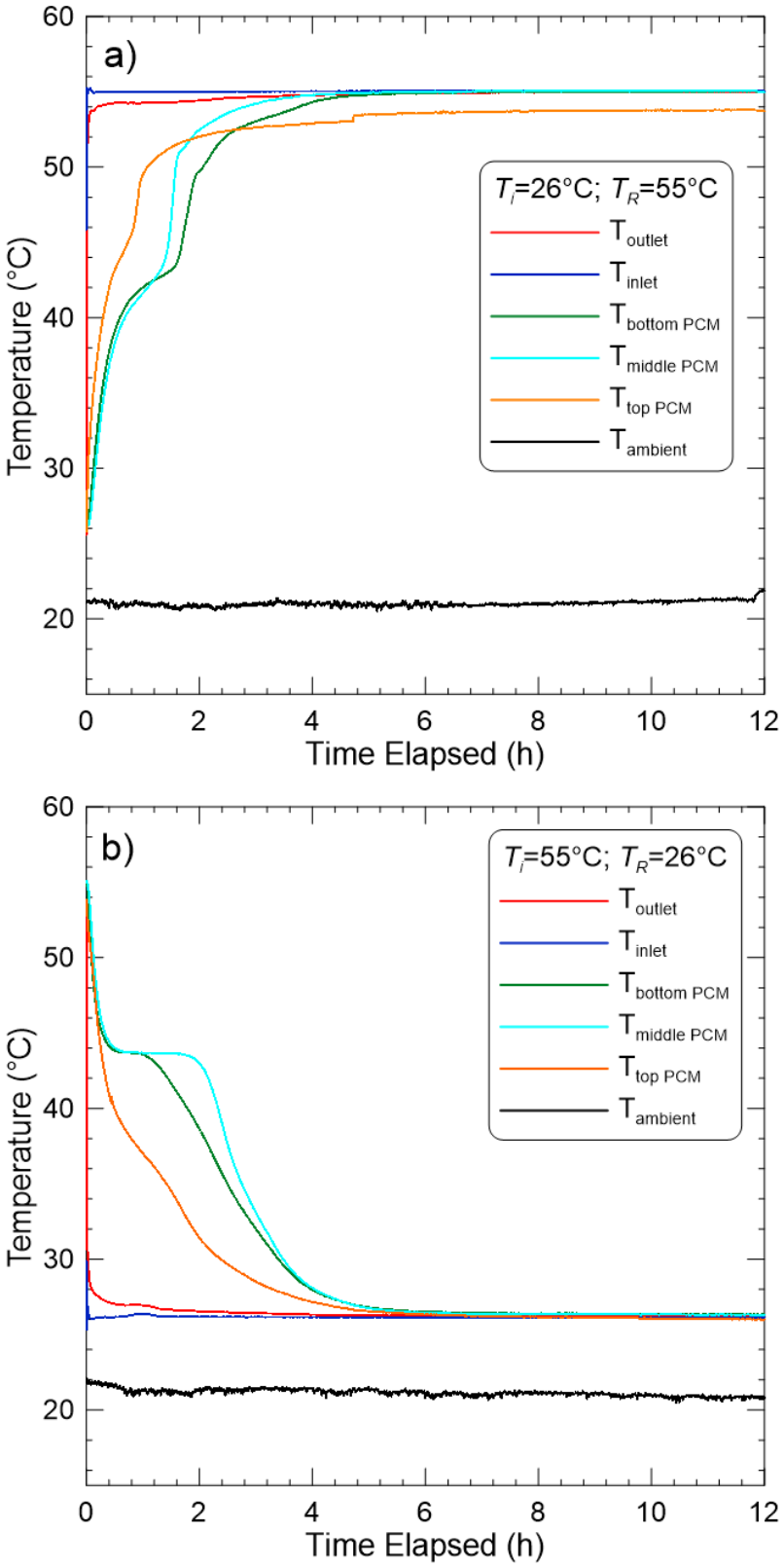

Figure 4.1: Typical trend of various temperature sensors for dodecanoic acid a) charging experiment b) discharging experiment

This can also be attributed to a small layer of air which may act as an insulator at the top of the container, as the container was not able to be filled completely with PCM due to leakage concerns. The ambient temperature for this trial is constant at 21°C.

The discharging results presented in Figure 4.1 b) shows the temperature of the cold HTF at the inlet at 26°C as it enters the heat exchanger. The PCM temperature observed in each thermocouple position decreases rapidly at the commencement of the trial, only to reach a plateau at 43°C when the PCM begins to change phase. This isothermal phase change is much more prevalent in the middle thermocouple compared to the top and bottom ones, this is due to the nature of the geometry of the coil as its bends cause there to be much more surface area near the top and bottom of the heat exchanger. This is displayed clearly in Figure 3.9, with the top thermocouple being 0.745" from the top coil bends and the bottom thermocouple being 0.745" from the bottom coil bend. The middle thermocouple is 2.25" away from either coil bend and therefore is affected less by this increase in surface area. The outlet temperature begins slightly higher than the HTF inlet temperature value at approximately 28°C, however this value begins to decrease as the trial continues until it reaches a value only slightly higher than that of the inlet. All three thermocouple probe values eventually reach steady state at a temperature equivalent to the HTF temperature. Ambient temperature appears to be constant at approximately 21°C for the duration of the trial.

4.2 Charging Results

Results of instantaneous heat transfer rates for charging experiments are calculated using the method discussed in Section 3.6.1 and are plotted against the cumulative energy stored in the LHTES system similarly to the method of Patil (2020). Plotting against the state of charge of the experiment, rather than the duration of the experiment better displays the significant characteristics of the heat transfer curves. Figures 4.2, 4.3 and 4.4 presents the results for charging experiments and display the common trends of all charging experiments. As the heat transfer fluid enters the heat exchanger, the heat transfer increases instantaneously to values greater than 500 W. This is due to the HTF being at or near the initial PCM temperature, which exits the system leading to an extremely large temperature

differential between this cold outlet and the warm inlet. The heat transfer then decreases rapidly as the PCM temperature begins to increase until it reaches the PCM melting temperature. An inflection point is observed in the heat transfer demonstrating the effect of increased heat transfer caused by the onset of natural convection as the PCM begins to melt. This inflection point is followed by a plateau of the heat transfer which signifies the isothermal melting process accelerated by natural convection. The heat transfer then begins to decrease more gradually until the system reaches a state of full charge, at which time the heat transfer value goes to zero.

Figure 4.2, demonstrates the results of charging experiments of dodecanoic acid for experiments of varying T_i and T_R but identical ΔT values, and thus identical stored energy. It is apparent from this figure that all of the experiments reach approximately the same energy. It is also clear that the experiments with higher T_R values display larger values of heat transfer rate throughout the duration of the trials.

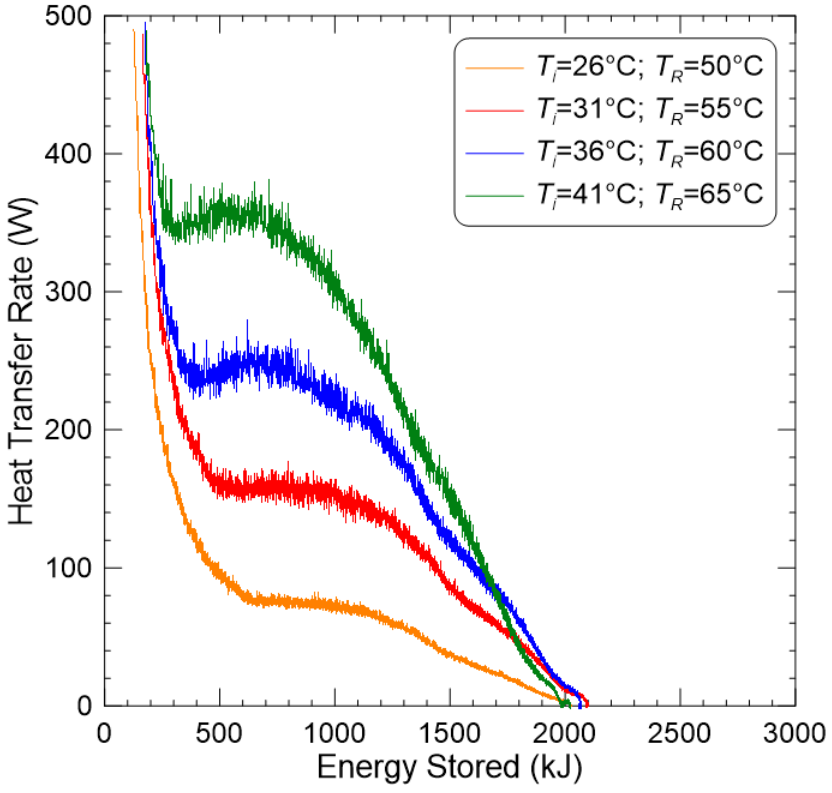

Figure 4.2: Equivalent energy charging results for dodecanoic acid

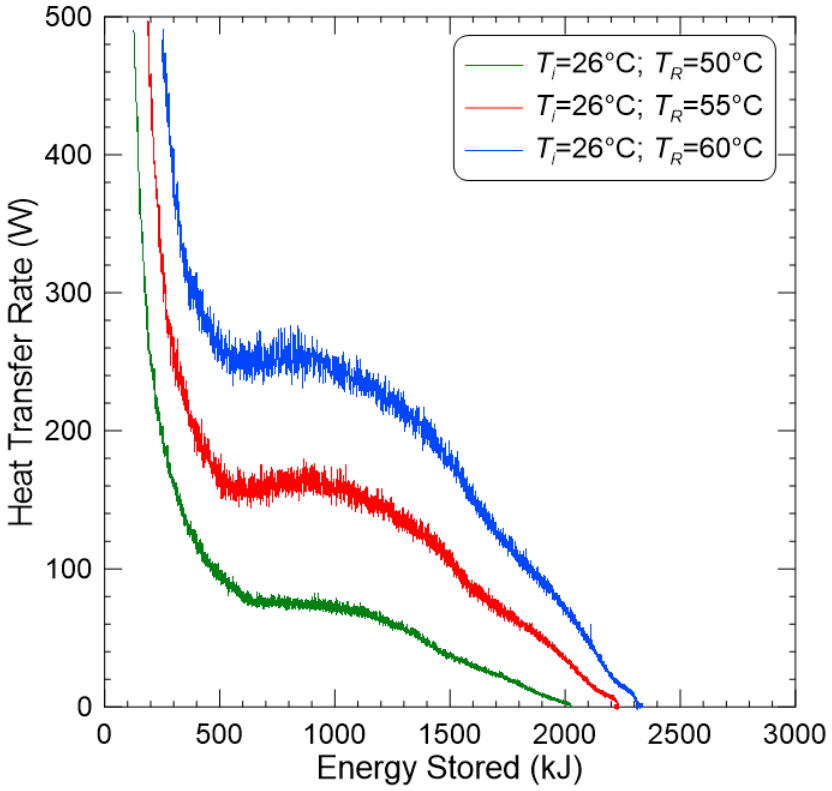

Figure 4.3: T_i identical T_R different charging results for dodecanoic acid

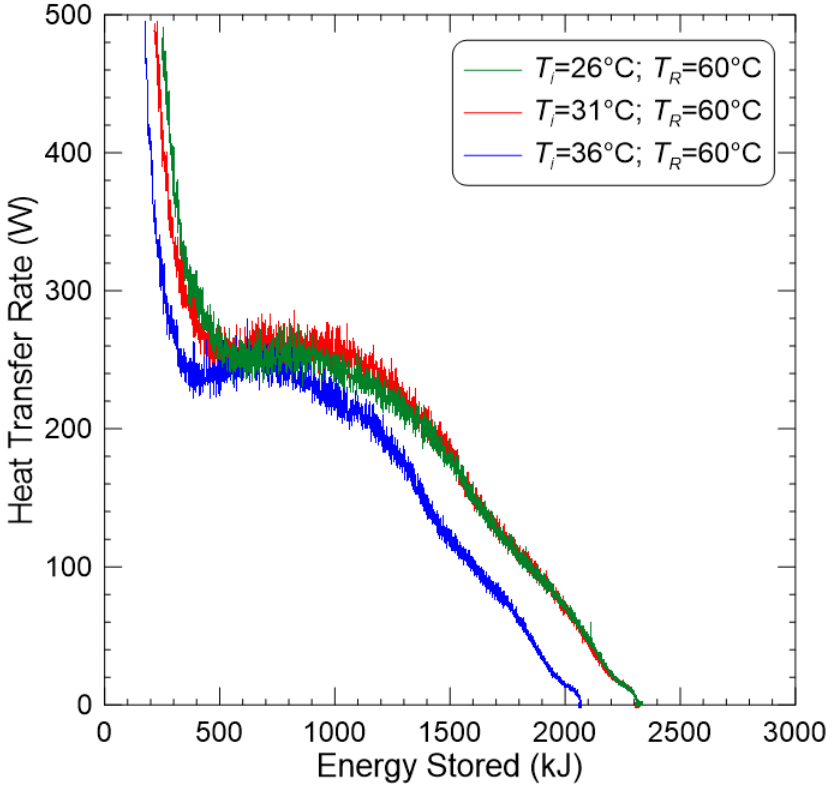

Figure 4.4: T_R identical T_i different charging results for dodecanoic acid

These conclusions are similar to what's been observed in previous research (Herbinger & Groulx, 2022; Patil, 2020). Figure 4.3 further demonstrates the effect of increasing T_R as results for identical T_i but different T_R values show augmented heat transfer with increasing T_R values. Due to the different ΔT for these figures, the total amount of energy stored is increased as T_R is increased also. Figure 4.4 shows results with identical T_i but different T_R. The heat transfer values observed from these trials are much closer in magnitude than the results from Figure 4.3. They have different ΔT as well and therefore also end at different energy values, aside from the trial of T_i=31°C to T_R=60°C which appears to be an outlier. This demonstrates that T_R is much more significant in driving the heat transfer process for charging experiments than is T_i.

4.3 Discharging Results

The results of discharging are shown in Figures 4.5, 4.6 and 4.7. Much like the charging experiments, the heat transfer rates of the discharging trials follow a typical trend. The heat transfer is dominated by conduction, and continuously decreases in magnitude as the trial progresses. This is due to the continuous decrease in temperature gradient between the constant HTF temperature and the decreasing PCM temperature as the PCM releases its energy. The solidification of liquid PCM on the surface of the HTF coils will also reduce the heat transfer effect due to the solid PCM acting as an ever-growing insulator. This effect also demonstrates the lack of natural convection in the discharging process, as the solid PCM remains stationary and restricts the fluid movement. The heat transfer eventually reaches zero when the system is fully discharged.

Figure 4.5 displays discharging results with equivalent stored energy, and thus equal ΔT values. Figure 4.6 presents results with identical T_i values but with differing T_R values. Figure 4.7 represents figures of identical T_R but different T_i values. The results demonstrate that T_R has a significant effect on the heat transfer of the system. However, it cannot be ignored that increasing the T_i causes a larger effect on the heat transfer of the system relative to other discharging results in comparison to the effect observed for the charging experiments.

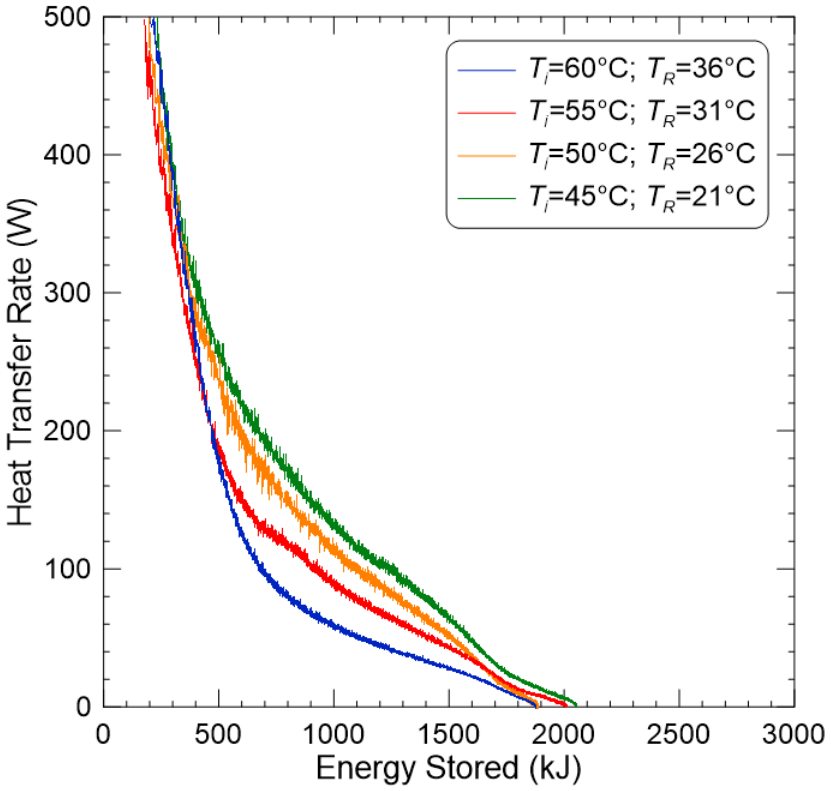

Figure 4.5: Equivalent energy discharging results for dodecanoic acid

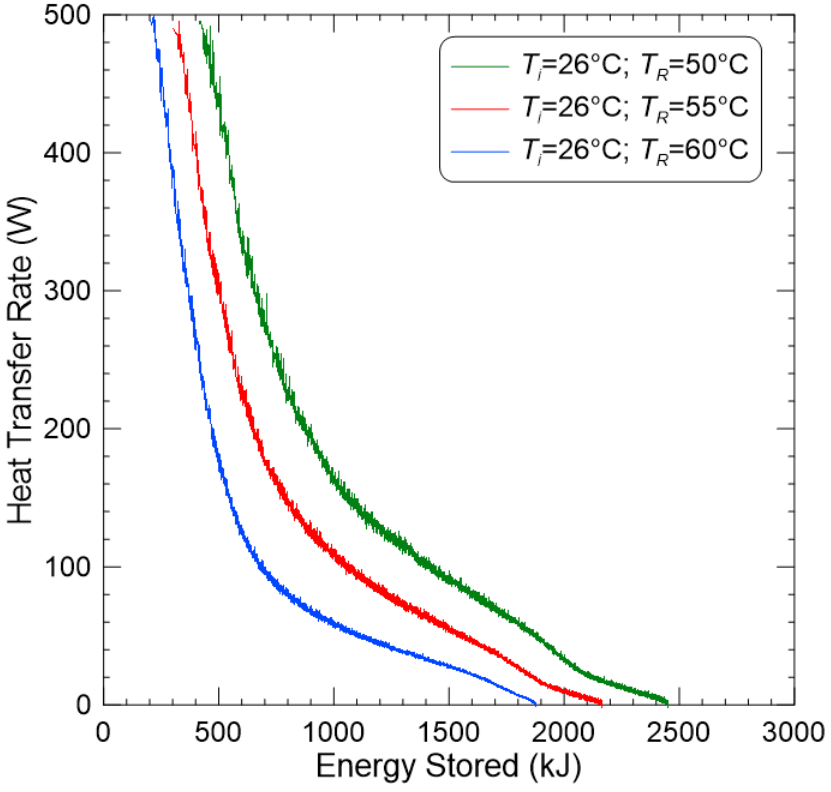

Figure 4.6: T_i identical T_R different discharging results for dodecanoic acid

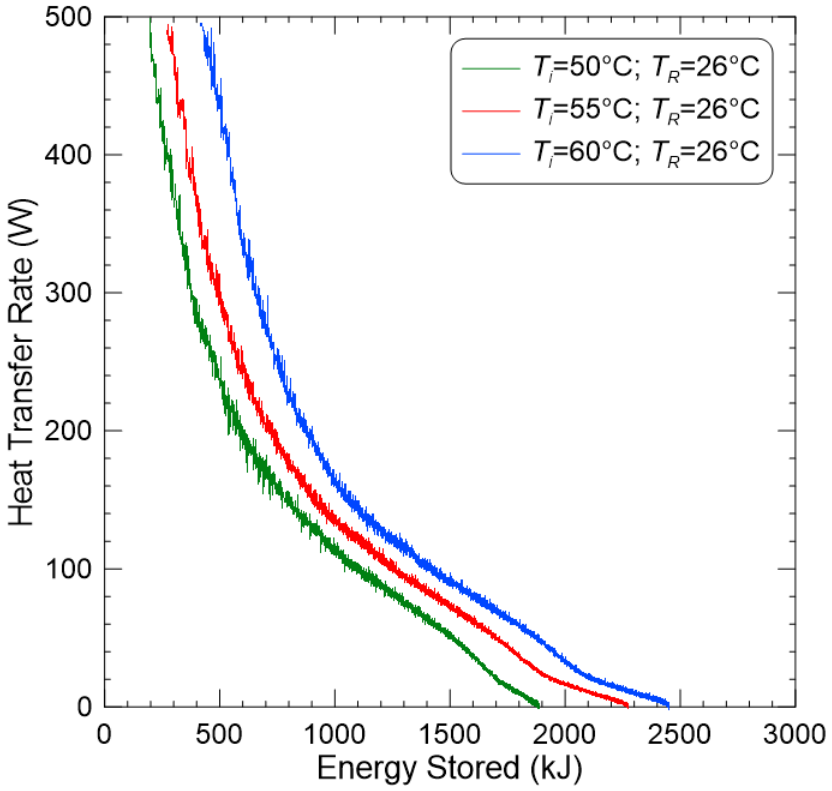

Figure 4.7: T_R identical T_i different discharging results for dodecanoic acid

Although it is clear that the T_R is the driving force of the heat transfer process for charging experiments, the effect of the ΔT, and therefore the T_i, could be more significant in the discharging experiments since this process is dominated by conduction.

4.4 High Flow Rate Results

This section analyzes discharging and charging results of dodecanoic acid with two different flow rates. The low flow rate value of 3 LPM was used for the previous experimental results presented in Sections 4.2 and 4.3. The high flow rate value of 7.5 LPM was achieved using a booster pump as described in Section 3.3.3. Figures 4.8, 4.9 and 4.10 display the charging results of the high flow rate experiments and the low flow rate experiments, while Figures 4.11, 4.12 and 4.13 present discharging results for both sets of experiments.

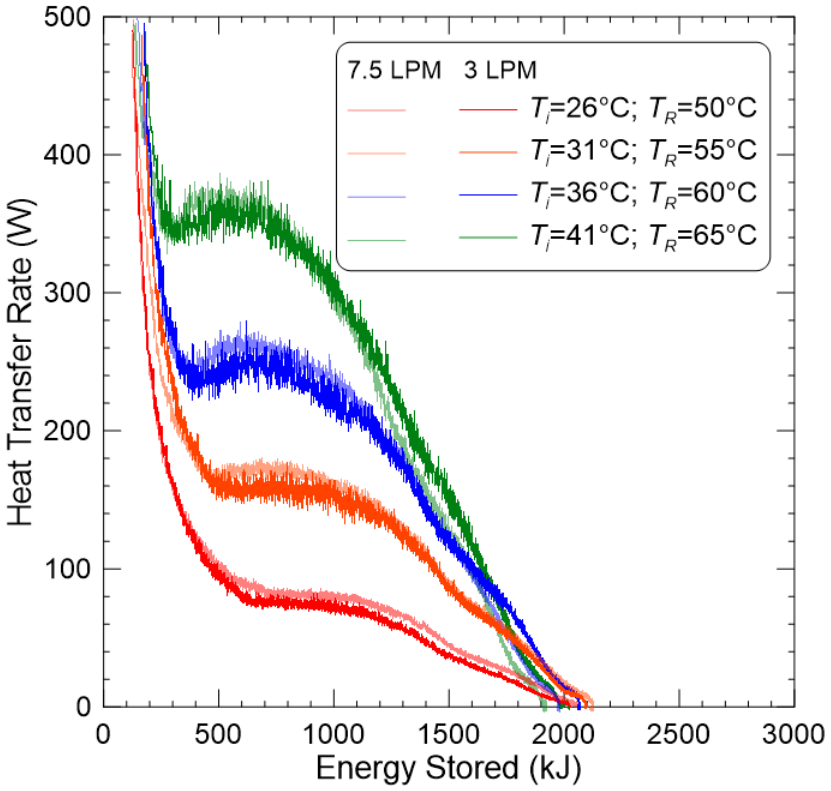

Figure 4.8: Equivalent energy discharging results varying flow rate

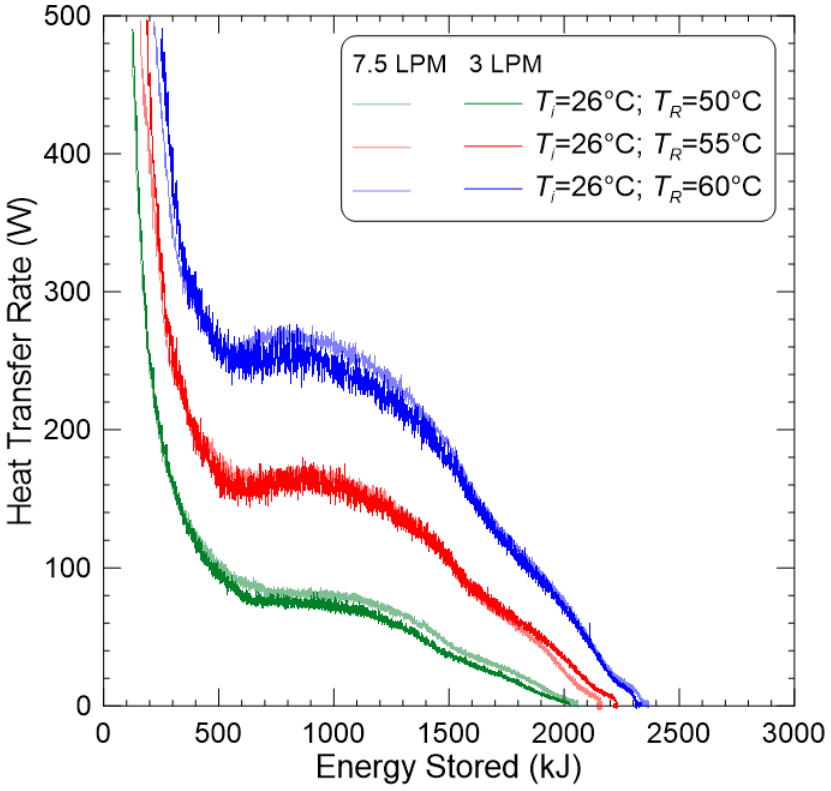

Figure 4.9: T_i identical T_R different charging results varying flow rate

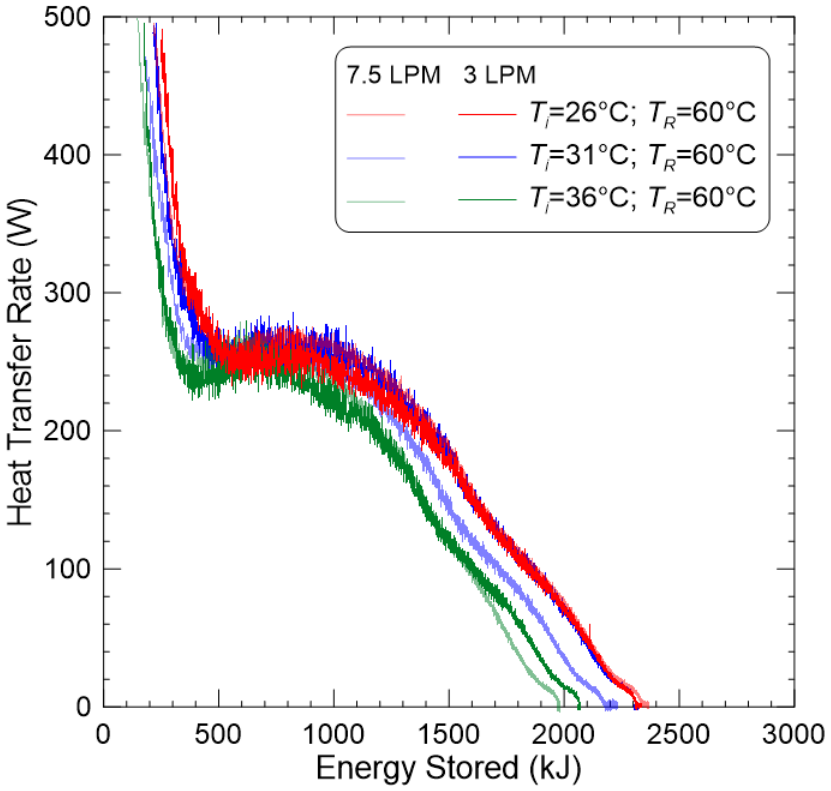

Figure 4.10: T_R identical T_i different charging results varying flow rate

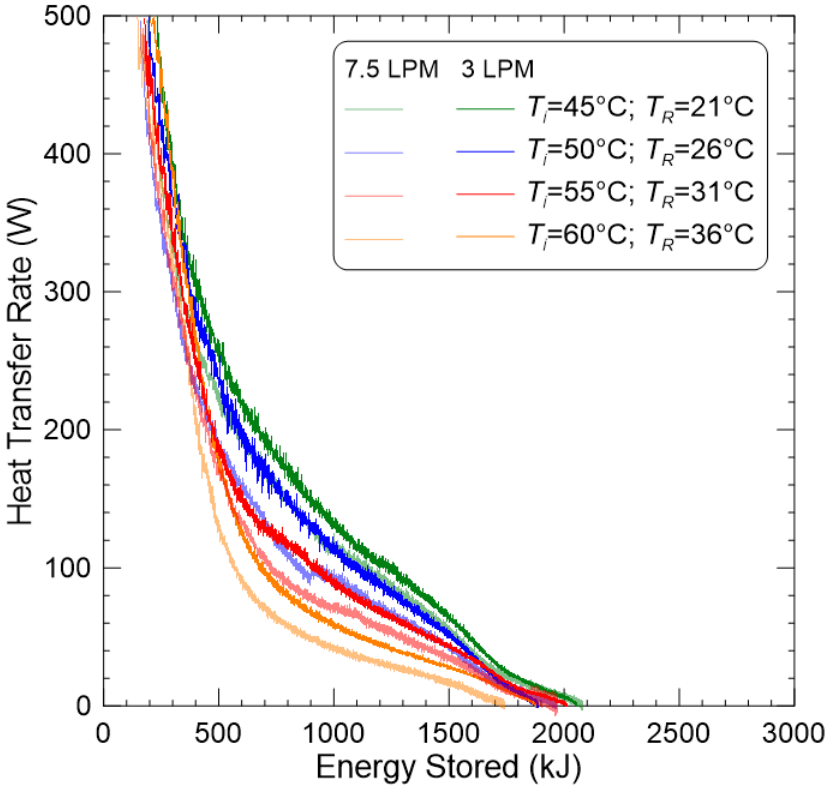

Figure 4.11: Equivalent energy discharging results varying flow rate

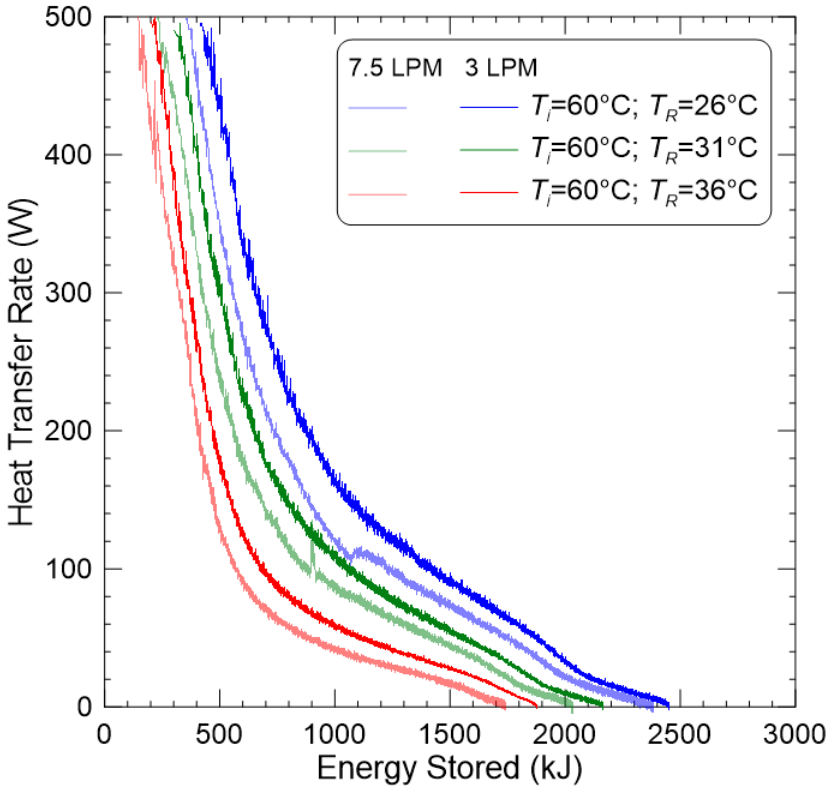

Figure 4.12: T_i identical T_R different discharging results varying flow rate

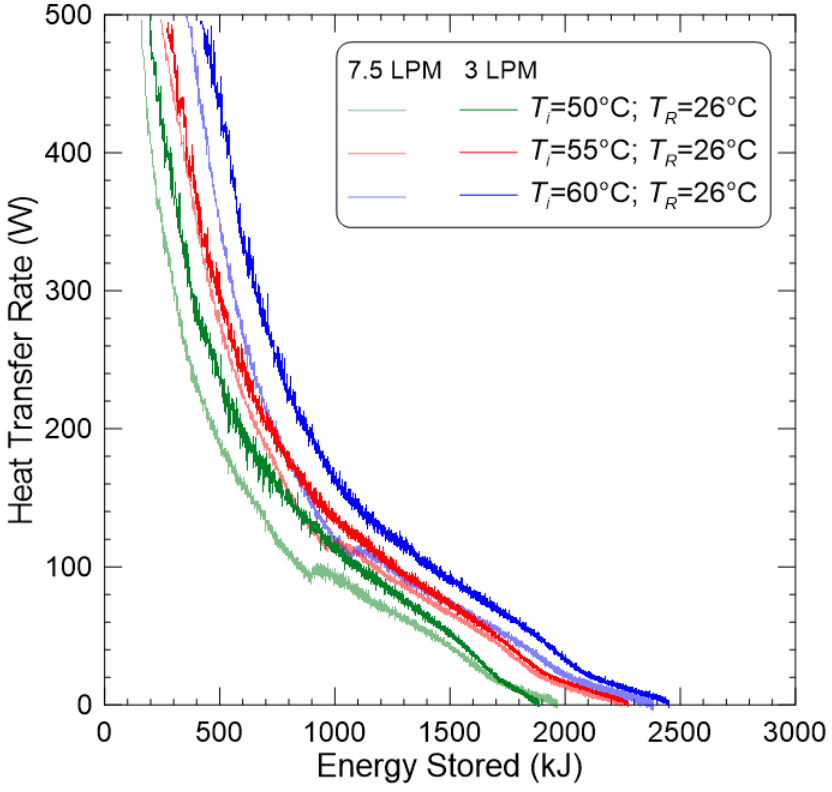

Figure 4.13: T_R identical T_i different discharging results varying flow rate

The charging experiments show insignificant differences between the high flow rate and the low flow rate trials with heat transfer rates for the high flow rate experiments being slightly larger than those of the low flow rate experiments. However, this difference is much too minuscule to be considered significant evidence of increased heat transfer due to increased flow rate.

The discharging experiments also demonstrate no major difference in the heat transfer between the high flow rate to the low flow rate, however the heat transfer of the high flow rate trials appears to be slightly lower than those of the low flow rate. The increase in flow rate correlates with an increase in convection heat transfer in the heat exchanger tubing as well as the exterior tubing. This may have led to the slight increase in heat transfer seen in the charging experiments. However, the discharging experiments show a very slight decrease in heat transfer, contradictory to this prediction. This may have been caused by the addition of the booster pump which may have added some heat to the inlet side of the HTF entering the heat exchanger. This would cause the discharging experiments to appear to experience a reduced heat transfer due to this increased inlet temperature, while the charging experiments would appear to experience a larger heat transfer. This variation in heat transfer, however, is very small and therefore it is reasonable to say that there were not enough discernable differences between the heat transfer in both sets of experiments to derive a conclusive result.

4.5 Theoretical Energy Storage Capacity

The theoretical energy and its uncertainty were calculated based on the methodology presented in Section 3.6.3. This energy value was compared to the measured stored or discharged total energy for each trial recorded. The percent difference was determined between the theoretical and the experimental values of energy and displayed in Table 4.1. The percent difference observed is well within the calculated relative uncertainty for each trial as the largest percent difference observed is 12.5%. This demonstrates that the experimental results are accurate to what is expected relative to the theory.

Table 4.1: Theoretical vs experimental energy stored for dodecanoic acid

Type of Experiment	T_i	T_R	Theoretical Energy, kJ	Measured Energy, kJ	Absolute Uncertainty, kJ (Relative Uncertainty)	Percent Difference
Discharging	55	26	2214	2211	± 496 (22%)	-0.1%
Charging	26	55	2214	2168	± 362 (17%)	-2.1%
Discharging	60	26	2322	2453	± 557 (23%)	5.7%
Charging	26	60	2322	2335	± 506 (22%)	0.6%
Discharging	50	26	2106	1888	± 387 (21%)	-10.3%
Charging	26	50	2106	2026	± 351 (17%)	-3.8%
Discharging	60	31	2234	2163	± 495 (23%)	-3.2%
Charging	31	60	2234	2303	± 487 (21%)	3.1%
Discharging	55	31	2126	2010	± 462 (23%)	-5.4%
Charging	31	55	2126	2102	± 347 (17%)	-1.1%
Discharging	60	36	2146	1878	± 456 (24%)	-12.5%
Charging	36	60	2146	2059	± 471 (23%)	-4.0%
Discharging	45	21	2085	2056	± 453 (22%)	-1.4%
Charging	41	65	2166	2021	± 480 (24%)	-6.7%

4.6 Conclusion

This chapter discusses the results of dodecanoic acid as a phase change material in the LHTES system used in this study. The effect of the operating conditions such as HTF temperature T_R and initial temperature T_i are discussed as well as the effects of increasing the HTF flow rate. It was found that T_R significantly affects the heat transfer of the system while T_i plays a lesser role, especially for charging experiments. The effect of increasing HTF temperature was found to be negligible with discrepancies possibly being associated with systematic error. The measured energy stored was compared to theoretical values and determined to be accurate in respect to its uncertainty. The following chapter will discuss the use of 1-octadecanol in the same LHTES system in a similar fashion. The effects of HTF flow rate will be omitted from this analysis as it was proven to have little effect on the system.

Chapter 5: 1-Octadecanol Results

This chapter presents the results of the experimental trials using 1-octadecanol as the PCM. Similarly to Chapter 4, figures displaying measured temperature, calculated power and energy for both charging and discharging experiments will be presented and discussed in this chapter, with the only altered variable being the PCM used in the LHTES.

5.1 Temperature Results

Figure 5.1 a) and b) display typical trends for the temperature of the LHTES system using 1-octadecanol for charging and discharging experiments respectively. Once again, measurements of the ambient temperature, inlet and outlet temperatures of the HTF as well as the top, middle and bottom temperatures of the PCM were recorded with the various temperature sensors used in the study. The experiments used for the temperature results represented were T_i= 40°C to T_R= 69°C and T_i= 69°C to T_R= 40°C for charging and discharging respectively.

Charging results are presented in Figure 5.1 a). In this figure, the hot HTF can be seen entering the heat exchanger with an inlet temperature of 69°C. The outlet temperature begins at a temperature of approximately 68°C before increasing asymptotically towards the inlet temperature. The PCM temperature in all three thermocouple positions rises rapidly immediately after the HTF enters the heat exchanger, similar to the dodecanoic acid trials. This rapid increase is followed by an infection point that begins at approximately 55°C. This coincides with the solid-solid phase transformation detailed in Section 3.1.2. It is observed in this figure that for 1-octadecanol, a second inflection point occur in the melting process at approximately 58°C, coinciding with the second phase transformation associated with melting in 1-octadecanol. As observed for the dodecanoic acid results in Section 4.1, the effects of natural convection cause the middle and bottom thermocouples to display a much more drawn out phase change process while the top thermocouple displays a more rapid temperature change. For this charging experiment none of the three thermocouples embedded in the PCM reach the HTF setpoint temperature and instead reach steady state at approximately 68°C.

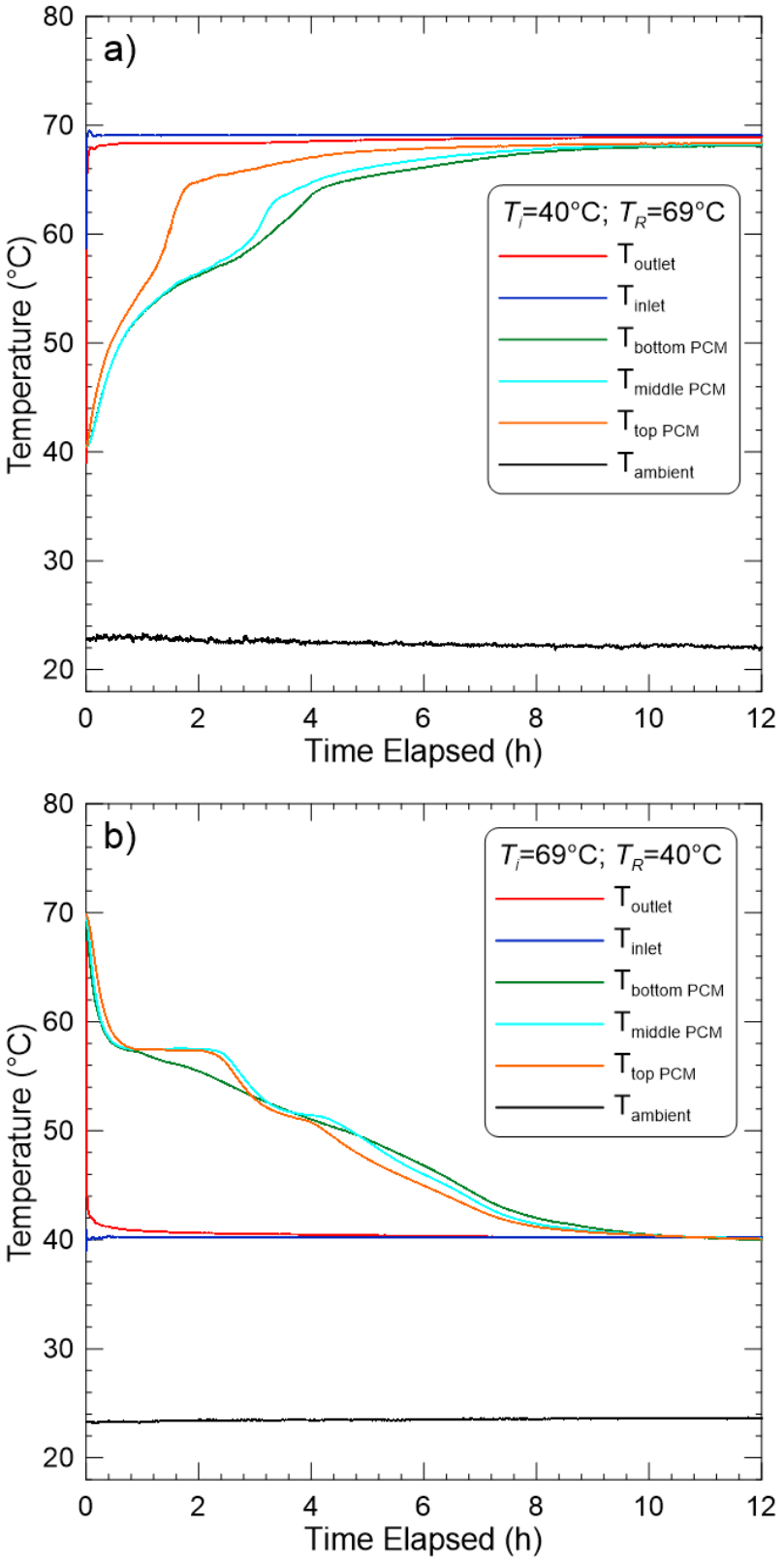

Figure 5.1: Typical trend of various temperature sensors for 1-octadecanol a) charging experiment b) discharging experiment

This could be due to the increased losses exhibited at the higher temperature of the 1-octadecanol trials (demonstrated in Section 3.6.2) in contrast to the charging trials of dodecanoic acid. Ambient temperature appears to be constant at 23°C throughout the experiment.

The discharging results presented in Figure 5.1 b) shows the temperature of the cold HTF at the inlet at 40°C as it enters the heat exchanger. The outlet temperature begins slightly higher than the HTF inlet temperature value at approximately 42°C, however this value begins to decrease asymptotically as it reaches values only slightly higher than that of the inlet. The PCM temperature observed in each thermocouple position decreases rapidly at the commencement of the trial, only to reach an initial plateau at approximately 58°C. This coincides with the solidification temperature of 1-octadecanol. Another, smaller plateau is observed at approximately 50°C when the PCM undergoes a solid-solid phase transition. This figure demonstrates clearly the two phase transformations observed for this material in contrast to only the single phase transformation observed for dodecanoic acid. The perception of the isothermal phase transitions is clearer in the middle and top thermocouples compared to the bottom indicator, this may have been due to experimental error in the movement or rotating of the thermocouple holder, moving it closer to the heat exchanger coil. This would cause the PCM near the bottom thermocouple to change phase faster than the top and middle indicators. All three thermocouple probe values eventually reach steady state at a temperature equivalent with the HTF temperature. Ambient temperature appears to be constant at approximately 23°C for the duration of the trial.

5.2 Charging Results

Results of instantaneous heat transfer rates for charging experiments are plotted against the cumulative energy stored in the LHTES for experiments similarly to Section 4.2, with 1-octadecanol as the PCM. Figures 5.2, 5.3 and 5.4 presents the results for charging experiments and display the common trends of all charging experiment. These experiments exhibit similar trends to the results of dodecanoic acid experiments demonstrating an instantaneous increase in heat transfer followed by a rapid decrease until a plateau is reached which corresponds with the phase transition(s) of the PCM. The heat transfer then

begins to decrease more gradually until the system reaches a state of full charge, at which time the heat transfer value goes to zero.

Figure 5.2, demonstrates the results of charging experiments of 1-octadecanol for experiments of identical stored energy, but varying T_i and T_R. All of the trials appear to reach the same energy values with the exception of the T_i=40°C to T_R =64°C trial. This trial may not have fully reached steady state within the designated trial time due to the small difference between the HTF temperature to the PCM melting temperature. This effect may have been more significant in the 1-octadecanol trials compared to the dodecanoic acid trials due to the increased latent heat values and therefore a longer charging time. The experiments with higher T_R values in this figure display larger values of heat transfer throughout the duration of the trials, consistent with the results from Section 4.2.

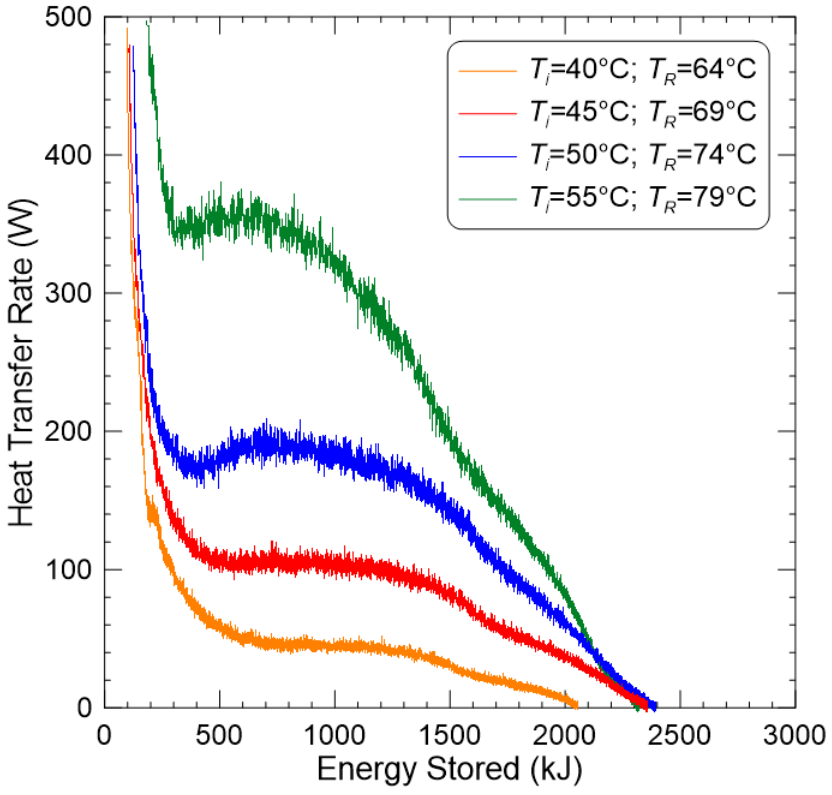

Figure 5.2: Equivalent energy charging results 1-octadecanol

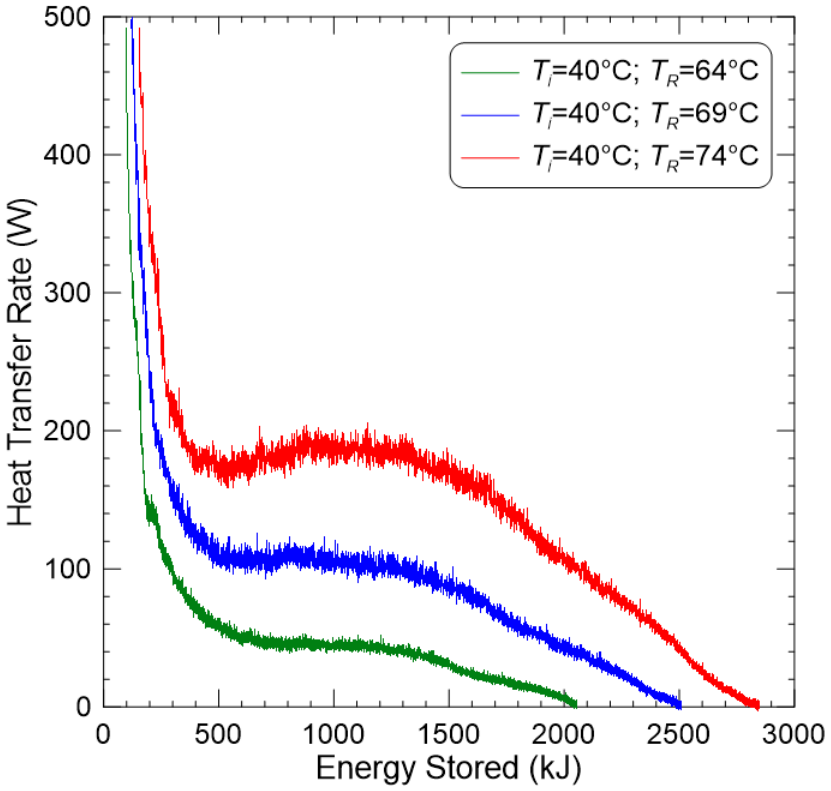

Figure 5.3: T_i identical T_R different charging results for 1-octadecanol

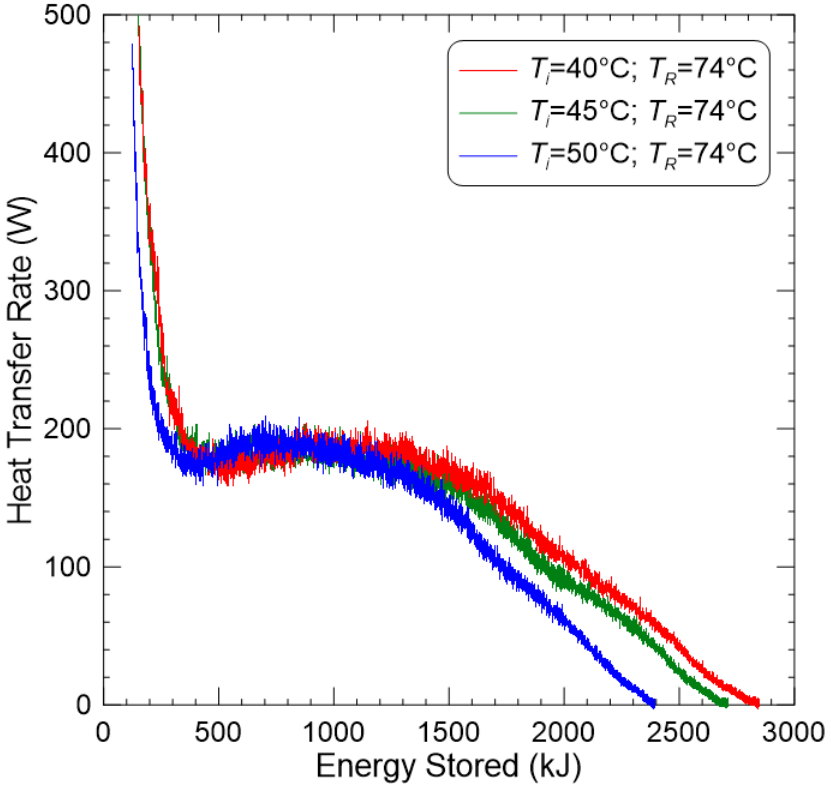

Figure 5.4: T_R identical T_i different charging results for dodecanoic acid

This again signifies that difference between the HTF temperature and the PCM melting temperature (T_R - T_m) is much more significant in driving the heat transfer process than is the total ΔT in charging for experiments with 1-octadecanol as the PCM.

5.3 Discharging Results

The results of discharging are shown in Figures 5.5, 5.6 and 5.7. The typical trend of discharging experiments for the 1-octadecanol experiments involves a continuous decrease in heat transfer as the trial progresses due to the effects described in Section 4.3. The heat transfer eventually reaches zero when the system is fully discharged.

Figure 5.5 represents discharging experiments of equivalent energy and demonstrates the effect of decreasing the T_R in discharging experiments. The general trend appears to be the same as observed using dodecanoic acid as the PCM, further emphasizing that the heat transfer of these trials, despite having the same ΔT, is strongly dependent on the T_R value, however the results are less conclusive. The results of the T_i=64°C to T_R=40 trial appear to have the smallest heat transfer initially and never surpass the heat transfer of the T_i=69°C to T_R=45 trial, despite having a smaller T_R value. This could demonstrate that one of these experiments may be an outlier as the other trials appear to have heat transfer values with magnitude inversely proportional to their T_R values as observed in the dodecanoic acid experiments. However, it is justified to note that the effect of T_R is much less significant than observed in the charging trials for 1-ocatdecanol.

Figure 5.6 demonstrates a clear trend for trials of equivalent T_i but different T_R. Showing the increase in heat transfer throughout the trial with decreasing T_R and increasing ΔT. Figure 5.7 displays experiments of equivalent T_R with decreasing T_i, this figure shows that the initial PCM temperature may play a larger role in the effect of the heat transfer in discharging compared with charging experiments. This reiterates what was observed for the dodecanoic acid experiments in Figure 4.7 and can be explained by the larger role played by ΔT in the heat transfer process for discharging due conduction being the only mode of heat transfer.

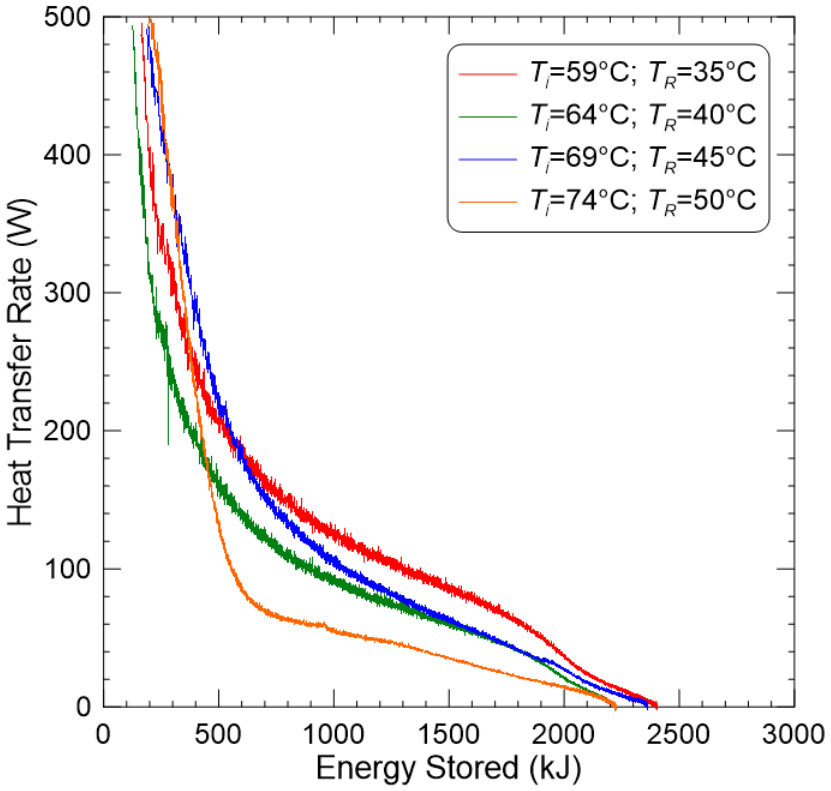

Figure 5.5: Equivalent energy discharging results for 1-octadecanol

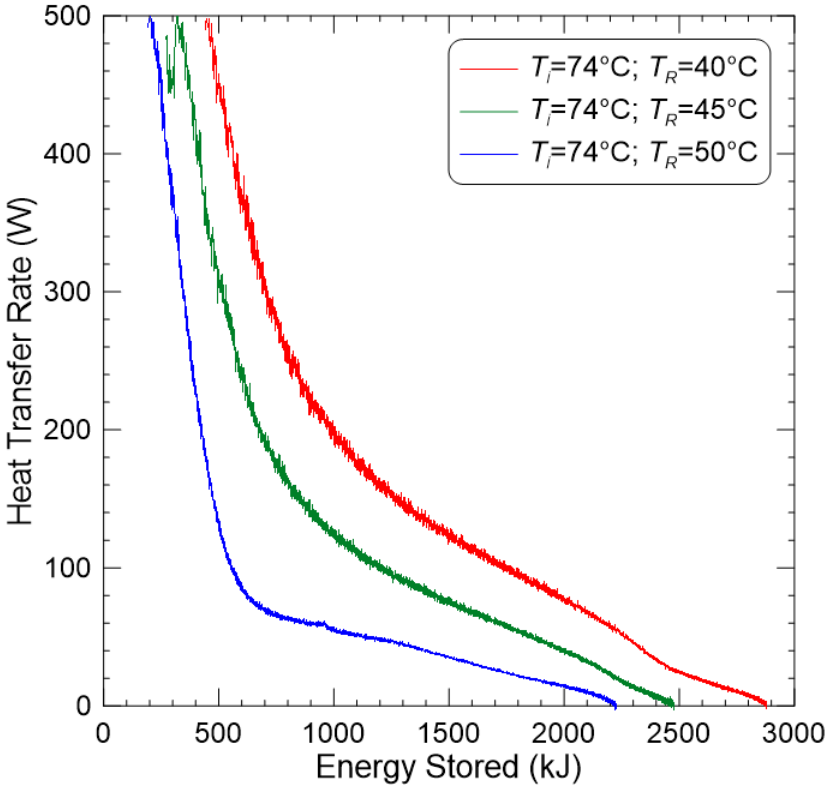

Figure 5.6: T_i identical T_R different discharging results for 1-octadecanol

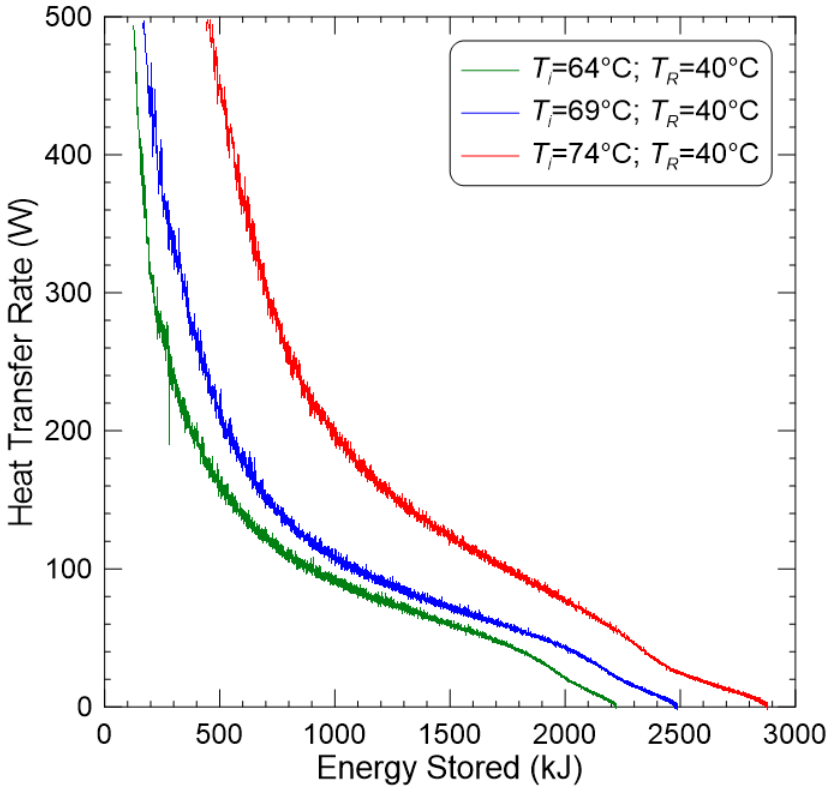

Figure 5.7: T_R identical T_i different discharging results for 1-octadecanol

5.4 Theoretical Energy Storage Capacity

Table 5.1 displays the theoretical and measured energy values for each experimental trial highlighting their disparity in the form of a percent difference. Uncertainty values are presented in the form of relative and absolute uncertainties for the measured energy. The percent difference observed is within the calculated relative uncertainty for each trial as the largest percent difference observed is 15.8% with the uncertainty of this data being 18%. This demonstrates that the experimental results are accurate to what is expected relative to the theory.

5.5 Conclusion

This chapter discusses the results of 1-ocatdecanol as a phase change material in the LHTES system used in this study. The effect of the operating conditions such as HTF temperature T_R and initial temperature T_i are discussed. It was found that T_R significantly affects the heat transfer of the system while T_i plays a lesser role for charging experiments.

Table 5.1 Theoretical vs experimental energy stored for 1-ocatdecanol

Type of Experiment	T_i	T_R	Theoretical Energy, kJ	Measured Energy, kJ	Total Uncertainty, kJ (Relative Uncertainty)	Percent Difference
Discharging	69	40	2499	2487	± 558 (22%)	-0.4%
Charging	40	69	2499	2846	± 577 (20%)	13.9%
Discharging	74	40	2611	2221	± 624 (28%)	-14.9%
Charging	40	74	2611	2508	± 636 (25%)	-4.0%
Discharging	64	40	2387	2405	± 496 (21%)	0.8%
Charging	40	64	2387	2057	± 500 (24%)	-13.8%
Discharging	74	45	2532	2712	± 402 (15%)	7.1%
Charging	45	74	2532	2339	± 606 (26%)	-7.6%
Discharging	69	45	2420	2355	± 521 (22%)	-2.7%
Charging	45	69	2420	2224	± 524 (24%)	-8.1%
Discharging	74	50	2453	2395	± 520 (22%)	-2.4%
Charging	50	74	2453	2313	± 564.7 (24%)	-5.7%
Discharging	59	35	2353	2363	± 546.1 (23%)	0.4%
Charging	55	79	2487	2879	± 506.2 (18%)	15.8%

However, for discharging experiments T_i appears to have a larger impact on the system as due to the dominance of conduction, the effect of ΔT is more pronounced. The measured energy stored was compared to theoretical values and determined to be accurate in respect to its uncertainty. These results reiterate and further cement the conclusions observed Chapter 4, demonstrating that, varying operating parameters cause similar trends for both dodecanoic acid and 1-octadecanol. The next chapter will directly compare the two PCMs studied by comparing results obtained with both PCMs under identical operating conditions. Attempts to quantify the impact of various PCM properties on the system parameters will be made using performance indicators.

Chapter 6: PCM Comparison and Data Reduction

This chapter discusses the experimental results from the LHTES system using dodecanoic acid and 1-octadecanol. Various comparisons between the two PCMs are made through the use of performance indicators described in Chapter 2 in an attempt to further reduce the data so that the effect the PCM's thermophysical properties on the system may be isolated and understood quantitatively.

6.1 Charging Results

Graphical representations of charging experiments are displayed in this Section, similarly to Sections 4.2 and 5.2. The heat transfer rate plotted against both time and energy shows results of both dodecanoic acid and 1-octadecanol on the same set of axes, which are presented in Figures 6.1 to 6.7. Each graph presents experiments of equivalent initial and final temperatures in relation to the individual PCM's melting point.

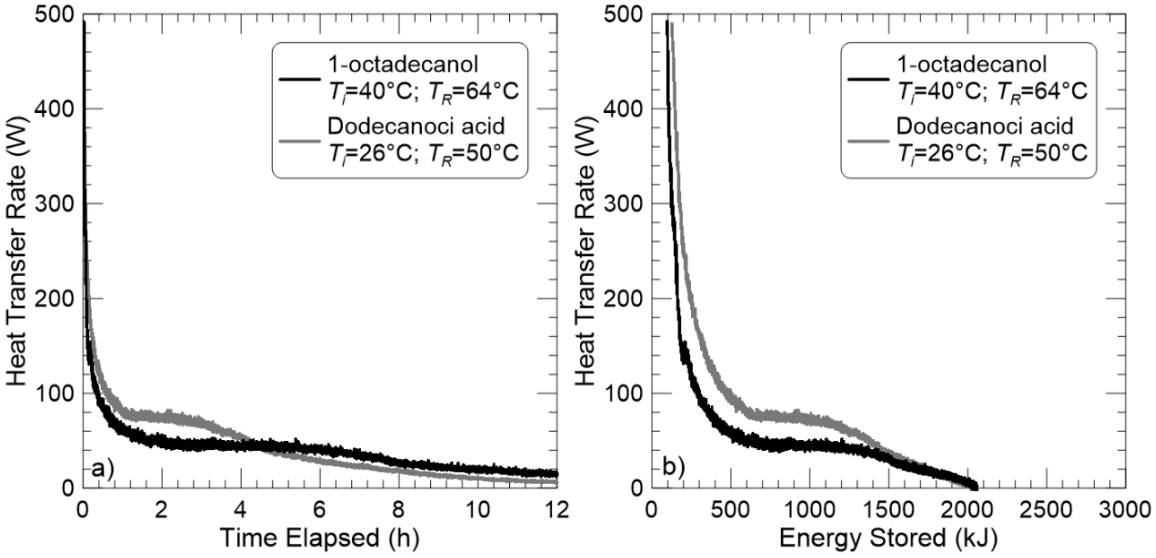

Figure 6.1: Heat transfer rate during charging with dodecanoic acid and 1-octadecanol T_m-17°C; T_m+7°C a) vs time b) vs energy

A trend is present for the charging experiments as the heat transfer rate for dodecanoic acid is initially greater than that of 1-octadecanol. However, as the trial continued, the 1-octadecanol results showed superior heat transfer rates close to the end of the experiment.

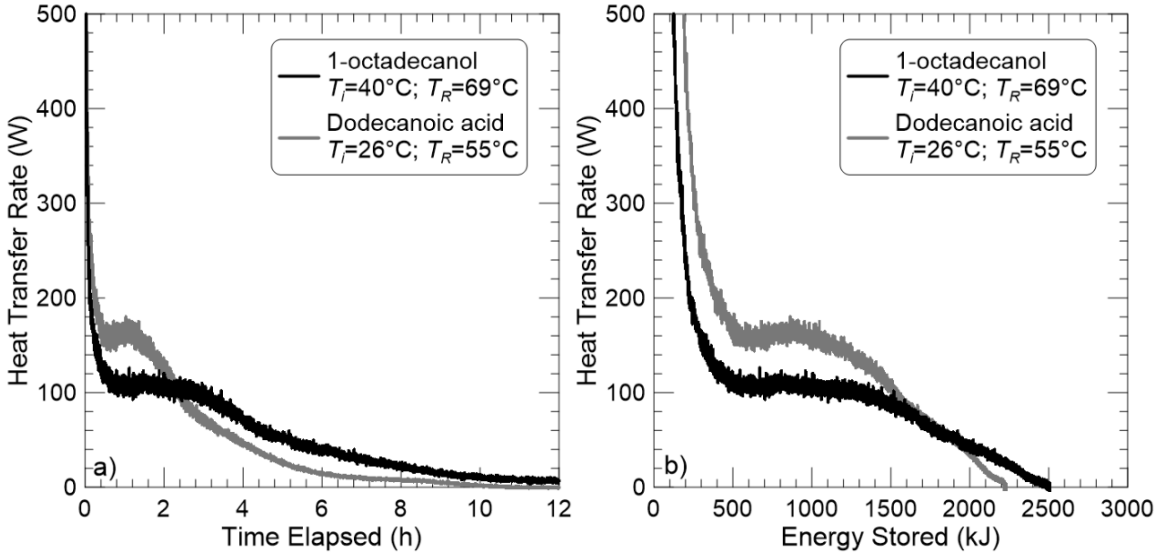

Figure 6.2: Heat transfer rate during charging with dodecanoic acid and 1-octadecanol T_m-17°C; T_m+12°C a) vs time b) vs energy

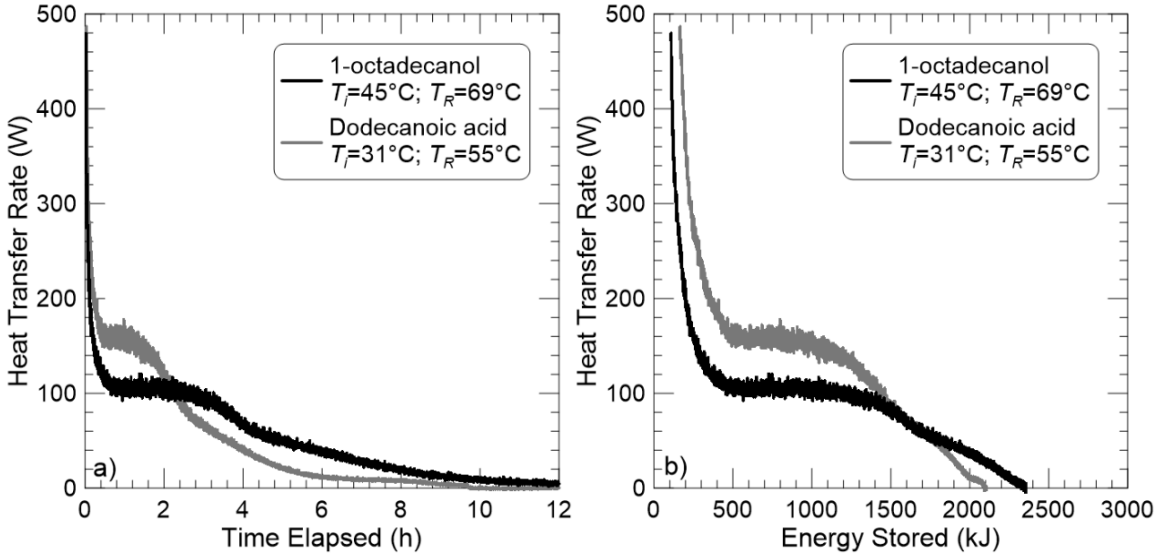

Figure 6.3: Heat transfer rate during charging with dodecanoic acid and 1-octadecanol T_m-12°C; T_m+12°C a) vs time b) vs energy

LHTES systems using 1-octadecanol feature larger energy storage values for the duration of the experiments in nearly all of the results except for the ones presented in Figure 6.1. The larger energy storage observed in the 1-octadecanol results from the larger latent heat value for this PCM compared to dodecanoic acid.

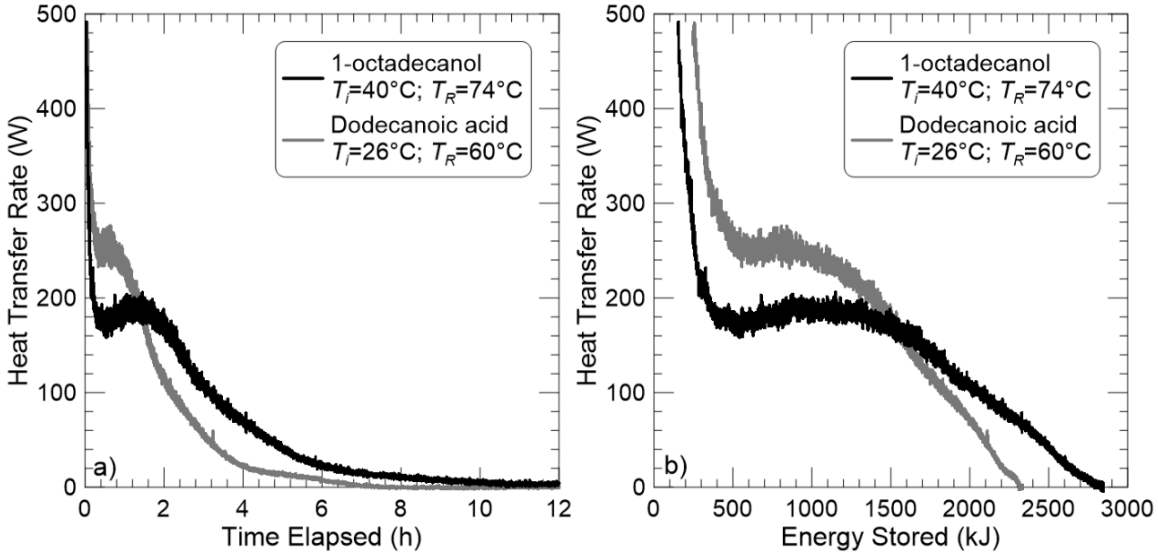

Figure 6.4: Heat transfer rate during charging with dodecanoic acid and 1-octadecanol T_m-12°C; T_m+12°C a) vs time b) vs energy

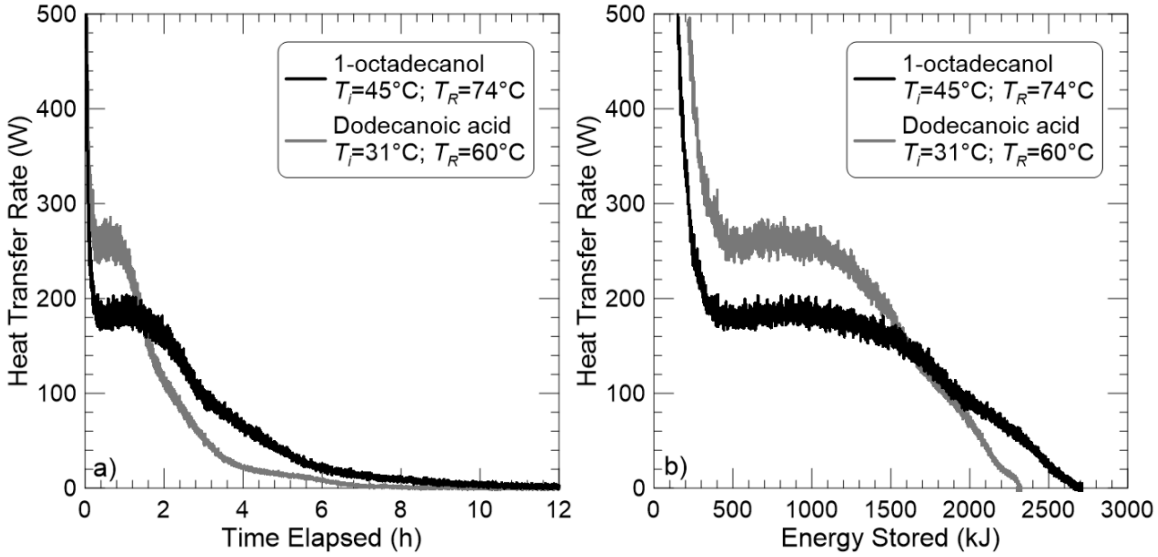

Figure 6.5: Heat transfer rate during charging with dodecanoic acid and 1-octadecanol T_m-7°C; T_m+12°C a) vs time b) vs energy

The larger thermal conductivity of 1-octadecanol compared to dodecanoic acid would suggest that this PCM would lead to a larger heat transfer rate with a higher peak power value, however the opposite is true in this case. This suggests that the observed increase in thermal conductivity, by approximately 1.5-2 times (depending on the PCM state) is not significant in the makeup of the heat transfer profile.

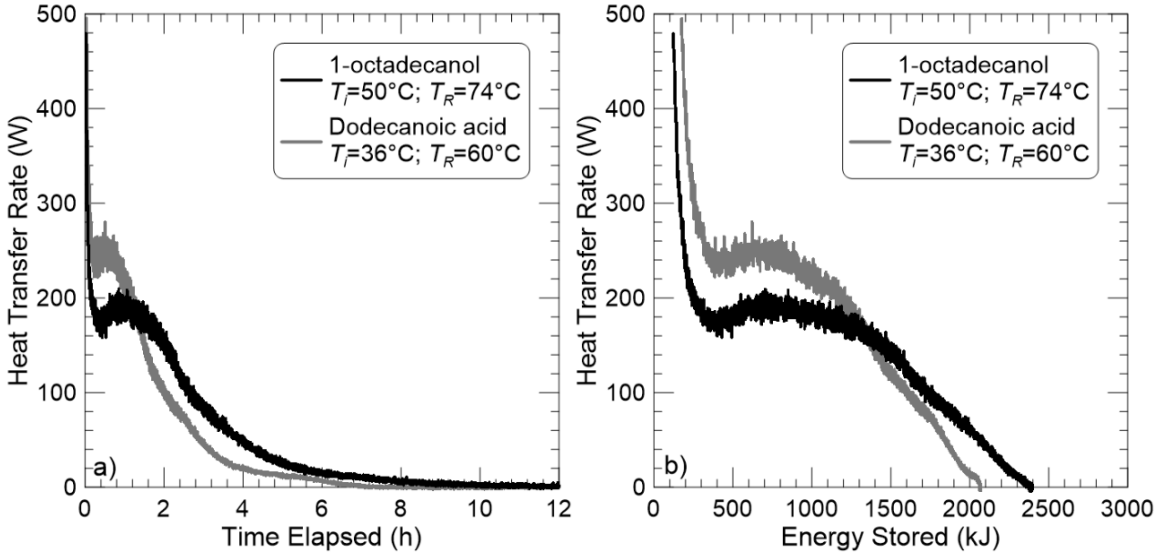

Figure 6.6: Heat transfer rate during charging with dodecanoic acid and 1-octadecanol T_m-7°C; T_m+12°C a) vs time b) vs energy

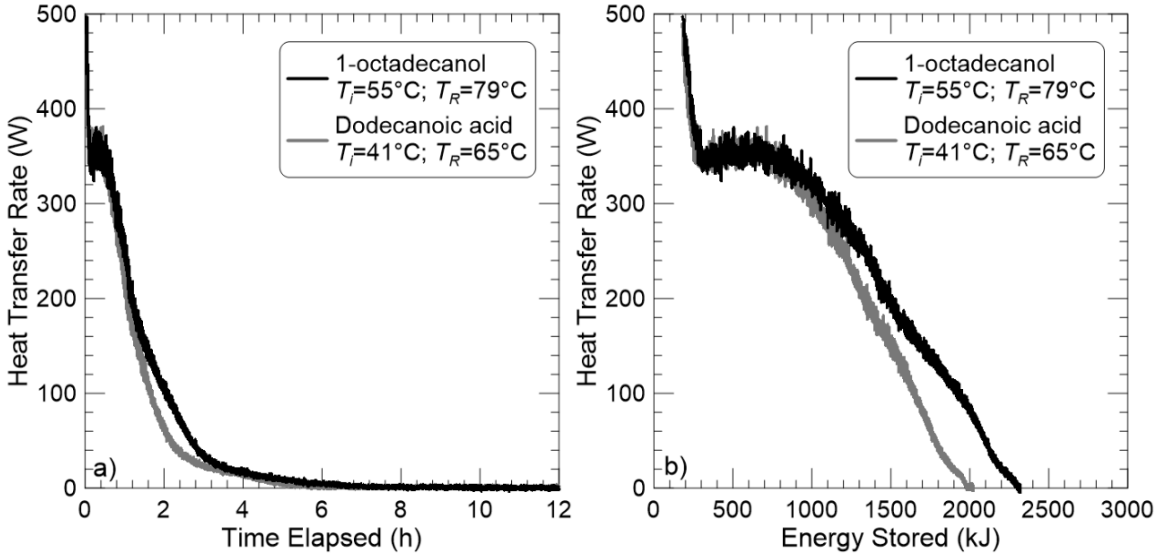

Figure 6.7: Heat transfer rate during charging with dodecanoic acid and 1-octadecanol T_m-2°C; T_m+22°C a) vs time b) vs energy

This means that the thermophysical properties of the phase change material may not play as large a role in the effect of the heat transfer in the experiment as other factors such as the nature the phase change and the effects of natural convection.

The difference in heat transfer rates observed between the charging experiments using both

PCMs could be a result of differences in the natural convection process observed between the two PCMs. The viscosity of the PCM plays a role in the natural convection process, 1-octadecanol has a larger viscosity close to its melting temperature compared to dodecanoic acid. This could result in a weakening of the natural convection process during melting, resulting in a lower heat transfer rate. The relationship between the two PCMs viscosities with respect to the melting temperature differential is shown in Figure 6.8. This shows that although 1-ocatdecanol has a greater viscosity for temperatures closer to the PCMs' respective melting points, the viscosity of the two PCMs appears to be equal at approximately 21°C above their melting points. This confirms results observed in Figure 6.7, in which trials of a melting differential of 22°C demonstrate equivalent heat transfer. This is contrary to what is seen in the other trials when the melting differential is less than 22°C. The solid-solid phase change which occurs at 55°C, (from the DSC diagram in Figure 3.1), may also lead to a delayed effect of natural convection since more energy will be needed to bring 1-octadecanol to its solid-liquid melting point.

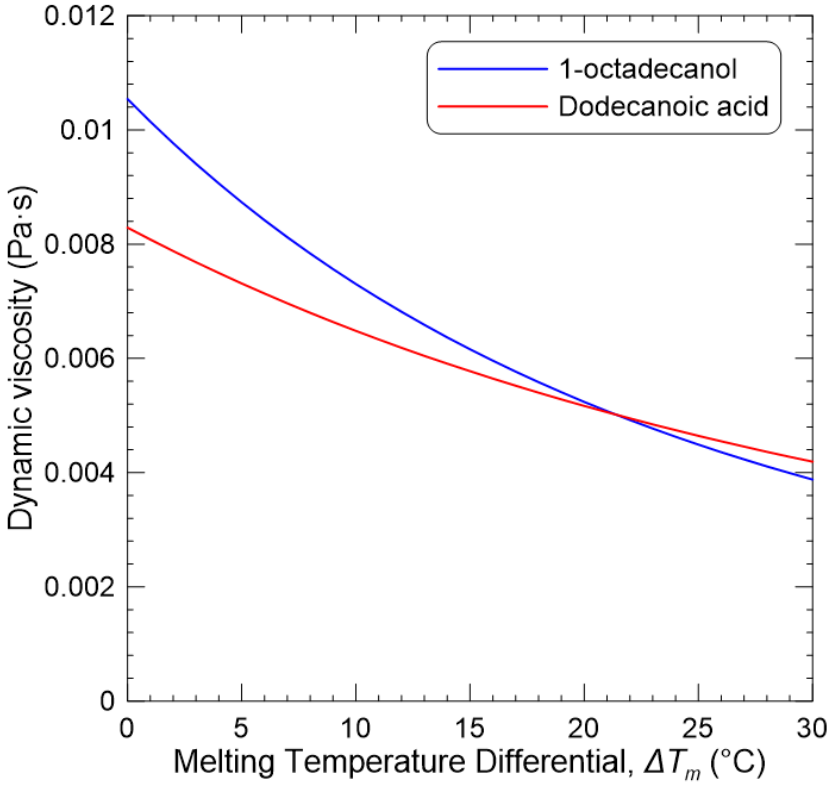

Figure 6.8: Dynamic viscosity of 1-octadecanol and dodecanoic acid vs melting temperature differential (Yaws, 2003)

6.2 Discharging Results

Discharging experiments using 1-ocatdecanol and dodecanoic acid are presented in Figure 6.9 to 6.15 in the form of heat transfer rates versus time as well as versus energy. Again, each graph demonstrates experiments of equivalent initial and final temperatures in relation to the individual PCM's melting point.

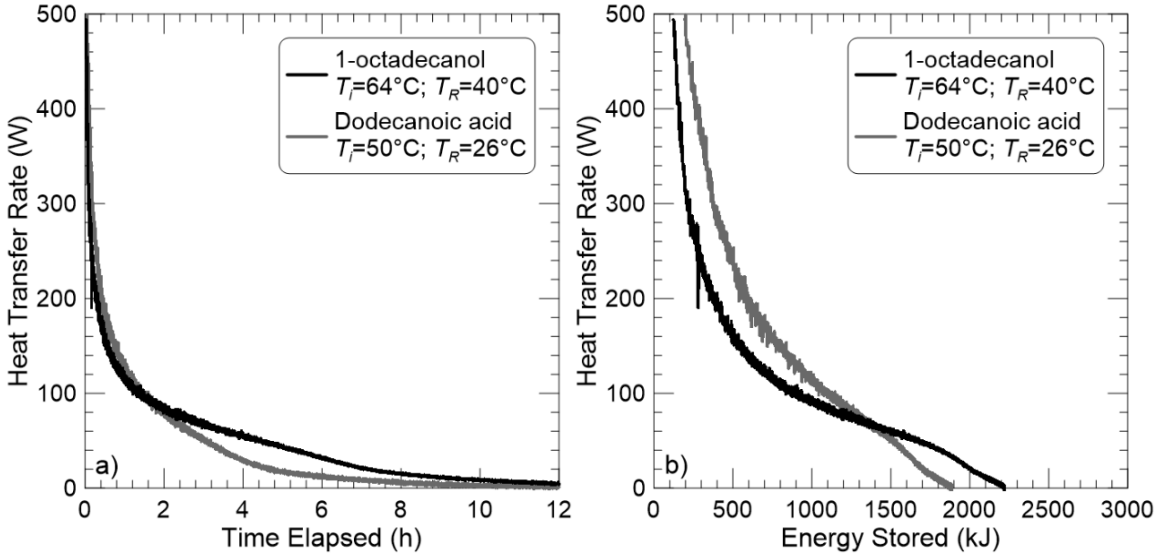

Figure 6.9: Heat transfer rate during discharging with dodecanoic acid and 1-octadecanol T_m+7°C; T_m-17°C a) vs time b) vs energy

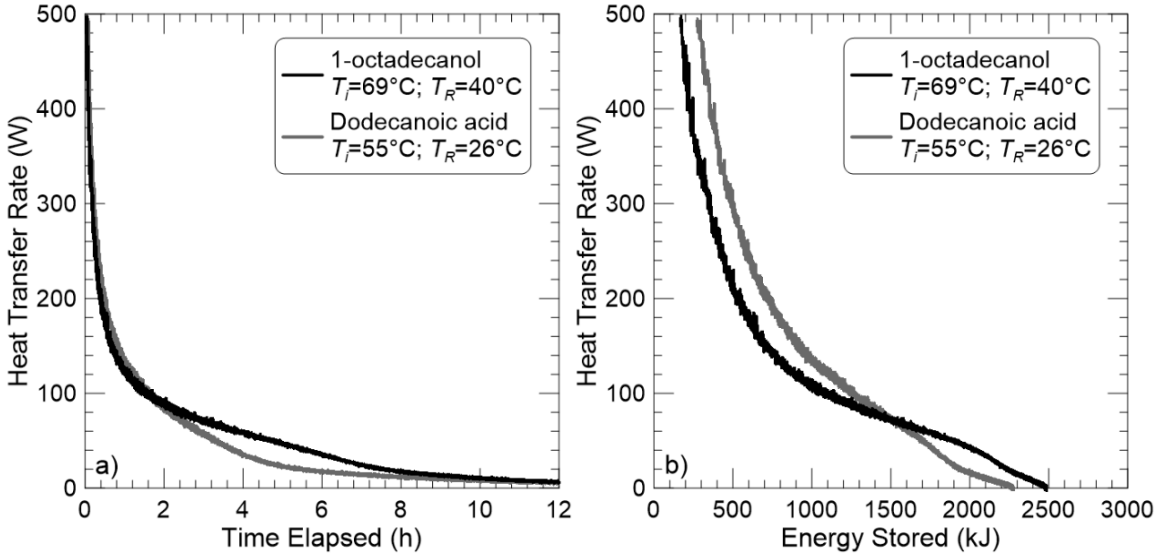

Figure 6.10: Heat transfer rate during discharging with dodecanoic acid and 1-octadecanol T_m+12°C; T_m-17°C a) vs time b) vs energy

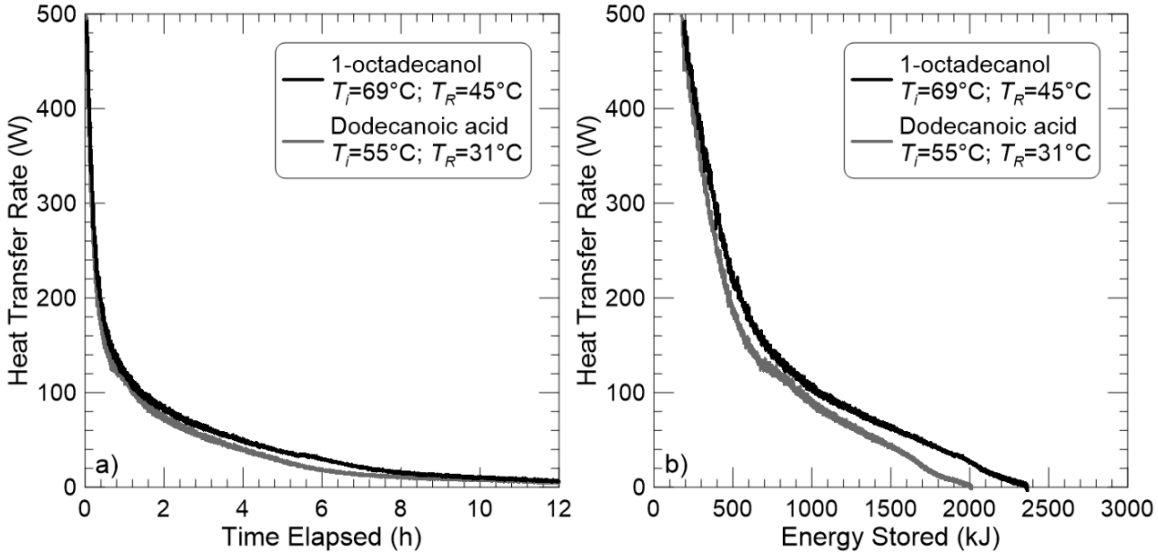

Figure 6.11: Heat transfer rate during discharging with dodecanoic acid and 1-octadecanol T_m+12°C; T_m-12°C a) vs time b) vs energy

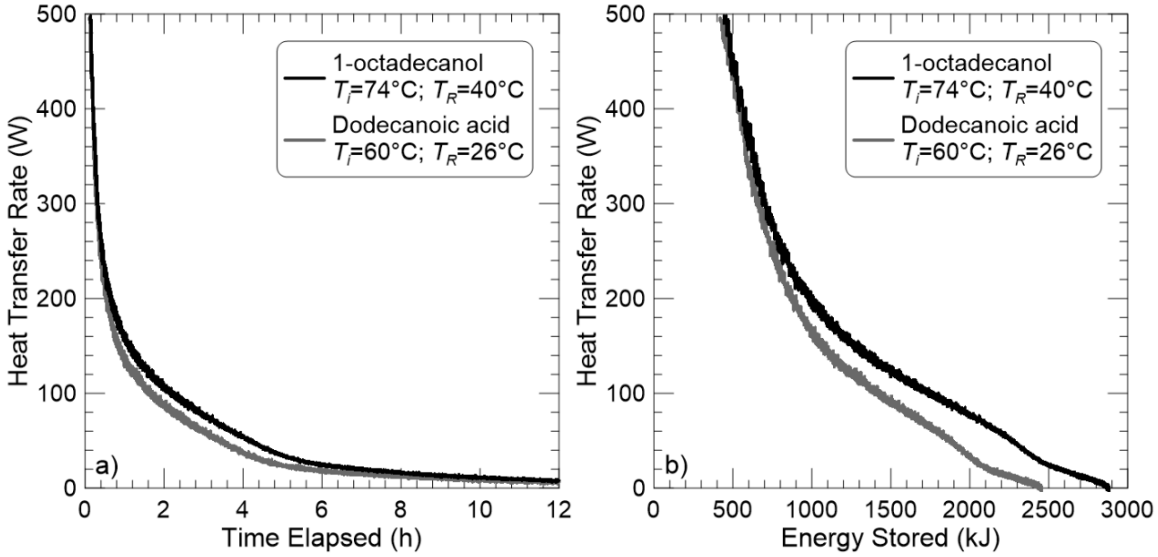

Figure 6.12: Heat transfer rate during discharging with dodecanoic acid and 1-octadecanol T_m+17°C; T_m-12°C a) vs time b) vs energy

Similar to the results of the charging trials, the discharging results using dodecanoic acid demonstrate a heat transfer profile with a larger peak and reaching a final state of charge at a lower energy value than that of 1-ocatdecanol. This leads to the notion that the same effect may be present in the two different physical phenomena of charging and discharging.

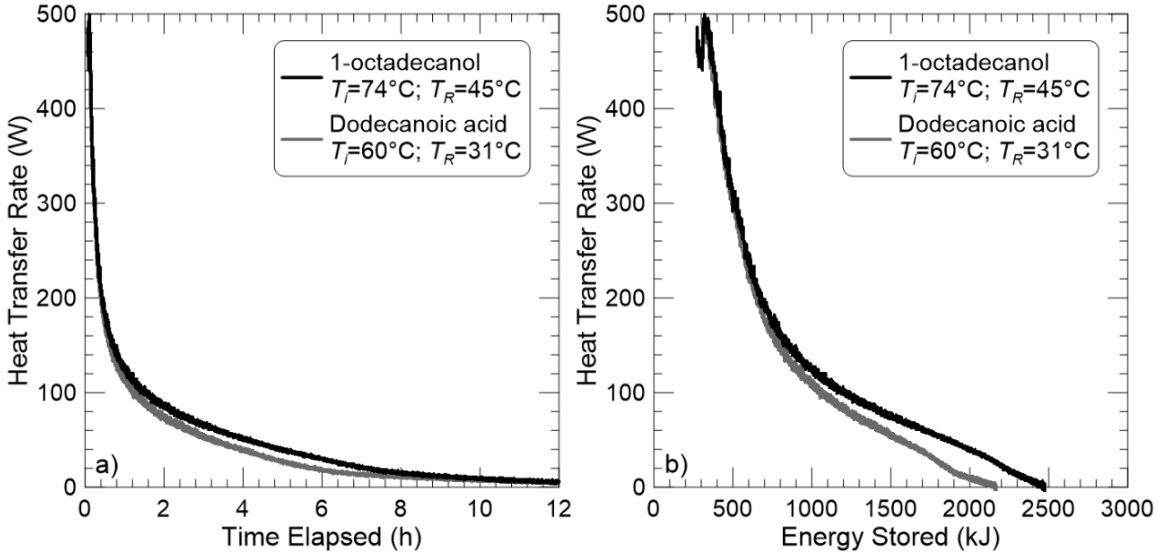

Figure 6.13: Heat transfer rate during discharging with dodecanoic acid and 1-octadecanol T_m+17°C; T_m-12°C a) vs time b) vs energy

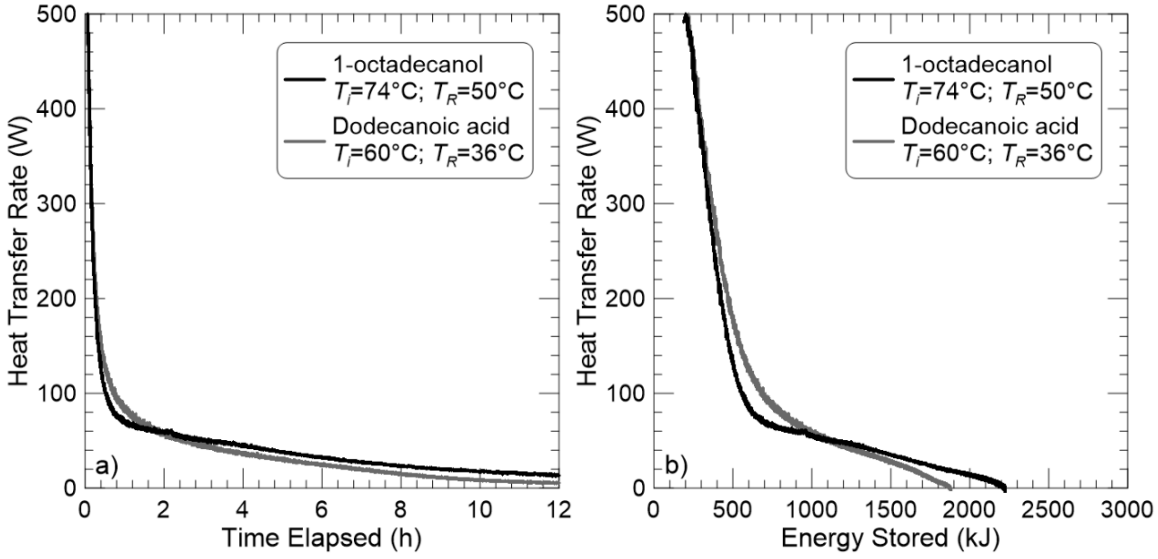

Figure 6.14: Heat transfer rate during discharging with dodecanoic acid and 1-octadecanol T_m+17°C; T_m-7°C a) vs time b) vs energy

The pattern of increased energy storage observed in the discharging results of 1-ocatdecanol are again attributed to larger latent heat values associated with this PCM. One possible explanation for the decreased heat transfer observed in discharging for 1-octadecanol, apart from the aforementioned outliers, is the multiple phase changes that this PCM undergoes.

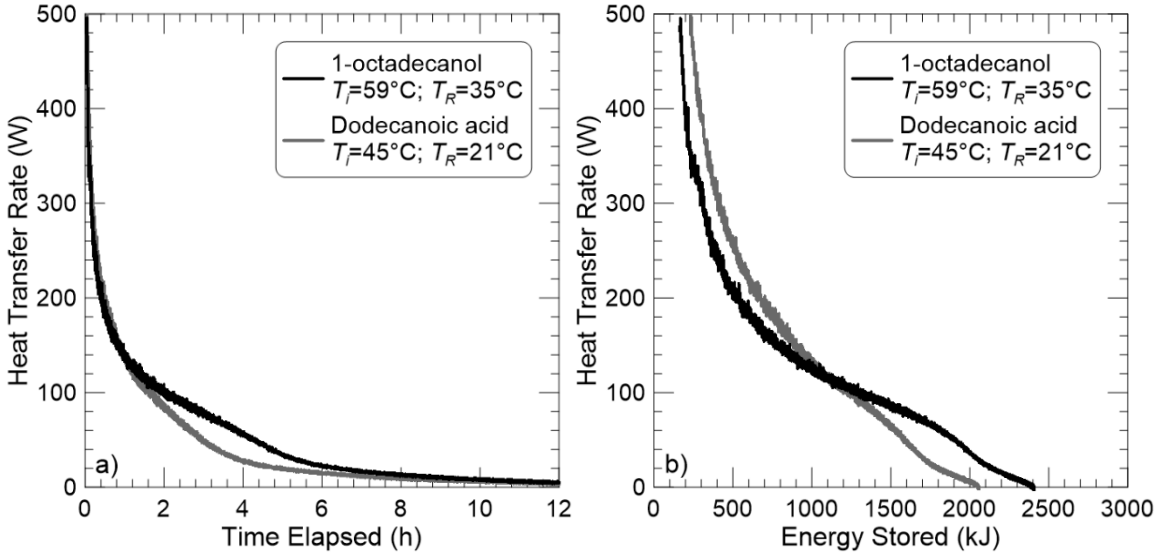

Figure 6.15: Heat transfer rate during discharging with dodecanoic acid and 1-octadecanol T_m+2°C; T_m -22°C a) vs time b) vs energy

After solidification at approximately 58°C, a solid-solid transformation occurs at 50°C, as seen in Figure 3.1. This transformation, like solidification is an isothermal process however, the temperature at which it occurs is lower making it closer to the HTF temperature and thereby decreasing the temperature differential, which drives the heat transfer process. Some of the trials (Figures 6.11, 6.12 and 6.13) show the heat transfer rate of 1-octadecanol being slightly higher than that of dodecanoic acid for the duration of the experiment. These results could be outliers as noted in Section 5.3.

6.3 Energy Profiles

Figures 6.16 and 6.17 present the energy profiles obtained with both PCMs during the charging and discharging processes. Upon analyzing the charging results in Figure 6.16, it is evident that dodecanoic acid exhibits a higher initial increase in energy compared to 1-octadecanol, which displays a more gradual increase throughout the charging period. Additionally, the slope of the dodecanoic acid results sharply decreases into a plateau at the end of the experiment, while 1-octadecanol has a more gradual decrease in slope. This is potentially due to the more significant effects of natural convection during the charging process in dodecanoic acid compared with 1-ocatdecanol.

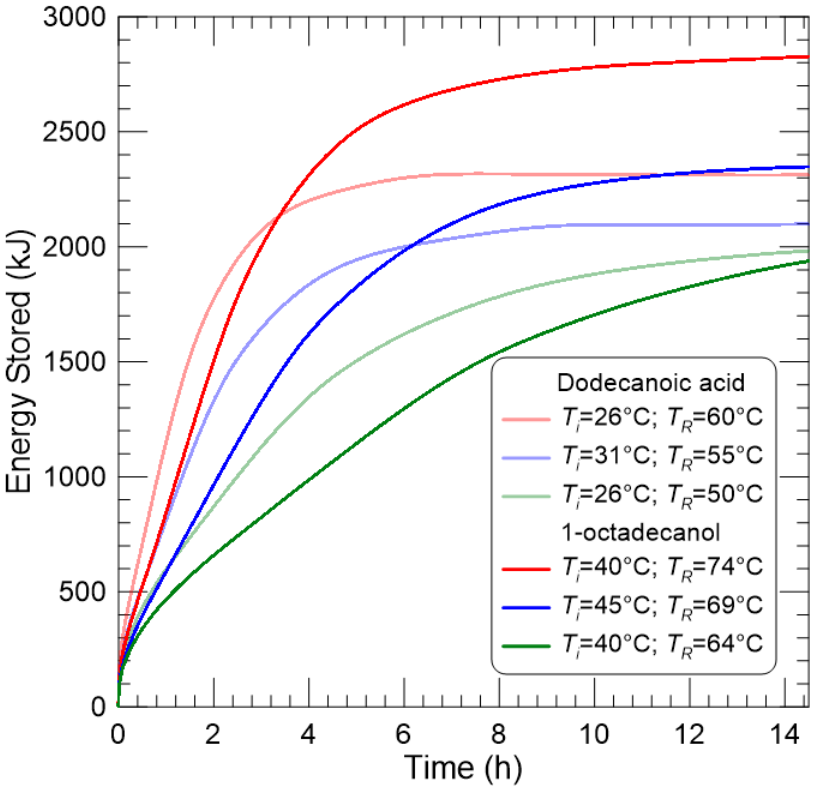

Figure 6.16: Energy vs time for charging experiments

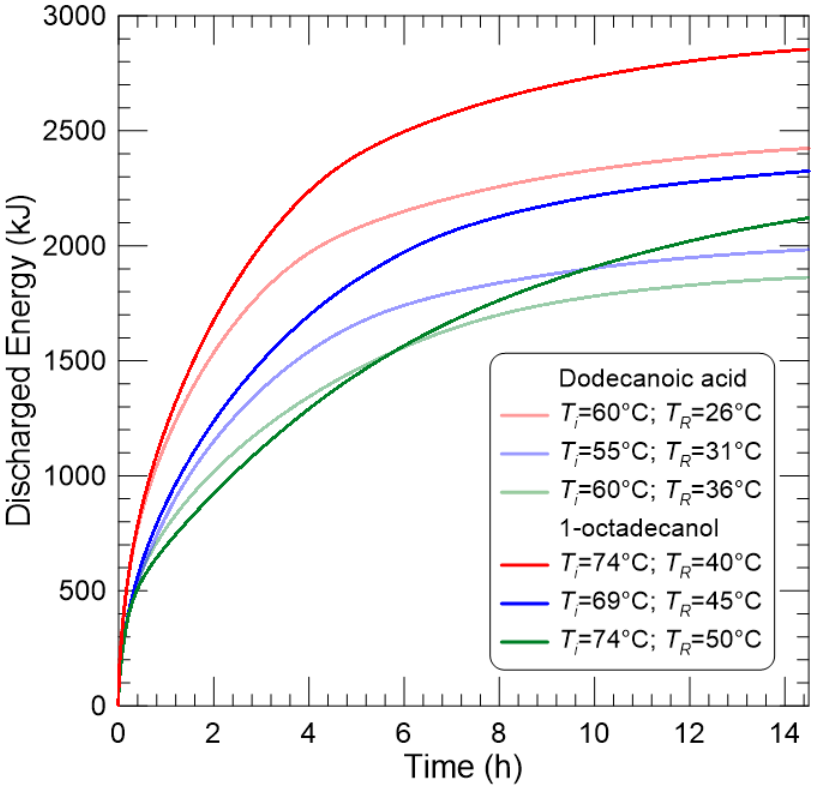

Figure 6.17: Energy vs time for discharging experiments

The results of discharging appear to vary less between PCM types than what is observed in charging. These results may be cause by the additional phase change occurring at a temperature lower than the melting temperature, resulting in a reduced temperature gradient. This may be why the discharging results seem to show similar power values throughout the initial part of the trial and then diverge off after this second phase change begins in 1-ocatdecanol, while the heat transfer in the charging experiments is observed to be greater for the duration of the trial, indicating superior natural convection during the melting process.

6.4 Data Reduction Approaches

Various data reduction approaches are utilized in the following sub-Sections in an attempt to develop relationships highlighting the impact of PCM properties on the heat transfer rate and energy storage exhibited by the system.

6.4.1 Effectiveness-NTU approach

The effectiveness-NTU approach, described in Section 2.9.1, has been utilized in literature to compare LHTES systems. However, the typical method of utilizing the melting temperature as the second reference point, as in Equation (6.1), simply reduces to a power of the system divided by the mass flow rate, specific heat of the HTF and the melting temperature differential (Equation 6.1), which would not change between PCM types. This would therefore not show any new information between the two PCMs and would therefore not be useful for the purposes of this study.

$$\varepsilon = \frac{T_{in} - T_{out}}{T_{in} - T_m} = \frac{Q(t)}{\dot{m} c_{p,HTF}(T_{in} - T_m)} \tag{6.1}$$

6.4.2 Comparing discharging results using Fourier number

The Fourier number, shown in Equation (6.2), is a dimensionless time which is used to characterize transient conduction problems. The Fourier number incorporates a ratio of the rate of conduction heat transfer over the rate of sensible energy stored (Bergman *et al.*, 2017).

$$Fo = \frac{\alpha\tau}{L_c^2} \tag{6.2}$$

In an attempt to compare the heat transfer results from both experiments using different PCMs, relations using the dimensionless Fourier number were explored similarly to what was done by Kuznik *et al.* (2015). Equation (6.2) demonstrates the Fourier number in which the value of thermal diffusivity, represented by α, was calculated for dodecanoic acid (0.07828 mm^2/s) and 1-octadecanol (0.1364 mm^2/s). Characteristic length, L_c, (20.4 mm) was calculated by dividing the volume of the PCM by the contact surface area of the heat exchanger. The value of τ is simply the measured discharging time of the PCM as the trial progresses. The Fourier number was used as a dimensionless time and the heat transfer of the system was plotted against this value. Due to the dominant effect of conduction heat transfer in discharging experiments, it is possible that the Fourier number could display relations between the heat transfer rate of the system using different PCMs. Results are shown in Figure 6.18 a) and b) for discharging experiments with various temperature changes.

These figures demonstrate that there is not a significant relationship between heat transfer of the system and the Fourier number of the specific PCM. This is indicative of perhaps more significant relationships which affect the heat transfer of the system in discharging involving the phase change, which the Fourier number does not account for. Charging results were also plotted despite the effects of natural convection not being able to be ignored and displayed no clear relationship.

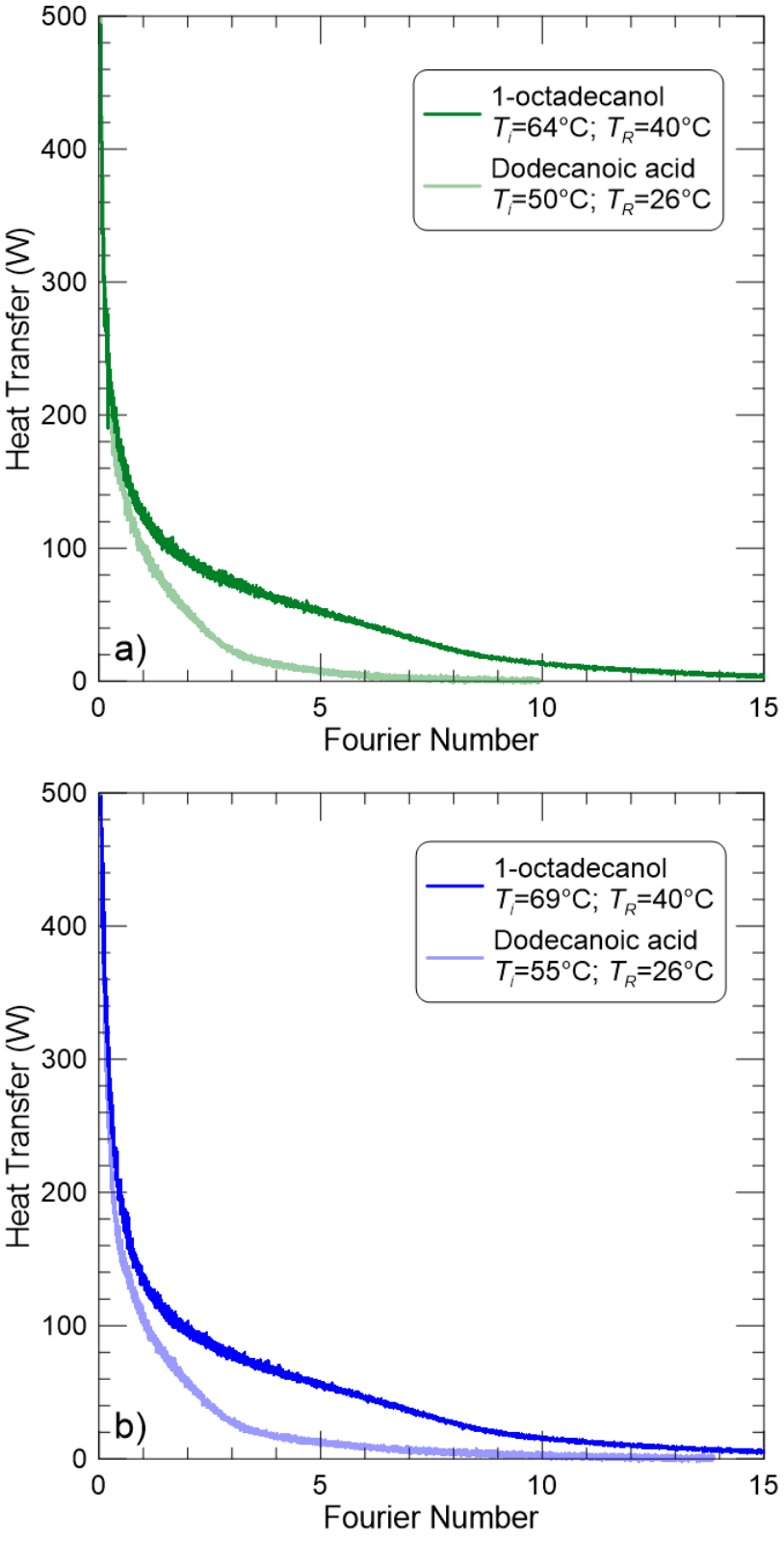

Figure 6.18: Heat transfer vs Fourier number for discharging experiment a) T_m +7°C; T_m -17°C b) T_m +12°C; T_m-17°C

6.4.3 Comparison of PCMs using Nusselt number

Utilizing another dimensionless parameter, an attempt was made to utilize a Nusselt number value defined by the author in an effort to find a common trend between the two PCMs in regard to their thermophysical properties. This parameter was defined by Equation (6.3),

$$Nu = \frac{Q(t)}{k_l \cdot \Delta T_m \cdot L_c} \tag{6.3}$$

where $Q(t)$ is the instantaneous heat transfer of the system, k is the thermal conductivity of the liquid PCM, ΔT_m is the melting temperature differential and L_c is the characteristic length. This value is plotted against the elapsed time of the experiment for charging trials, seen in Figures 6.19, 6.20 and 6.21.

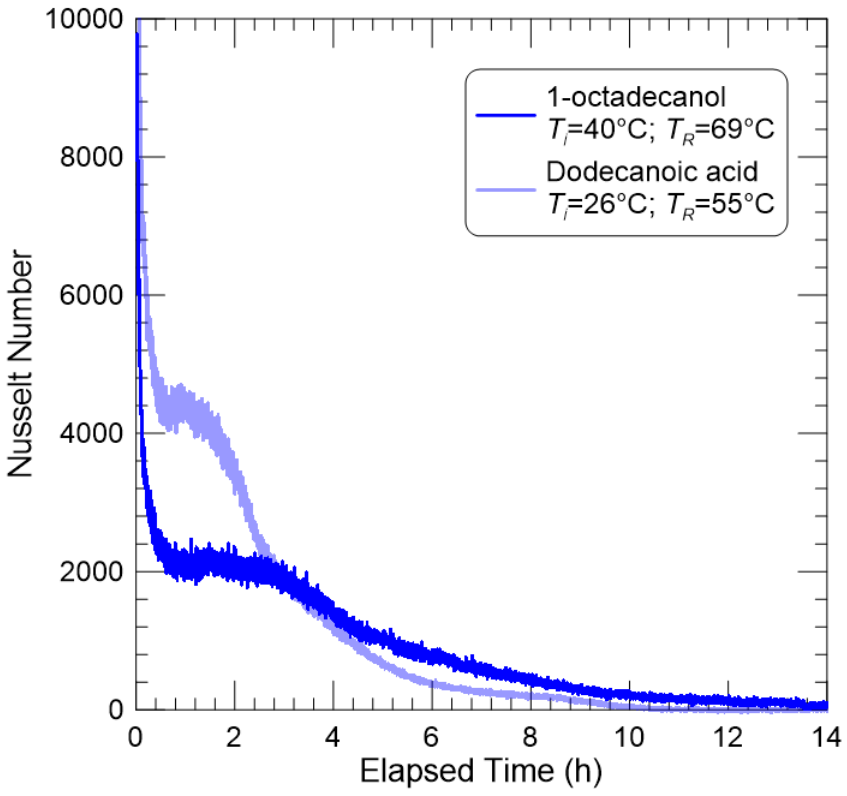

Figure 6.19: Nusselt number vs time for T_m-17°C; T_m+12°C

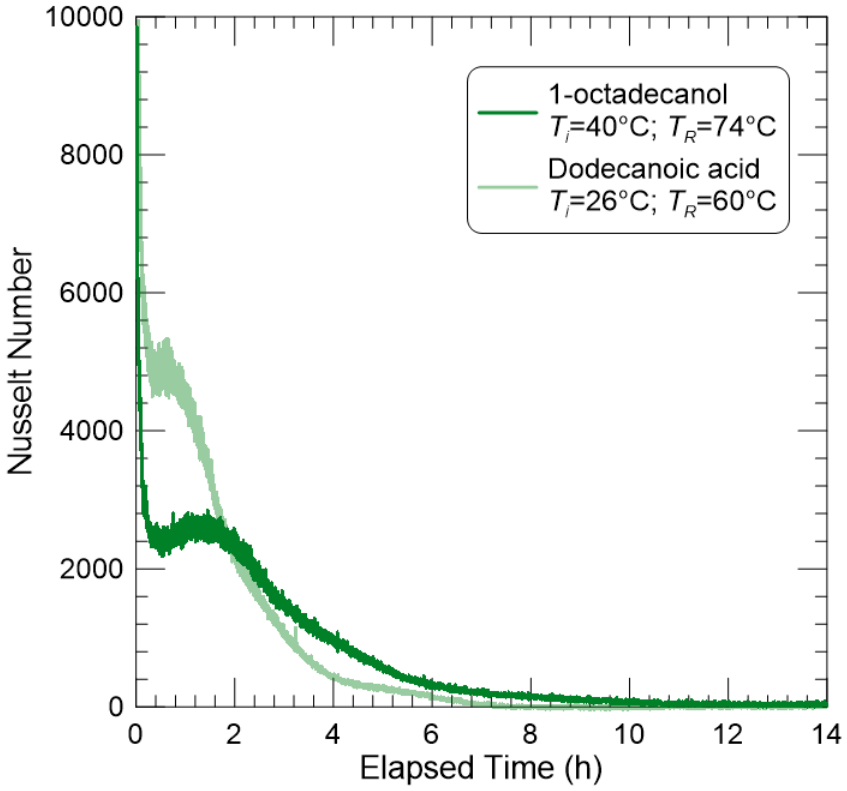

Figure 6.20: Nusselt number vs time for T_m-17°C; T_m+17°C

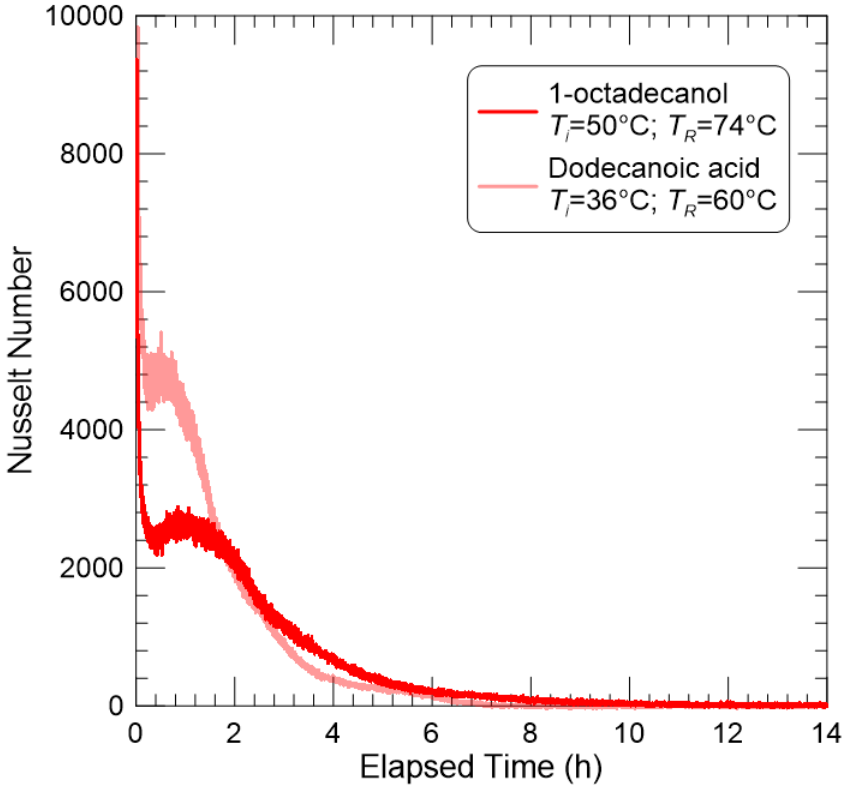

Figure 6.21: Nusselt number vs time for T_m-7°C; T_m+17°C

Results of this analytical approach do not produce conclusive results as no clear trend can be observed between the two PCMs studied. Using only the Nusselt number to reduce the data may not be the best method of comparison between PCMs as it only addresses the issue of thermal conductivity.

6.4.4 Comparison of PCMs using average power over total energy stored/discharged

In order to compare experiments using different PCMs and thus different heat transfer profiles, an average heat transfer rate could be utilized to quantify the entirety of the heat transfer process in one value. A simple arithmetic mean of the heat transfer rate taken over the duration of the trial may be skewed by the very low heat transfer rate at the end of the trials. Therefore the method developed by Lazaro *et al.* (2019) was taken using a weighted average of instantaneous heat transfer rate over the energy stored in the system during this interval. This reduces the impact of the low power values near the end of the trial as they also result in minute amounts of energy being added to the system.

This average heat transfer is referred to as the Q_{mean} and is a function of the heat transfer integrated over the energy stored/discharged divided by the total energy stored/discharged as described in Section 2.9.4 and shown in Equation (6.4).

$$Q_{mean} = \frac{\int_0^{E_{tot}} Q(E)dE}{E_{tot}} \tag{6.4}$$

The effects of Q_{mean} are demonstrated by plotting it against a dimensionless temperature difference through the Stefan number. The Stefan number defined by the melting temperature differential (Ste_m) was used for comparing charging trials as in Equation (6.5), while the Stefan number defined by the solidification temperature differential (Ste_s) was used for discharging trials, sas een in Equation (6.6). Plotting against this Stefan number relates the temperature differential driving the heat transfer process as well as the storage properties specific to the PCM used in the system to the heat transfer rate observed in the system. Figure 6.23 presents Q_{mean} for both melting and solidification trials for both dodecanoic acid and 1-octadecanol. In order to determine the validity of this parameter, results are also plotted against the simple melting temperature differential (ΔT_m) for charging experiments and the solidification temperature differential (ΔT_s) for discharging

experiments. These results are seen in Figure 6.22.

$$Ste_m = \frac{c_{p,l}\Delta T_m}{L} \tag{6.5}$$

$$Ste_s = \frac{c_{p,s}\Delta T_s}{L} \tag{6.6}$$

These figures show a positive correlation between Stefan number and Q_{mean} for both melting and solidification experiments. The trend observed in the melting experiments is stronger than in the discharging experiments, demonstrating that the effect of melting Stefan number may be more significant for charging experiments than solidification Stefan number is to discharging experiments. When looking at Figure 6.22 it is clear from the R^2 values observed, (0.946 for charging and 0.010 for discharging), that plotting against the melting and solidification temperature differential produces a weaker correlation when comparing two different PCMs than plotting against the melting and solidification Stefan numbers (R^2 values of 0.963 for charging and 0.162 for discharging).

While this proves to be true, the difference between the two sets of plots is small and the results of Figure 6.23 still do not show a strong relationship between Stefan number and Q_{mean} independent of PCM type, especially for discharging experiments.

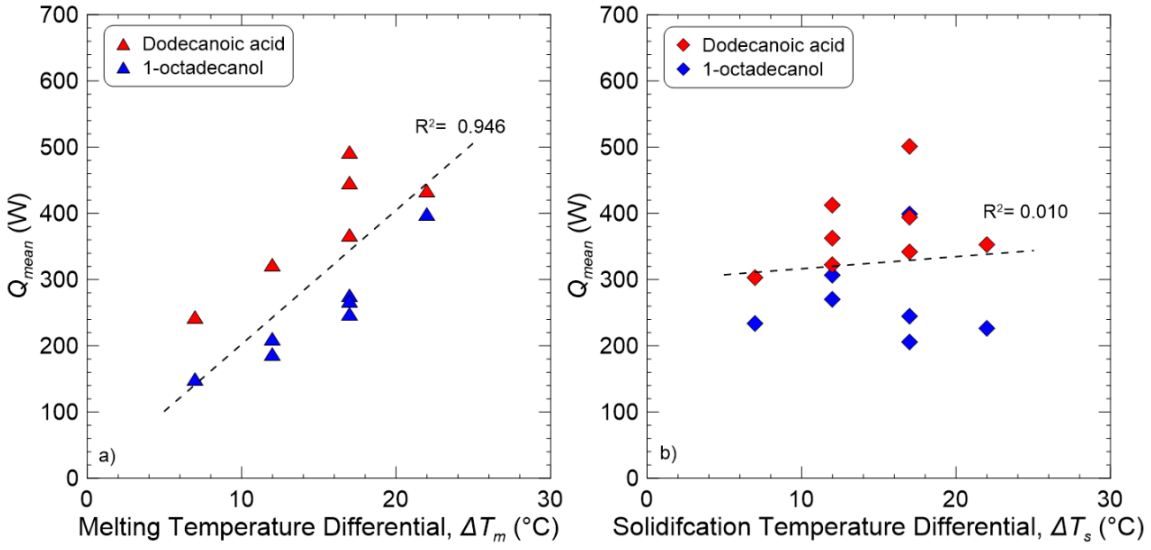

Figure 6.22: Q_{mean} vs a) melting temperature differential and b) solidification temperature differential

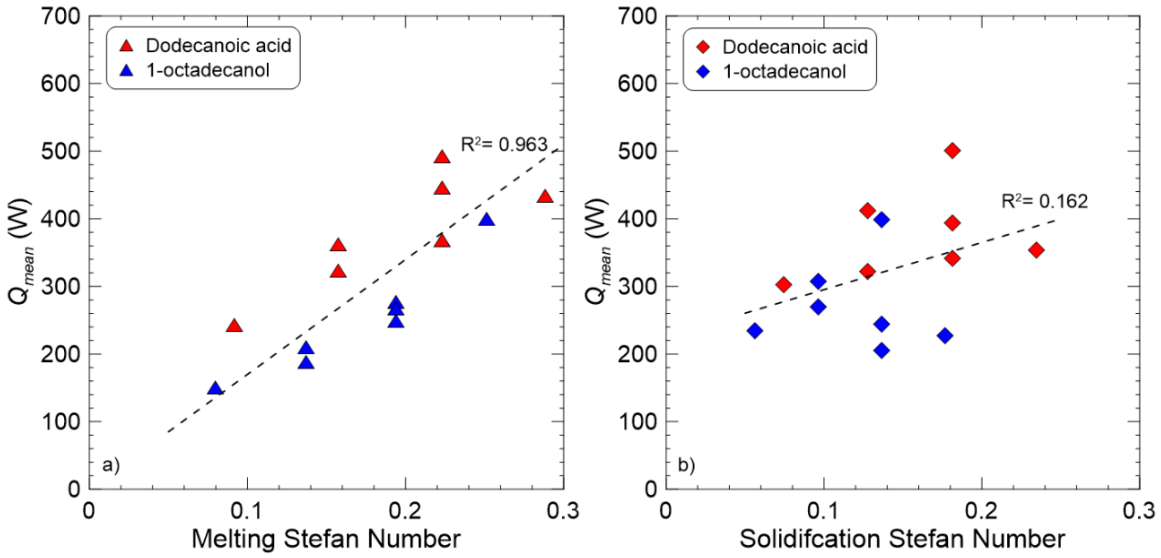

Figure 6.23: Q_{mean} vs a) melting Stefan number and b) solidification Stefan number

Another Stefan number can be defined in order to explore the effect of the entire range of operating temperatures on the system. The total Stefan number (Ste_t) is defined by Equation (6.7) and incorporates both the initial and final PCM temperatures. In charging experiments, T_c represents the initial PCM temperature, and T_h the HTF temperature.

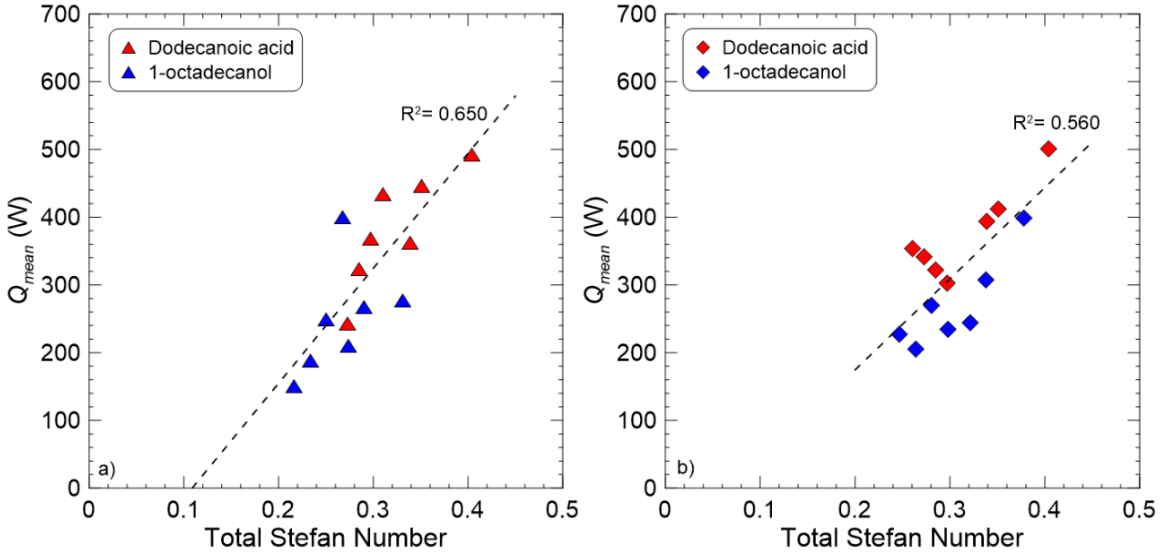

Figure 6.24: Q_{mean} vs total Stefan number for a) charging and b) discharging

Conversely, in discharging experiments, T_h corresponds to the initial PCM temperature, while T_c denotes the HTF temperature.

$$Ste_t = \frac{c_{p,l}|T_h - T_m| + c_{p,s}|T_m - T_c|}{L} \tag{6.7}$$

The correlation observed in charging is similar to Figure 6.23 a), however a stronger correlation is observed in discharging experiments when the total Stephan number, Ste_t is plotted against Q_{mean}, shown in Figure 6.24, demonstrating that perhaps that the effect of initial temperature, at least for discharging is more significant than once predicted. The intercept of the trend for both charging and discharging results clearly travels below the *x*-axis which implies that for low total Stefan numbers there would be zero or negative heat transfer rates. This points to a linear relationship not necessarily being the correct trend to fit the data. It is unclear whether this method could be more successful for discharging experiments.

6.4.5 Comparison of PCMs using normalized average power over total energy stored/discharged

Authors like Medrano et al. (2009) and Lazaro et al. (2019) have attempted to derive the normalized average heat transfer rate. The approach used by Medrano *et al.* (2009) involved reducing the average heat transfer of the system by the temperature range of the system as well as the heat transfer surface area, as in Equation (6.8).

$$Q_{therm} = \frac{Q_{avg}}{A \cdot \Delta T_{avg}} \tag{6.8}$$

This approach could be useful for instances when the geometry of the system was being changed and therefore created a change in heat transfer surface area. The use of this metric for this study would not show any new information since the geometry remains the same, while only the PCM is changing.

The method of normalizing introduced by Lazaro *et al.* (2019) is built upon Q_{therm} and is defined as the average heat transfer rate obtained over the stored energy (called normative power, Q_{norm}) per unit temperature difference, where this temperature difference was taken to be the difference between the HTF and the PCM melting temperature (T_R -T_m), per unit volume of the PCM (V_{PCM}), similarly to Patil (2020). This normalized average heat transfer rate is known as the normative power, Q_{norm}, and is shown in Equation (6.9). Figure 6.25

displays Q_{norm} plotted against the Ste_m and Ste_s for both PCM types.

$$Q_{norm} = \frac{Q_{mean}}{V_{PCM} \cdot |T_R - T_m|} \tag{6.9}$$

Figure 6.25 demonstrates a negative trend for both charging and discharging experiments, and the R^2 values observed are quite small for both plots. The weak relationship observed, demonstrates that perhaps this metric may not be optimal for the comparison of the results presented in this study.

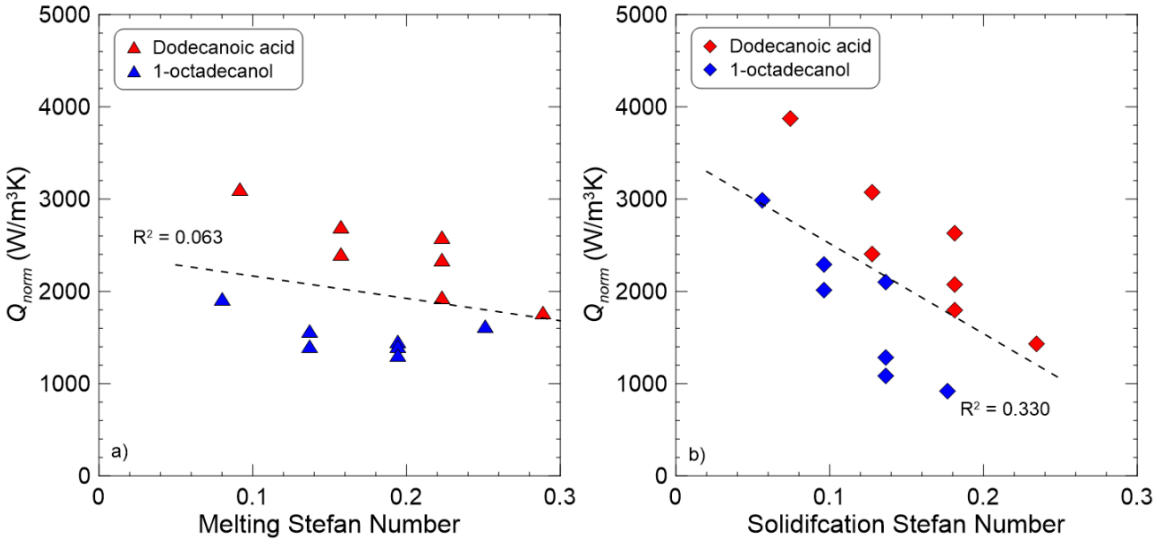

Figure 6.25: Q_{norm} vs a) melting Stefan number and b) solidification Stefan number

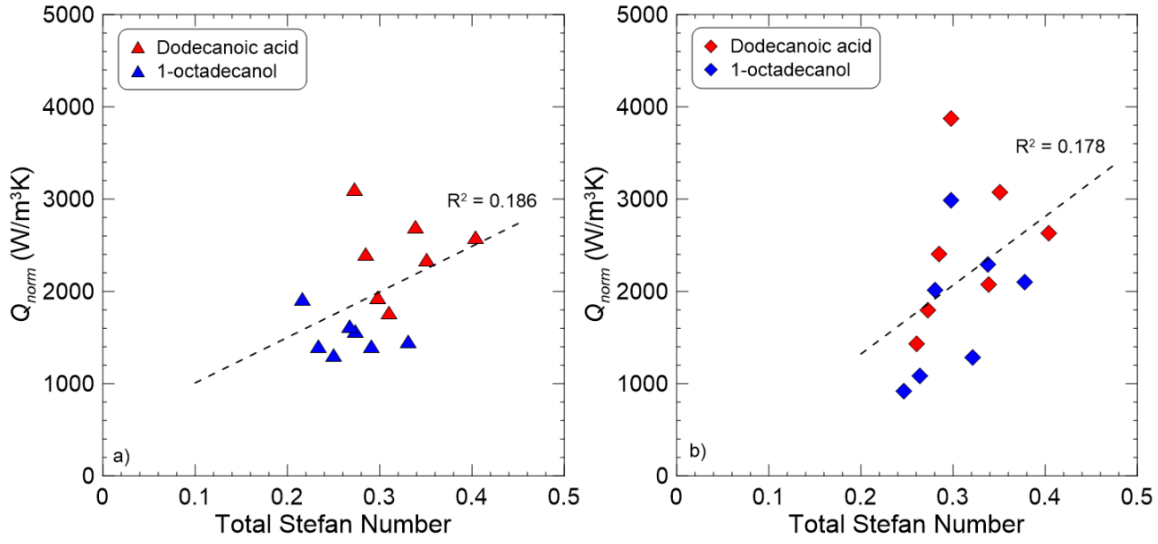

Figure 6.26: Q_{norm} vs total Stefan number for a) charging and b) discharging

Similarly to Figure 6.24, Q_{norm} was plotted against the total Stefan number seen in Figure 6.26. These results show a very weak positive correlation with Q_{norm} and the total Stefan number. Once again, the lack of a convincing relationship may indicate that these metrics may not be ideal for the comparison of multiple PCMs.

A different normalized average heat transfer was used in this study by replacing the melting temperature differential with total temperature difference of the process instead. This value uses the same method as Equation (6.9) but where the temperature difference used was taken to be the difference between the HTF and the initial PCM temperature (T_i -T_R), per unit volume of the PCM (V_{PCM}). Calling this normalized average heat transfer rate $Q_{norm,t}$, shown in Equation (6.10).

$$Q_{norm,t} = \frac{Q_{mean}}{V_{PCM} \cdot |T_i - T_R|} \tag{6.10}$$

The results of $Q_{norm,t}$ were once again plotted against Ste_m, Ste_s and Ste_t, as in Figures 6.27 and 6.28.

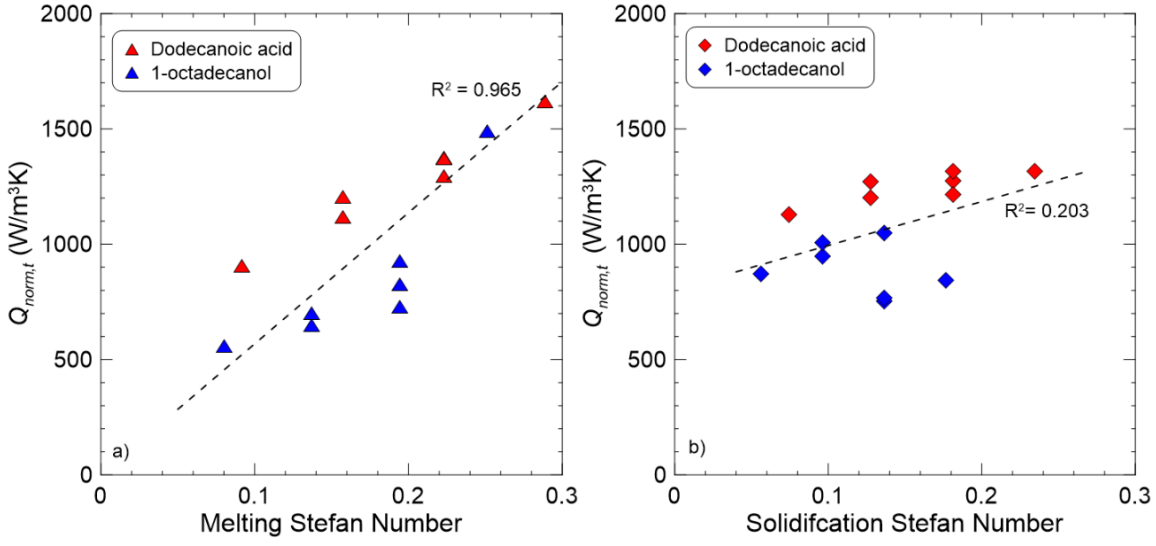

Figure 6.27: $Q_{norm,t}$ vs a) melting Stefan number and b) solidification Stefan number

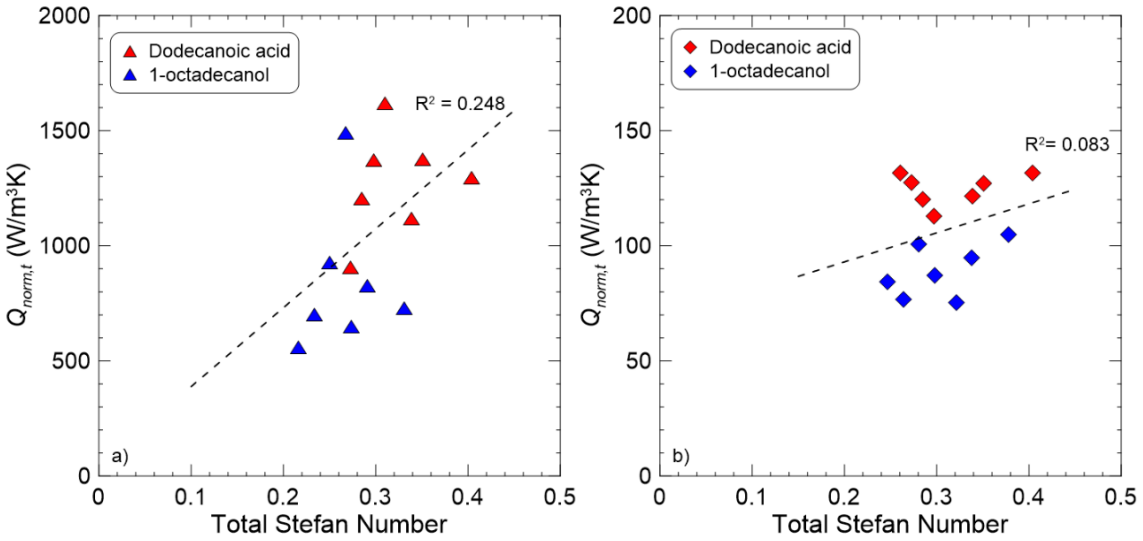

Figure 6.28: $Q_{norm,t}$ vs total Stefan number for a) charging and b) discharging

The data from Figure 6.27 presents a similar correlation than observed for the Q_{mean} plots of Figure 6.23, with a slightly stronger correlation. When the R^2 values of this plot (0.965 for charging and 0.203 for discharging) are compared to those from Figure 6.23 (0.963 and 0.162), it is clear that this relationship is nearly the same. The relationship observed for discharging is still extremely weak which denotes that perhaps the use of Stefan number may not be ideal for comparison of discharging results. The results using total Stefan number as the dependant variable, much like those observed in Figure 6.26, show no clear indication of any discernable correlation.

6.5 Conclusion

This Chapter compared results obtained experimentally, using two different types of PCMs in an LHTES system. Results for charging indicate that 1-octadecanol has a lower heat transfer rate than dodecanoic acid, while also reaching higher stored energy levels. This reduced heat transfer rate was notable as the thermal conductivity, a significant property in conduction heat transfer, was greater for 1-octadecanol than for dodecanoic acid. The observed results signify that this property is not as significant in the heat transfer of the system as other factors. The difference of the viscosity of the PCM was determined to be the significant property causing this variation of heat transfer rates between the two PCMs in the charging experiments. Discharging experiments showed similar results, however the

reasoning behind the difference in heat transfer rates in the system was determined to be different. Due to the lack of natural convection in the discharging process, the results can be explained by the lower temperature at which the solid-solid phase transition occurs creating a lower temperature differential resulting in a lower heat transfer rate for 1-octadecanol.

Performance indicators which reduce the heat transfer of the system to one number, such as the Q_{mean}, Q_{norm}, (defined in literature) and $Q_{norm,t}$ (defined by the author and adapted from metrics in literature), were used to attempt to find trends between the results of both PCMs used in this study. The results were plotted against the melting and solidification Stefan numbers as well as the total Stefan numbers. Results plotted against melting and solidification Stefan numbers were compared with results using a simple melting or solidification temperature differential. It was found that the use of Stefan number, which incorporates the PCM properties of c_p and L improves the correlation between PCMs, if only slightly.

The most promising results are those comparing the Q_{mean} of charging results with the melting Stefan number, which demonstrate the increasing the Stefan number (and thus the melting temperature differential) increases the average heat transfer of the system. These results are still not strong which indicates that the Stefan number alone is not suitable for analyzing the data retrieved from this study. Another factor apart from Stefan number may need to be included in the analysis of the LHTES system. For melting this factor may be the effect of viscosity on the natural convection, as discussed in Section 6.1.

Discharging results show even weaker correlations for both PCMs with little evidence of a correlation. The strongest results are those which compare Q_{mean} with the total Stefan number, however this correlation is still not significant enough to determine whether this method could be successful in comparing results for LHTES systems. From the results observed it may be necessary for another metric to be developed in order to fully understand the effects of PCM on the heat transfer during discharging.

Chapter 7: Conclusion

Characterization of LHTES systems in an effort to develop design rules is a central focus of research in the field of PCM-TES today. Experimental and numerical approaches employing a multitude of characterization techniques such as using different geometries, varying operating parameters and adding material or fins have been thoroughly explored in literature. Understanding the full picture of how LHTES systems can be designed and optimized involves many factors including those mentioned. One factor, however which has not been thoroughly explored in literature is the effect of the PCM on the system. The use of different PCMs could impact the heat transfer, energy storage and overall effectiveness of LHTES systems. There are many thermophysical properties which effect these parameters and determining the significance of each and how it affects the system requires the creation of comparison metrics based on PCM properties alone, which currently do not exist in literature. It is up to researchers then, to explore what performance indicators can be applied to PCM-TES systems and utilize these performance indicators to perform sensitivity analyses to determine the most significant PCM properties for characterizing LHTES systems.

This study looked to explore the effect of PCM on an experimental coil-in-shell LHTES system in an effort to understand which PCM properties are the most significant in the design of these systems. The LHTES was tested with two different types of PCMs, namely dodecanoic acid and 1-octadecanol. Results were compared under the same representative operating conditions, varying only the PCM type for different sets of experiments. The experiments performed were categorized by operating temperature and consisted of trials of equivalent energies, identical initial PCM temperatures and identical HTF temperatures. Trials of increased HTF flow rate were also performed for dodecanoic acid in order to determine the significance of this operating parameter. The following results were obtained from this study:

- Increased heat transfer is strongly associated with the differential between T_R and T_m for both PCMs.
- Increasing the differential between T_i and T_m affects the heat transfer very

minimally for charging experiments but seems to play a larger role in the conduction dominated discharging experiments regardless of PCM type.

- Increasing HTF flow rate has a negligible effect on heat transfer within the range of flow rate used in this work.
- Dodecanoic acid initially has a higher heat transfer rate in both charging and discharging experiments than 1-octadecanol, however 1-octadecanol experiences a higher heat transfer rate towards the end of experiments and stores/discharges more energy.

It is concluded that the higher latent heat value of 1-octadecanol is responsible for the higher energy storage values observed during the charging and discharging experiments when compared to dodecanoic acid. Initially, the significance of the thermal conductivity was thought to play a large role in the heat transfer rate in the system, however despite its higher thermal conductivity, 1-octadecanol was observed to have a lower average heat transfer value for both charging and discharging experiments. This could be explained by two separate physical effects. For charging experiments the reduced heat transfer observed in 1-octadecanol was caused by a reduced effect of natural convection due to an increased viscosity as well as the delayed onset of natural convection due to the solid-solid transformation occurring before melting. In discharging the solid-solid phase change occurring at temperatures at 50°C, which is 8°C lower than the melting point, reduces the temperature differential driving the heat transfer by a significant amount while this phase change occurs. This ultimately reduces the average overall heat transfer rate of 1-octadecanol.

Various approaches were undertaken in order to reduce the data in order to numerically compare data from each set of experiments. These methods include plotting the instantaneous heat transfer against Fourier number, plotting average heat transfer rate per unit stored energy against Ste_m and Ste_s and plotting a normalized heat transfer against Ste_m and Ste_s. The use of Fourier number as a dimensionless time showed insignificant results demonstrating that the effect of thermal diffusivity alone through this dimensionless number could not explain variation in heat transfer observed.

The results of methods using Q_{mean}, Q_{norm} and $Q_{norm,t}$ plotting against the Ste_m, Ste_s and Ste_t lead to promising results involving the comparison of the Q_{mean} of charging experiments with the Ste_m. These results demonstrated a positive correlation which further supports the theory that the driving force in charging experiments is the T_R. The results for discharging experiments showed weak relationships with no results reaching R^2 values greater than 0.6. It is notable that plotting the Q_{mean} against the total Stefan number produced the strongest linear relationship for discharging, perhaps due to the inclusion of the initial PCM temperature in the equation, however this relationship was still not significant enough for the author to deem it viable for use going forward. These uncorrelated results show that the Stefan number may not be the best metric for comparing results of discharging experiments and that other parameters may be needed to be explored in order to fully understand this physical process. The results using Q_{norm} and $Q_{norm,t}$ displayed no new information than those using Q_{mean} and displayed results lacking correlations for some instances. This demonstrates that these parameters may not be useful for the results of this study.

Future work involving more types of PCMs under identical conditions is recommended in order to observe a more obvious trend between PCM properties and heat transfer values. The possible use of the PCMs considered but not chosen in this study, such as PEG-1000 and eicosane could be those used for future research. More data points would help establish a more obvious trend in these experiments. It is recommended that the effect of PCM viscosity be analyzed for charging experiments as this appears to be a significant metric in influencing the natural convection on the system. For further studies pursued using multiple PCMs, it is recommended that PCMs with similar phase change characteristics (i.e., number of phase changes) are used for the study, as this remains a difficult characteristic to quantify in any data reduction techniques. It is also recommended to explore a new metric using Ste_m along with other parameters such as viscosity as the basis for comparing charging trials as this may lead to more concrete results in determining its impact on the average heat transfer rate. Investigations into the effects on subcooling Stefan number should also be considered in order to understand the effects of initial temperature, especially on discharging experiments.

Finally, as the various approaches used to highlight the impact of PCM properties in this thesis did not show clear trends and success, it might be time, and there is now the start of the data needed for it, to perform a complete dimensionless analysis in order to determine better comparison metrics.

References

Agarwal, A., & Sarviya, R. (2016). An experimental investigation of shell and tube latent heat storage for solar dryer using paraffin wax as heat storage material. *Engineering Science and Technology, an International Journal*, 619-631.

Agyenim, F., Hewitt, N., Eames, P., & Smyth, M. (2010). A review of materials, heat transfer and phase change problem formulation for latent heat thermal energy storage systems (LHTESS). *Renewable and Sustainable Energy Reviews*, 615-628.

Al-Abidi, A. A., Mat, S., Sopian, K., Sulaiman, M., & Mohammad, A. T. (2014). Experimental study of melting and solidification of PCM in a triplex tube heat exchanger with fins. *Energy and Buildings*, 33-41.

Alawadhi, E. M. (2008). Thermal analysis of a building brick containing phase change material. *Energy and Buildings*, 351-357.

Allouche, Y., Varga, S., Bouden, C., & Oliveira, A. C. (2015). Experimental determination of the heat transfer and cold storage characteristics of a microencapsulated phase change material in a horizontal tank. *Energy Conversion and Management*, 275-285.

Alnakeeb, M. A., Salam, M. A. A., & Hassab, M. A. (2021). Eccentricity optimization of an inner flat-tube double-pipe latent-heat thermal energy storage unit. *Case Studies in Thermal Engineering*, 14.

Amin, N. A. M., Belusko, M., & Bruno, F. (2014). An effectiveness-NTU model of a packed bed PCM thermal storage system. *Applied Energy*, 356-362.

Amin, N. A. M., Bruno, F., & Belusko, M. (2012). Effectiveness–NTU correlation for low temperature PCM encapsulated in spheres. *Applied Energy*, 549-555.

Anderson, D. (1966). Thermal conductivity of polymers. *Chemical Reviews*, 677-690.

Azad, M., Groulx, D., & Donaldson, A. (2021). Natural convection onset during melting of phase change materials: Part I–Effects of the geometry, Stefan number, and degree of subcooling. *International Journal of Thermal Sciences*, 16.

Azad, M., Groulx, D., & Donaldson, A. (2022). Natural convection onset during melting of phase change materials: Part III–Global correlations for onset conditions. *International Journal of Thermal Sciences*, 9.

Aziz, N., Amin, N., Majid, M., Bruno, F., & Belusko, M. (2022). Optimising a packed bed phase change material of spheres using effectiveness-number of transfer unit method. *Journal of Energy Storage*, 10.

Bastani, A., Haghighat, F., & Kozinski, J. (2014). Designing building envelope with PCM wallboards: Design tool development. *Renewable and Sustainable Energy Reviews*, 554-562.

Bauer, T. (2011). Approximate analytical solutions for the solidification of PCMs in fin geometries using effective thermophysical properties. *International Journal of Heat and Mass Transfer*, 4923-4930.

Belusko, M., Halawa, E., & Bruno, F. (2012). Characterising PCM thermal storage systems using the effectiveness-NTU approach. *International Journal of Heat and Mass Transfer*, 3359-3365.

Bergman, T., Incropera, F., & DeWitt, D. (2017). *Fundamentals of Heat and Mass Transfer; Bergman, TL, Lavine, AS, Eds*. John Wiley & Sons, Inc.: Hoboken, NJ, USA. 1048.

Beyne, W., T'Jollyn, I., Lecompte, S., Cabeza, L., & De Paepe, M. (2023). Standardised methods for the determination of key performance indicators for thermal energy storage heat exchangers. *Renewable and Sustainable Energy Reviews*, 19.

Cabeza, L., & Heinz, A. (2005). *Inventory of phase change materials (PCM)* (A report of iea solar heating and cooling programme—task, Issue. 33 p

Cabeza, L. F. (2021). *Advances in Thermal Energy Storage Systems: Methods and Applications* (2nd ed.). Elsevier. 755.

Cabeza, L. F., Castell, A., Barreneche, C. d., De Gracia, A., & Fernández, A. (2011). Materials used as PCM in thermal energy storage in buildings: A review. *Renewable and Sustainable Energy Reviews*, 1675-1695.

Callaghan, R. L., D'Oliveira, E. J., Groulx, D., & Pereira, S. C. C. (2023). *Characterization of a small-scale PCM-heat exchanger: impact of PCM selection* IHTC-17, Cape Town (South Africa). 10 p

Castell, A., Belusko, M., Bruno, F., & Cabeza, L. F. (2011). Maximisation of heat transfer in a coil in tank PCM cold storage system. *Applied Energy*, 4120-4127.

Castellón, C., Martorell, I., Cabeza, L. F., Fernández, A. I., & Manich, A. (2011). Compatibility of plastic with phase change materials (PCM). *International Journal of Energy Research*, 765-771.

Chen, X., Worall, M., Omer, S., Su, Y., & Riffat, S. (2014). Experimental investigation on PCM cold storage integrated with ejector cooling system. *Applied Thermal Engineering*, 419-427.

Das, S. K., Choi, S. U., Yu, W., & Pradeep, T. (2007). *Nanofluids: science and technology*. John Wiley & Sons. 416.

Desgrosseilliers, L., Whitman, C. A., Groulx, D., & White, M. A. (2013). Dodecanoic acid as a promising phase-change material for thermal energy storage. *Applied Thermal Engineering*, 37-41.

Diaconu, B. M., Cruceru, M., & Anghelescu, L. (2023). A critical review on heat transfer enhancement techniques in latent heat storage systems based on phase change materials. Passive and active techniques, system designs and optimization. *Journal of Energy Storage*, 48.

Eslami, M., Khosravi, F., & Kohan, H. F. (2021). Effects of fin parameters on performance of latent heat thermal energy storage systems: A comprehensive review. *Sustainable Energy Technologies and Assessments*, 16.

Fang, Y., Niu, J., & Deng, S. (2019). An analytical technique for the optimal designs of tube-in-tank thermal energy storage systems using PCM. *International Journal of Heat and Mass Transfer*, 849-859.

Garg, H., Pandey, B., Saha, S. K., Singh, S., & Banerjee, R. (2018). Design and analysis of PCM based radiant heat exchanger for thermal management of buildings. *Energy and Buildings*, 84-96.

Gasia, J., Tay, N. S., Belusko, M., Cabeza, L. F., & Bruno, F. (2017). Experimental investigation of the effect of dynamic melting in a cylindrical shell-and-tube heat exchanger using water as PCM. *Applied Energy*, 136-145.

Groulx, D. (2018). The rate problem in solid-liquid phase change heat transfer: Efforts and questions toward heat exchanger design rules. Proceedings of the 16th International Heat Transfer Conference (IHTC-16), Beijing, China, 16 p

Groulx, D., Castell, A., & Solé, C. (2021). Design of latent heat energy storage systems using phase change materials. In *Advances in Thermal Energy Storage Systems* (pp. 331-357). Elsevier.

Gürel, B. (2020). A numerical investigation of the melting heat transfer characteristics of phase change materials in different plate heat exchanger (latent heat thermal energy storage) systems. *International Journal of Heat and Mass Transfer*, 19.

Han, G.-S., Ding, H.-S., Huang, Y., Tong, L.-G., & Ding, Y.-L. (2017). A comparative study on the performances of different shell-and-tube type latent heat thermal energy storage units including the effects of natural convection. *International Communications in Heat and Mass Transfer*, 228-235.

Hayat, M. A., Chen, Y., Bevilacqua, M., Li, L., & Yang, Y. (2022). Characteristics and potential applications of nano-enhanced phase change materials: A critical review on recent developments. *Sustainable Energy Technologies and Assessments*, 36.

Herbinger, F., & Groulx, D. (2022). Experimental comparative analysis of finned-tube PCM-heat exchangers' performance. *Applied Thermal Engineering*, 12.

Joseph, A., Kabbara, M., Groulx, D., Allred, P., & White, M. A. (2016). Characterization and real-time testing of phase-change materials for solar thermal energy storage. *International Journal of Energy Research*, 61-70.

Kahwaji, S., Johnson, M. B., Kheirabadi, A. C., Groulx, D., & White, M. A. (2017a). Fatty acids and related phase change materials for reliable thermal energy storage at moderate temperatures. *Solar energy materials and solar cells*, 109-120.

Kahwaji, S., White, M. A., & Groulx, D. (2017b). *Thermophysical Properties, Chemical Compatibility and Thermal Stability of Phase Change Materials Selected for Fanless Cooling of Portable Electronics* 67 p

Kalapala, L., & Devanuri, J. K. (2018). Influence of operational and design parameters on the performance of a PCM based heat exchanger for thermal energy storage–A review. *Journal of Energy Storage*, 497-519.

Kibria, M., Anisur, M., Mahfuz, M., Saidur, R., & Metselaar, I. (2014). Numerical and experimental investigation of heat transfer in a shell and tube thermal energy storage system. *International Communications in Heat and Mass Transfer*, 71-78.

König-Haagen, A., & Diarce, G. (2023). Prediction of the discharging time of a latent heat thermal energy storage system with a UA approach. *Journal of Energy Storage*, 21.

Kou, Y., Wang, S., Luo, J., Sun, K., Zhang, J., Tan, Z., & Shi, Q. (2019). Thermal analysis and heat capacity study of polyethylene glycol (PEG) phase change materials for thermal energy storage applications. *The Journal of Chemical Thermodynamics*, 259-274.

Kousha, N., Rahimi, M., Pakrouh, R., & Bahrampoury, R. (2019). Experimental investigation of phase change in a multitube heat exchanger. *Journal of Energy Storage*, 292-304.

Kumar, N., Hirschey, J., LaClair, T. J., Gluesenkamp, K. R., & Graham, S. (2019). Review of stability and thermal conductivity enhancements for salt hydrates. *Journal of Energy Storage*, 15.

Kumar, R., Pandey, A., Samykano, M., Mishra, Y. N., Mohan, R., Sharma, K., & Tyagi, V. (2022). Effect of surfactant on functionalized multi-walled carbon nano tubes enhanced salt hydrate phase change material. *Journal of Energy Storage*, 15.

Kuznik, F., Lopez, J. P. A., Baillis, D., & Johannes, K. (2015). Design of a PCM to air heat exchanger using dimensionless analysis: Application to electricity peak shaving in buildings. *Energy and Buildings*, 65-73.

Lazaro, A., Delgado, M., König-Haagen, A., Höhlein, S., & Diarce, G. (2019). Technical performance assessment of phase change material components. Proceedings of the SHC 2019 International Conference on Solar Heating and Cooling for Building and Industry, Santiago, Chile, 12 p

Li, J., Zhang, Y., Peng, Z., Zhang, X., Zhai, J., Luo, Y., Liu, B., Sun, X., & Al-Saadi, S. N. (2023). Thermal performance of a plate-type latent heat thermal energy storage heat exchanger-An experimental investigation and simulation study. *Journal of Energy Storage*, 14.

Li, M.-J., Jin, B., Ma, Z., & Yuan, F. (2018). Experimental and numerical study on the performance of a new high-temperature packed-bed thermal energy storage system with macroencapsulation of molten salt phase change material. *Applied Energy*, 15.

Liang, H., Niu, J., Annabattula, R. K., Reddy, K., Abbas, A., Luu, M. T., & Gan, Y. (2022). Phase change material thermal energy storage design of packed bed units. *Journal of Energy Storage*, 16.

López-Navarro, A., Biosca-Taronger, J., Corberán, J., Peñalosa, C., Lázaro, A., Dolado, P., & Payá, J. (2014). Performance characterization of a PCM storage tank. *Applied Energy*, 151-162.

Mahdi, M. S., Mahood, H. B., Alammar, A. A., & Khadom, A. A. (2021). Numerical investigation of PCM melting using different tube configurations in a shell and tube latent heat thermal storage unit. *Thermal Science and Engineering Progress*, 9.

Mahdi, M. S., Mahood, H. B., Mahdi, J. M., Khadom, A. A., & Campbell, A. N. (2020). Improved PCM melting in a thermal energy storage system of double-pipe helical-coil tube. *Energy Conversion and Management*, 11.

Mao, Q., Chen, K., & Li, T. (2022). Heat transfer performance of a phase-change material in a rectangular shell-tube energy storage tank. *Applied Thermal Engineering*, 15.

Mao, Q., & Zhang, Y. (2020). Thermal energy storage performance of a three-PCM cascade tank in a high-temperature packed bed system. *Renewable Energy*, 110-119.

Martin, M., Villalba, A., Fernández, A. I., & Barreneche, C. (2019). Development of new nano-enhanced phase change materials (NEPCM) to improve energy efficiency in buildings: Lab-scale characterization. *Energy and Buildings*, 75-83.

Mat, S., Al-Abidi, A. A., Sopian, K., Sulaiman, M. Y., & Mohammad, A. T. (2013). Enhance heat transfer for PCM melting in triplex tube with internal–external fins. *Energy Conversion and Management*, 223-236.

Medrano, M., Yilmaz, M., Nogués, M., Martorell, I., Roca, J., & Cabeza, L. F. (2009). Experimental evaluation of commercial heat exchangers for use as PCM thermal storage systems. *Applied Energy*, 2047-2055.

Moffat, R. J. (1988). Describing the uncertainties in experimental results. *Experimental thermal and fluid science*, 3-17.

Morovat, N., Athienitis, A. K., Candanedo, J. A., & Dermardiros, V. (2019). Simulation and performance analysis of an active PCM-heat exchanger intended for building operation optimization. *Energy and Buildings*, 47-61.

Nguyen, T. P., Ramadan, Z., Hong, S. J., & Park, C. W. (2022). Effect of graphite fin on heat transfer enhancement of rectangular shell and tube latent heat storage. *International Journal of Heat and Mass Transfer*, 14.

Pahamli, Y., Hosseini, M., Ranjbar, A., & Bahrampoury, R. (2018). Inner pipe downward movement effect on melting of PCM in a double pipe heat exchanger. *Applied Mathematics and Computation*, 30-42.

Patil, A. (2020). *Experimental study of coil and shell phase change material heat exchanger* Dalhousie Univeristy. Halifax. 131.

Pielichowska, K., & Pielichowski, K. (2014). Phase change materials for thermal energy storage. *Progress in materials science*, 67-123.

Punniakodi, B. M. S., & Senthil, R. (2021). A review on container geometry and orientations of phase change materials for solar thermal systems. *Journal of Energy Storage*, 28.

Rathod, M., & Banerjee, J. (2014). Experimental investigations on latent heat storage unit using paraffin wax as phase change material. *Experimental heat transfer*, 40-55.

Raud, R., Cholette, M. E., Riahi, S., Bruno, F., Saman, W., Will, G., & Steinberg, T. A. (2017). Design optimization method for tube and fin latent heat thermal energy storage systems. *Energy*, 585-594.

Sadeghi, G. (2022). Energy storage on demand: Thermal energy storage development, materials, design, and integration challenges. *Energy Storage Materials*, 192-222.

Safari, V., Kamkari, B., & Abolghasemi, H. (2022). Investigation of the effects of shell geometry and tube eccentricity on thermal energy storage in shell and tube heat exchangers. *Journal of Energy Storage*, 18.

Seddegh, S., Wang, X., Joybari, M. M., & Haghighat, F. (2017). Investigation of the effect of geometric and operating parameters on thermal behavior of vertical shell-and-tube latent heat energy storage systems. *Energy*, 69-82.

Shamberger, P. J., & Bruno, N. M. (2020). Review of metallic phase change materials for high heat flux transient thermal management applications. *Applied Energy*, 28.

Shao, X., Yang, S., Fan, L., & Yuan, Y. (2023). Sugar alcohol phase change materials for low-to-medium temperature thermal energy storage: A comprehensive review. *Journal of Energy Storage*, 29.

Sharma, R., Sarı, A., Hekimoğlu, G. k., Zahir, M. H., & Tyagi, V. (2020). Effects of thermal cycling operation on solar thermal energy storage, morphology, chemical/crystalline structure, and thermal degradation properties of some fatty alcohols as organic PCMs. *Energy & Fuels*, 9011-9019.

Shen, G., Wang, X., Chan, A., Cao, F., & Yin, X. (2020). Investigation on optimal shell-to-tube radius ratio of a vertical shell-and-tube latent heat energy storage system. *Solar Energy*, 732-743.

Skaalum, J., & Groulx, D. (2020). Heat transfer comparison between branching and non-branching fins in a latent heat energy storage system. *International Journal of Thermal Sciences*, 10.

Tariq, S. L., Ali, H. M., Akram, M. A., & Janjua, M. M. (2020). Experimental investigation on graphene based nanoparticles enhanced phase change materials (GbNePCMs) for thermal management of electronic equipment. *Journal of Energy Storage*, 10.

Tatsidjodoung, P., Le Pierrès, N., & Luo, L. (2013). A review of potential materials for thermal energy storage in building applications. *Renewable and Sustainable Energy Reviews*, 327-349.

Tay, N., Belusko, M., & Bruno, F. (2012a). An effectiveness-NTU technique for characterising tube-in-tank phase change thermal energy storage systems. *Applied Energy*, 309-319.

Tay, N., Belusko, M., Castell, A., Cabeza, L. F., & Bruno, F. (2014). An effectiveness-NTU technique for characterising a finned tubes PCM system using a CFD model. *Applied Energy*, 377-385.

Tay, N., Bruno, F., & Belusko, M. (2012b). Experimental validation of a CFD model for tubes in a phase change thermal energy storage system. *International Journal of Heat and Mass Transfer*, 574-585.

Tomassetti, S., Aquilanti, A., Muciaccia, P. F., Coccia, G., Mankel, C., Koenders, E. A., & Di Nicola, G. (2022). A review on thermophysical properties and thermal stability of sugar alcohols as phase change materials. *Journal of Energy Storage*, 26.

Trevisan, S., Wang, W., Guedez, R., & Laumert, B. (2022). Experimental evaluation of an innovative radial-flow high-temperature packed bed thermal energy storage. *Applied Energy*, 17.

Vasu, A., Hagos, F. Y., Noor, M., Mamat, R., Azmi, W., Abdullah, A. A., & Ibrahim, T. K. (2017). Corrosion effect of phase change materials in solar thermal energy storage application. *Renewable and Sustainable Energy Reviews*, 19-33.

Wang, S., Lei, K., Wang, Z., Wang, H., & Zou, D. (2022). Metal-based phase change material (PCM) microcapsules/nanocapsules: Fabrication, thermophysical characterization and application. *Chemical Engineering Journal*, 21.

Wang, W.-W., Zhang, K., Wang, L.-B., & He, Y.-L. (2013). Numerical study of the heat charging and discharging characteristics of a shell-and-tube phase change heat storage unit. *Applied Thermal Engineering*, 542-553.

White, F. M., & Xue, H. (2021). *Fluid Mechanics* (9 ed.). McGraw-Hill Education. 1760.

Wołoszyn, J., Szopa, K., & Czerwiński, G. (2021). Enhanced heat transfer in a PCM shell-and-tube thermal energy storage system. *Applied Thermal Engineering*, 13.

Xiao, Q., Zhang, M., Fan, J., Li, L., Xu, T., & Yuan, W. (2019). Thermal conductivity enhancement of hydrated salt phase change materials employing copper foam as the supporting material. *Solar energy materials and solar cells*, 91-98.

Xu, H., Romagnoli, A., Sze, J. Y., & Py, X. (2017). Application of material assessment methodology in latent heat thermal energy storage for waste heat recovery. *Applied Energy*, 281-290.

Xu, T., Humire, E. N., Chiu, J. N., & Sawalha, S. (2021). Latent heat storage integration into heat pump based heating systems for energy-efficient load shifting. *Energy Conversion and Management*, 24.

Yan, S.-R., Fazilati, M. A., Samani, N., Ghasemi, H. R., Toghraie, D., Nguyen, Q., & Karimipour, A. (2020). Energy efficiency optimization of the waste heat recovery system with embedded phase change materials in greenhouses: a thermo-economic-environmental study. *Journal of Energy Storage*, 10.

Yang, X., Xiong, T., Dong, J. L., Li, W. X., & Wang, Y. (2017). Investigation of the dynamic melting process in a thermal energy storage unit using a helical coil heat exchanger. *Energies*, 18.

Yaws, C. L. (2003). Yaws' Handbook of Thermodynamic and Physical Properties of Chemical Compounds. In: Knovel.

Yuan, Y., Zhang, N., Tao, W., Cao, X., & He, Y. (2014). Fatty acids as phase change materials: a review. *Renewable and Sustainable Energy Reviews*, 482-498.

Zayed, M. E., Zhao, J., Li, W., Elsheikh, A. H., Elbanna, A. M., Jing, L., & Geweda, A. (2020). Recent progress in phase change materials storage containers: Geometries, design considerations and heat transfer improvement methods. *Journal of Energy Storage*, 22.

Zhang, Q., Yan, H., Zhang, Z., Luo, J., Yin, N., Tan, Z., & Shi, Q. (2021). Thermal analysis and heat capacity study of even-numbered fatty alcohol (C12H25OH-C18H37OH) phase-change materials for thermal energy storage applications. *Materials Today Sustainability*, 10.

Zivkovic, B., & Fujii, I. (2001). An analysis of isothermal phase change of phase change material within rectangular and cylindrical containers. *Solar Energy*, 51-61.

Appendix-A Engineering Drawings

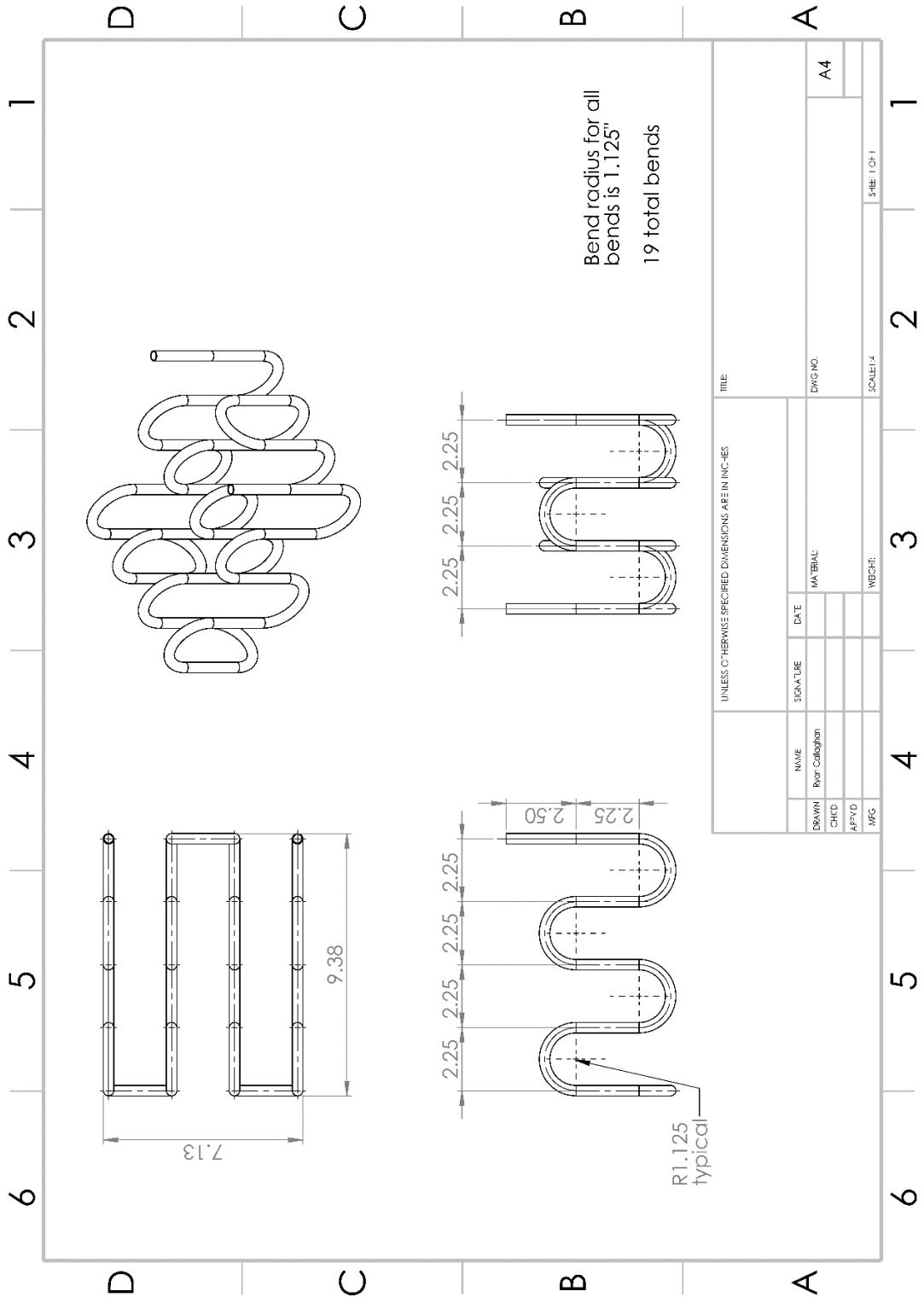

Figure A 1: Coil design

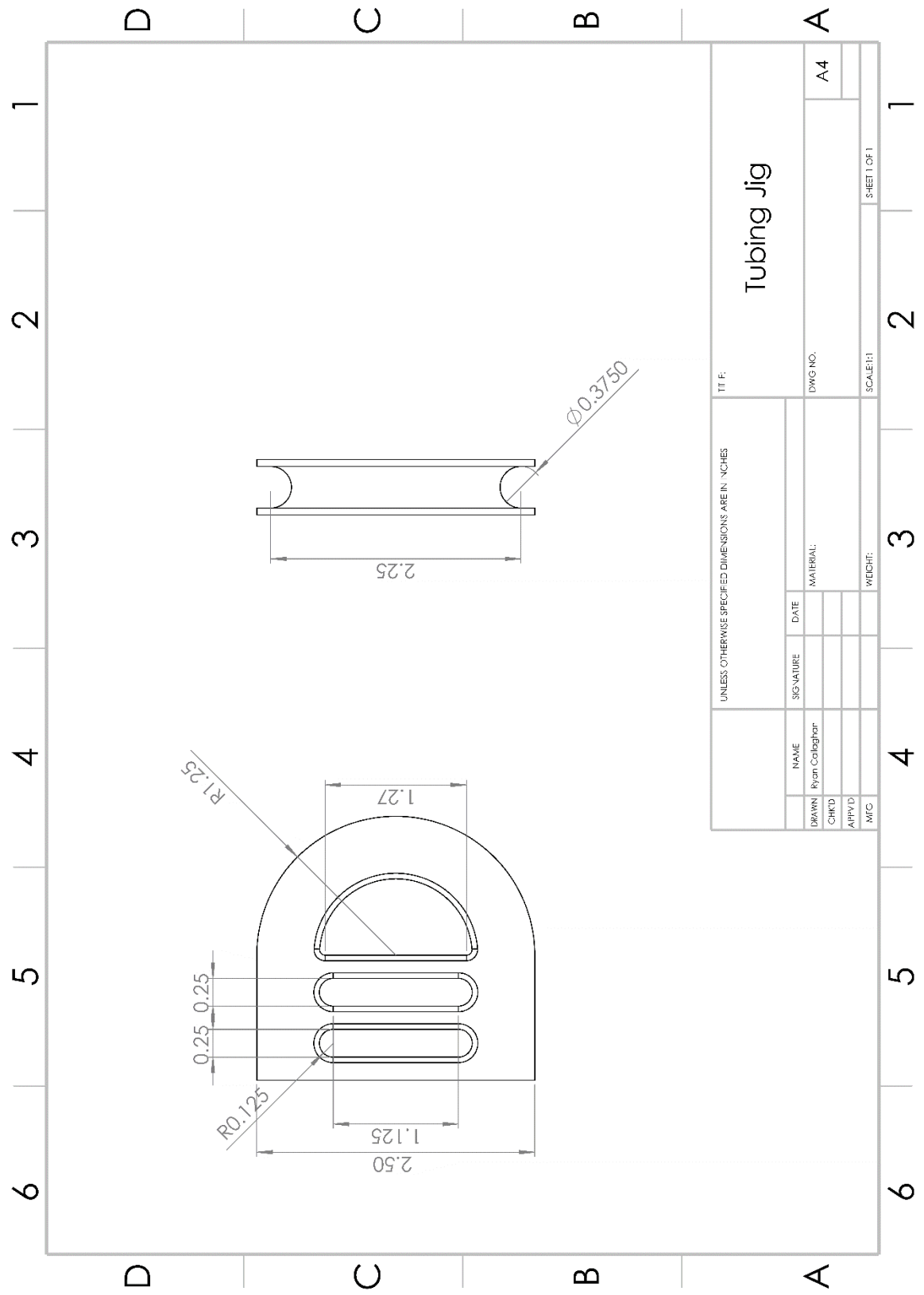

Figure A 2: Tube bending jig design

Appendix-B Equipment Data Sheets

PVC junction box specs

Molded nonmetallic boxes

6P rated

Nonmetallic junction boxes are UL Listed with a NEMA 6P rating per Section 314.29, Exception of the National Electrical Code® and CSA Certified per Section 12 of the Canadian Electrical Code. Manufactured from PVC or PPO thermoplastic molding compound and featuring foam in-place gasketed lids attached with stainless steel screws, these rugged enclosures offer all the corrosion resistance and physical properties you need for direct-burial applications.

Type 6P enclosures are intended for indoor or outdoor use, primarily to provide a degree of protection against contact with enclosed equipment, falling dirt, hose-directed water, entry of water during prolonged submersion at a limited depth and external ice formation.

Features and benefits:

- All Carlon junction boxes are UL Listed/CSA Certified and maintain a minimum of a NEMA Type 4/4X Rating

Diagrams

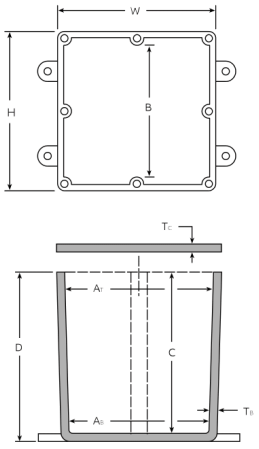

Molded nonmetallic junction boxes – 6P rated

E11461

Cat. No.	Size H x W x D (in.)	Std. Ctn.	Dimensions (in.) Min. AT	Min. AB	Min. B	Min. C	T_B	T_C	Material PVC	Thermo-plastic	Std. Wt(lb)
E989NNJ*	4 x 4 x 2	10	$3^{11}/_{16}$	$3^{5}/_{8}$	N/A	2	0.160	0.155	X		3
E987N*	4 x 4 x 4	10	$3^{11}/_{16}$	$3^{1}/_{2}$	N/A	4	0.160	0.155	X		4
E989NNR*	4 x 4 x 6	10	$3^{11}/_{16}$	$3^{3}/_{8}$	N/A	6	0.160	0.200	X		5
E989PPJ*	5 x 5 x 2	10	$4^{11}/_{16}$	$4^{1}/_{2}$	N/A	2	0.110	0.150		X	3
E987R-CAR*	6 x 6 x 4	2	6	$5^{5}/_{8}$	N/A	4	0.190	0.190		X	3
E989RRR-UPC*	6 x 6 x 6	8	$5^{5}/_{8}$	$5^{3}/_{8}$	N/A	6	0.160	0.150		X	14
E989N-CAR	8 x 8 x 4	1	8	8	N/A	4	0.185	0.190		X	2
E989SSX-UPC	8 x 8 x 7	2	$7^{21}/_{32}$	$7^{5}/_{16}$	N/A	7	0.160	0.150		X	6
E989UUN	12 x 12 x 4	3	$11^{5}/_{8}$	$11^{1}/_{2}$	$11^{1}/_{8}$	4	0.160	0.150		X	12
E989R-UPC	12 x 12 x 6	2	$11^{15}/_{16}$	$11^{7}/_{8}$	$11^{7}/_{16}$	6	0.265	0.185		X	10

* UL Listed

Vision
Turbine Flow Meters

Vision Turbine Meter

Models BV1000, BV2000 and BV3000

for Low Viscosity and Non-Aggressive Liquids NSF/ANSI/CAN 61 and 372 Certified

DESCRIPTION

The Vision Turbine Meters comply with the lead-free provisions of the Safe Drinking Water Act. Available models include meters that are:

- Bisphenol A (BPA)-free
- BV1000 and BV2000 certified to NSF/ANSI/CAN 61 and 372

The meters are designed for flow measurement of low-viscosity, aggressive and non-aggressive liquids alike, including demineralized water, alkaline solutions, oils, salad oil, fuel/fuel consumption, beverages, water solutions and coolants.

- The BV1000 flow range is 0.026….0.65 gpm (0.1…2.5 lpm)
- The BV2000 flow range 0.13…9.2 gpm (0.5…35 lpm)
- The BV3000 flow range 1.32…17.17 gpm (5…65 lpm)

The meter is especially suitable for washing machines, dishwashers, coffee machines, laser cooling plants, solar solutions, bakery machines, steam cooking machines in large kitchen plants, and CD or DVD cleaning.

APPLICATIONS

- **Food Industry:** Coffee machines, vending machines, dispensing systems, bakery machines, and steamers
- **Medical Applications:** Sterilizers, slide staining, dental water jets, and dialysis machines
- **Chemical and Pharma Industry:** Dosing systems and bottling plants
- **Industrial applications:** Cooling systems, washing machines and plants, dosing systems, water treatment units, filter monitoring systems, and solar plants
- **Automotive:** Fuel consumption measurement and fuel injection systems

FEATURES

- Compact size
- Measurement in any meter orientation
- Operating pressure up to 362.50 psi (25 bar)
- Temperature range of –4…212° F (–20…100° C)
- Accuracy of ± 3%
- Resolution up to 83,000 ppg (22,000 ppl), depending on the model

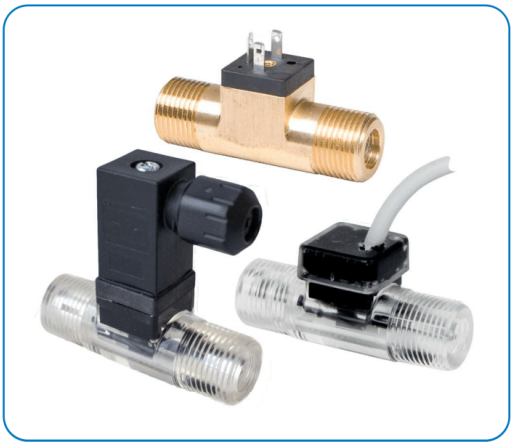

MEASURING PRINCIPLE

The rotor is turned by the liquid force proportional to flow. A Hall effect sensor supplies pulses that can be used for digital or analog signal processing. The generated pulses are specified as a K-factor.

OPERATING PRINCIPLE

Liquid flow causes a bladed turbine inside the meter housing to turn at an angular velocity directly proportional to the velocity of the liquid measured. As the blades pass beneath a magnetic pickup coil, a frequency signal is generated.

Each pulse is equivalent to a discrete volume of liquid. The frequency pulse is directly proportional to the turbine angular velocity and the flow rate.

The large number of pulses provides high resolution. As the mass of the turbine is small, the response time is fast. It is not necessary to install a straight length of pipeline upstream of the meter.

The simple mechanical construction of the Vision meter provides a long lifespan without any loss of accuracy. Pressure spikes less than the burst pressure rating do not affect the measurements.

Badger Meter

VIS-DS-00020-EN-13 (September 2021)

Product Data Sheet

SPECIFICATIONS

Model		BV1000	BV2000					BV3000
		025*	050	075	100	150	250	350	650
Flow Range		0.026…. 0.65 gpm	0.13… 1.3 gpm	0.13… 2.0 gpm	0.26… 2.7 gpm	0.26… 4.0 gpm	0.26… 6.6 gpm	0.53… 9.2 gpm	1.32…17.17 gpm
		0.1…2.5 lpm	0.5…5 lpm	0.5…7.5 lpm	1…10 lpm	1…15 lpm	1…25 lpm	2…35 lpm	5…65 lpm
K-factor		83,270 ppg	26100 ppg	17800 ppg	12500 ppg	8300 ppg	3785 ppg	2840 ppg	795 ppg
		22,000 ppl*	6900 ppl	4700 ppl	3300 ppl	2200 ppl	1000 ppl	750 ppl	210 ppl
DN mm		5 mm	6 mm	8 mm	6 mm	8 mm	8 mm	8 mm	12 mm
Operating Pressure		360 psi (25 bar)							—
Burst Pressure		2900 psi (200 bar)							~100 bar
Inlet / Outlet ports		1/4 in. NPT or G 1/4 in. (BSPP)	3/8 in. NPT or G 3/8 in. (BSPP)						3/4 in. NPT or G 3/4 in. (BSPP)
Operating Temperature		– 4…212° F (– 20…100° C)							
Accuracy		± 3% of reading							
Repeatability		< 0.50 % under the same operating conditions							
Viscosity		up to 16 cSt							
Electrical Connection		Round cable 3 x AWG 24 with free cable ends or *3-pin (2.8 × 0.5) mini DIN connector, EN 60529 * Mating connector is included.							
Filter		20…40 microns recommended							
Input Power		5…24V DC							
Power Consumption		~ 8 mA							
Output (Hz)		NPN sinking open collector							
Output Current		Max. 20 mA (Pull-up resistor required. See wiring diagram in User Manual.)							
Materials	Housing	Trogamid (NSF/ANSI/CAN 61 and 372 certified)							
		—	Brass CuZn38AI-C (complies with lead-free provisions of the Safe Drinking Water Act)						—
	Turbine	PPS Ferrite							
	Bearings	Graphite/PTFE							
Weight		~0.35 oz (10 g)	~ 0.53 oz (15 g)						~ 1.23 oz (35 g)
Approvals		KTW-BWGL; NSF/ANSI/CAN 61 and 372 for BV1000 and BV2000							
Certifications		RoHS and CE compliant							

* The previous generation of Model 025 had a K-factor of 18,500 ppl.

Pressure Drop Chart

	Type		Part Number															
	gpm	lpm	025		050		075		100		150		250		350		650	
	—	—	psi	bar	psi	bar	psi	bar	psi	bar	psi	bar	psi	bar	psi	bar	psi	bar
Pressure Drop Δp with Water Flow at 68° F (20° C)	**0.13**	**0.5**	0.29	0.02	—	—	—	—	—	—	—	—	—	—	—	—	—	—
	0.26	**1**	0.73	0.05	<0	<0	<0	<0	<0	<0	<0	<0	<0	<0	<0	<0	—	—
	0.40	**1.5**	2.18	0.15	—	—	—	—	—	—	—	—	—	—	—	—	—	—
	0.53	**2**	3.63*	0.25*	<0	<0	0.87	0.06	<0	<0	0.73	0.05	<0	<0	<0	<0	—	—
	1.32	**5**	—	—	1.74	0.12	2.90	0.20	0.73	0.05	2.90	0.20	0.73	0.05	0.73	0.05	0.00	0.00
	2.64	**10**	—	—	5.80	0.40	10.15	0.70	2.90	0.20	5.80	0.40	2.47	0.17	2.18	0.15	0.14	0.01
	3.96	**15**	—	—	13.05	0.90	—	—	5.80	0.40			3.92	0.27	3.63	0.25	0.29	0.02
	5.28	**20**	—	—	18.85	1.30	—	—	10.15	0.70	—	—	6.96	0.48	6.53	0.45	0.72	0.05
	6.60	**25**	—	—	—	—	—	—	—	—	—	—	9.43	0.65	8.70	0.60	1.02	0.07
	7.93	**30**	—	—	—	—	—	—	—	—	—	—	—	—	13.34	0.92	1.59	0.11
		35	—	—	—	—	—	—	—	—	—	—	—	—	—	—	2.03	0.14
		40	—	—	—	—	—	—	—	—	—	—	—	—	—	—	2.61	0.18
		45	—	—	—	—	—	—	—	—	—	—	—	—	—	—	3.34	0.23
		50	—	—	—	—	—	—	—	—	—	—	—	—	—	—	4.06	0.28
		55	—	—	—	—	—	—	—	—	—	—	—	—	—	—	4.93	0.34
		60	—	—	—	—	—	—	—	—	—	—	—	—	—	—	5.80	0.40
		65	—	—	—	—	—	—	—	—	—	—	—	—	—	—	6.82	0.47

*Value applies to 0.66 gpm (2.50 lpm)

CHEMICAL TRANSFER PUMPS

Little GIANT

MENU

5-MD SERIES - 1/8 HP

APPLICATIONS

The Little Giant MD series features leakproof, seal-less magnetic drives and are designed for in-line, non submersible use. Volute and magnet housing are glass-filled polypropylene for excellent chemical resistance. Impeller is glass-filled polypropylene and ceramagnet "A" (barium ferrite). Shaft and thrust washers are titanium for excellent wear and trouble-free service. Pumping heads are easily rotated, cleaned or serviced with no special tools required. Spindle shaft is supported at both ends to prevent impeller damage during start-up and stop of pump.

5-MD

1 ONE YEAR WARRANTY

FEATURES

- Thermally protected, open, fan-cooled permanent split capacitor motor
- Sleeve bearings
- 6' power cord with 3-prong plug (no plug on 230V)
- Specific gravity to 1.1
- Fluid temperature to 150°F
- Ambient air temperature to 77°F

NOTE: Consult your local distributor or the factory for applications with higher ambient temperatures, specific gravities and viscosities.

SERIES SPECIFICATIONS

Model No.	Item No.	Intake Size	Discharge Size	Listing(s)	HP	Volts	Hertz	Amps	Watts	Performance (GPM@Head)					Shutoff		Power Cord (ft.)	Weight (lbs.)
										1'	3'	6'	9'	15'	Ft.	P.S.I.		
5-MD	583002	1/2" FNPT	1/2" MNPT	UR/C-CSA	1/8	115	60	2.1	200	905	875	800	750	635	34.6	15.0	6	9.25

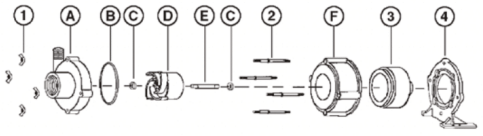

REPLACEMENT PARTS

Item	Part No.	Description
A	183070	Volute
B	924007	O-ring
C	921067	Thrust washer
D	183142	Impeller
E	182056	Shaft
F	182005	Housing
1	920003	Wing nut
2	911403	Stud, collared
3	182602	Drive magnet
4	180031	Mounting bracket

NOTE: Parts A–F contact fluid

5-MD SERIES - 1/8 HP

ENGINEERING DATA

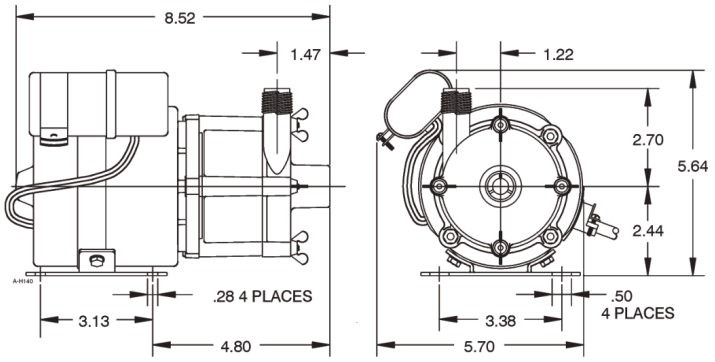

NOTE: Designs and dimensions may vary for various reasons (i.e. type of motor). This information should be used as general guide rather than an unqualified guarantee. Specifications are subject to change without prior notice.

PERFORMANCE DATA

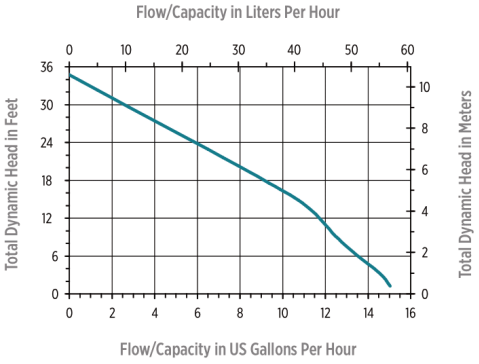

T **Duplex Insulated Copper-Constantan Duplex ANSI Type T**

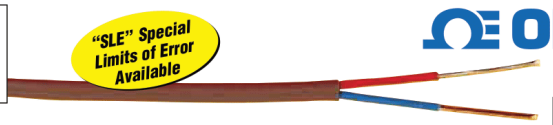

OMEGA®

ANSI color code shown | **To order IEC color code visit us online**

ANSI Color Code: Positive Wire, Blue; Negative Wire, Red; Overall, Brown
OMEGA Engineering does not use reprocessed PFA or PVC in manufacturing thermocouple wire.

To order

Insulation	AWG No.	Model Number	Type Wire	Insulation		Max Temp		Nominal Size mm (inches)	Wt.† kg/300 m (lb/1000')
				Conductor	Overall	°C	°F		
Glass	20	**GG-T-20**	Solid	Glass Braid	Glass Braid	260	500	1.5 x 2.4 (0.060 x 0.095)	4 (9)
	20	**GG-T-20S**	7 x 28	Glass Braid		260	500	1.5 x 2.5 (0.060 x 0.100)	4 (9)
	24	**GG-T-24**	Solid	Glass Braid		200	400	1.3 x 2.0 (0.050 x 0.080)	3 (5)
	24	**GG-T-24S**	7 x 32	Glass Braid		200	400	1.3 x 2.2 (0.050 x 0.085)	3 (5)
	26	**GG-T-26**	Solid	Glass Wrap		200	400	1.1 x 1.9 (0.045 x 0.075)	2 (4)
	28	**GG-T-28**	Solid	Glass Wrap		200	400	1.0 x 1.4 (0.040 x 0.055)	2 (3)
	30	**GG-T-30**	Solid	Glass Wrap		150	300	0.9 x 1.3 (0.037 x 0.050)	2 (3)
Glass with Stainless Steel Overbraid	20	**GG-T-20-SB**	Solid	Glass	SS Braid Over Glass	260	500	2.2 x 3.0 (0.090 x 0.120)	6 (14)
	20S	**GG-T-20S-SB**	Solid			260	500	2.2 x 3.0 (0.085 x 0.117)	5 (11)
	24	**GG-T-24-SB**	Solid			200	400	2.2 x 3.0 (0.085 x 0.117)	5 (11)
	24S	**GG-T-24S-SB**	Solid			200	400	2.2 x 3.0 (0.085 x 0.117)	5 (11)
Kapton Polymide Tape	20	**KK-T-20**	Solid	Fused Polymide Tape	Fused Polymide Tape	260	500	1.5 x 2.5 (0.060 x 0.100)	5 (11)
	24	**KK-T-24**	Solid			260	500	1.3 x 1.9 (0.050 x 0.075)	3 (6)
	30	**KK-T-30**	Solid			260	500	1.0 x 1.4 (0.040 x 0.055)	3 (5)
PFA Glass	30	**TG-T-30**	Solid	PFA	Glass Braid	150	300	0.9 x 1.2 (0.034 x 0.047)	1 (2)
	36	**TG-T-36**	Solid			150	300	0.7 x 1.0 (0.028 x 0.038)	1 (2)
	40	**TG-T-40**	Solid			150	300	0.7 x 0.9 (0.026 x 0.035)	1 (2)
Neoflon PFA (High Performance)	20	**TT-T-20**	Solid	PFA	PFA	260	500	1.7 x 3.0 (0.068 x 0.116)	5 (11)
	20	**TT-T-20S**	7 x 28			260	500	1.9 x 3.2 (0.073 x 0.126)	5 (11)
	22	**TT-T-22S**	7 x 30			260	500	1.7 x 3.4 (0.065 x 0.133)	4 (9)
	24	**TT-T-24**	Solid			200	400	1.4 x 2.4 (0.056 x 0.092)	3 (7)
	24	**TT-T-24S**	7 x 32			200	400	1.6 x 2.6 (0.063 x 0.102)	3 (7)
	30	**TT-T-30††**	Solid			150	300	0.6 x 1.0 (0.024 x 0.040)	1 (2)
	36	**TT-T-36††**	Solid			150	300	0.5 x 0.8 (0.019 x 0.030)	1 (2)
	40	**TT-T-40††**	Solid			150	300	0.4 x 0.7 (0.017 x 0.026)	1 (2)
PFA Polymer w/Twisted and Shielded Conductors	20	**TT-T-20-TWSH**	Solid	PFA Polymer	PFA Polymer and Shielding	260	500	3.7 (0.15)	9 (20)
	20S	**TT-T-20S-TWSH**	7 x 28			260	500	3.8 (0.15)	9 (20)
	24	**TT-T-24-TWSH**	Solid			260	500	2.7 (0.11)	4 (9)
	24S	**TT-T-24S-TWSH**	7 x 32			260	500	2.9 (0.12)	4 (9)
Neoflon FEP	20	**FF-T-20**	Solid	FEP	FEP	200	392	1.7 x 3.0 (0.068 x 0.116)	5 (11)
	24	**FF-T-24**	Solid			200	392	1.4 x 2.4 (0.056 x 0.092)	3 (7)
FEP Polymer w/Twisted and Shielded Conductors	20	**FF-T-20-TWSH**	Solid	FEP Polymer	FEP Polymer and Shielding	200	392	3.7 (0.15)	9 (20)
	20S	**FF-T-20S-TWSH**	7 x 28			200	392	3.8 (0.15)	9 (20)
	24	**FF-T-24-TWSH**	Solid			200	392	2.7 (0.11)	4 (9)
	24S	**FF-T-24S-TWSH**	7 x 32			200	392	2.9 (0.12)	4 (9)
TFE Tape Polymer	20	**TFE-T-20**	Solid	TFE Tape Polymer	Fused TFE Tape Polymer	260	500	1.5 x 2.5 (0.060 x 0.100)	5 (11)
	20S	**TFE-T-20S**	7 x 28			260	500	1.5 x 2.7 (0.060 x 0.105)	5 (11)
	24	**TFE-T-24**	Solid			260	500	1.3 x 1.9 (0.050 x 0.075)	3 (6)
	24S	**TFE-T-24S**	7 x 32			260	500	1.3 x 2.2 (0.050 x 0.085)	3 (6)
Polyvinyl	24	**PP-T-24**	Solid	Polyvinyl	Polyvinyl	105	221	1.9 x 3 (0.075 x 0.120)	5 (10)
	24	**PP-T-24S**	7 x 32			105	221	1.9 x 3.1 (0.080 x 0.130)	5 (10)
	24	**PR-T-24**	Solid		(Rip Cord)**	105	221	1.3 x 2.2 (0.050 x 0.086)	3 (5)

See Fused Tape Insulated TFE-T Series.
*** Two insulated leads bonded together, but with no overjacket.*
† Weight of spool and wire rounded to the next highest lb. (does not include packing material).
*†† Overall color clear, ††† To order special limits of error wire, add **"-SLE"** to model number before spool length.*
***Ordering Example: TT-T-24-SLE-1000,** 1000' (300 m) of Type T duplex insulated special limits of error thermocouple wire.*

Discount Schedule *(1000' spools only)*

3 to 4 spools	10%
5 to 9 spools	15%
10 to 19 spools	20%

Note: Published prices are based on market value at time of printing and are subject to change due to Nickel surcharges, Chromium and precious-metal market fluctuations.

Compact Transition Joint Probes

OMEGA®

Where Space is Limited PFA Insulated Lead Wire

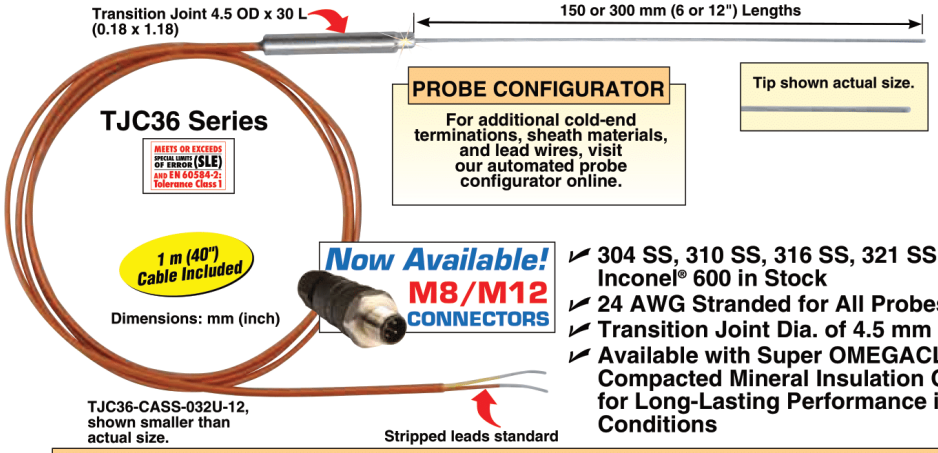

- 304 SS, 310 SS, 316 SS, 321 SS and Inconel® 600 in Stock
- 24 AWG Stranded for All Probes
- Transition Joint Dia. of 4.5 mm (0.177")
- Available with Super OMEGACLAD® XL Compacted Mineral Insulation Cable for Long-Lasting Performance in Harsh Conditions

To Order

Calibration ANSI Code	Sheath Material	Sheath Dia. mm (in)	Upper Temp Guidelines °C (°F) T/C Junction	Model No. *Specify Junction (G)rounded, (E)xposed, or (U)ngrounded. **Probe Length 150 mm (6"), 300 mm (12"), 450 mm (18") in Stock
K CHROMEGA®-ALOMEGA®	304 SS	0.25 (0.010)	500 (932)	TJC36-CASS-010(*)-(**)
	304 SS	0.50 (0.020)	700 (1290)	TJC36-CASS-020(*)-(**)
	304 SS	0.80 (0.032)	700 (1290)	TJC36-CASS-032(*)-(**)
	304 SS	1.00 (0.040)	700 (1290)	TJC36-CASS-040(*)-(**)
	304 SS	1.59 (0.062)	900 (1652)	TJC36-CASS-062(*)-(**)
	INC 600	0.25 (0.010)	500 (932)	TJC36-CAIN-010(*)-(**)
	INC 600	0.50 (0.020)	700 (1290)	TJC36-CAIN-020(*)-(**)
	INC 600	0.80 (0.032)	700 (1290)	TJC36-CAIN-032(*)-(**)
	INC 600	1.00 (0.040)	700 (1290)	TJC36-CAIN-040(*)-(**)
	INC 600	1.59 (0.062)	920 (1690)	TJC36-CAIN-062(*)-(**)
	XL	0.25 (0.010)	600 (1112)	TJC36-CAXL-010(*)-(**)
	XL	0.50 (0.020)	800 (1472)	TJC36-CAXL-020(*)-(**)
	XL	0.80 (0.032)	800 (1472)	TJC36-CAXL-032(*)-(**)
	XL	1.00 (0.040)	800 (1472)	TJC36-CAXL-040(*)-(**)
	XL	1.59 (0.062)	1038 (1900)	TJC36-CAXL-062(*)-(**)
J IRON-CONSTANTAN	304 SS	0.25 (0.010)	260 (500)	TJC36-ICSS-010(*)-(**)
	304 SS	0.50 (0.020)	260 (500)	TJC36-ICSS-020(*)-(**)
	304 SS	0.80 (0.032)	260 (500)	TJC36-ICSS-032(*)-(**)
	304 SS	1.00 (0.040)	260 (500)	TJC36-ICSS-040(*)-(**)
	304 SS	1.59 (0.062)	440 (825)	TJC36-ICSS-062(*)-(**)
T COPPER-CONSTANTAN	304 SS	0.50 (0.020)	260 (500)	TJC36-CPSS-020(*)-(**)
	304 SS	0.80 (0.032)	260 (500)	TJC36-CPSS-032(*)-(**)
	304 SS	1.00 (0.040)	260 (500)	TJC36-CPSS-040(*)-(**)
	304 SS	1.59 (0.062)	260 (500)	TJC36-CPSS-062(*)-(**)

** Specify junction type: **E** (Exposed), **G** (Grounded) or **U** (Ungrounded). ** Specify length in inches, plus additional price for length. Custom lengths also available; use additional price for length in 150 mm/6" increments.*

*For a male straight M8 plug add **"M8-S-M"** to the model number for additional cost, for a male straight M12 plug add **"M12-S-M"** to the model number for additional cost. For a male right-angled M8 plug add **"M8-R-M"** to the model number for additional cost, for a male right-angled M12 plug add **"M12-S-M"** to the model number for additional cost.*

***Ordering Example: TJC36-CASS-020G-6,** compact transition joint probe, 40" cable, Type K, 0.020" OD stainless steel sheath, 6" length, grounded junction.*

RTD Probes with M12 Molded Connectors

Standard and Metric Sizes

PR-22 Series

ACCURACY IEC CLASS A (±0.15°C @ 0°C)
ACCURACY IEC CLASS B (±0.30°C @ 0°C)

- -30 to 350°C (-22 to 622°F) Probe Temperature Range (Class A) Standard, -50 to 500°C (-58 to 932°F) (Class B)
- -50 to 90°C (-58 to 194°F) Connector Temperature Range
- 316 Stainless Steel Probe in Imperial and Metric Diameters
- Many Standard Lengths Available
- IP67 Molded 4-Pin M12 Connector

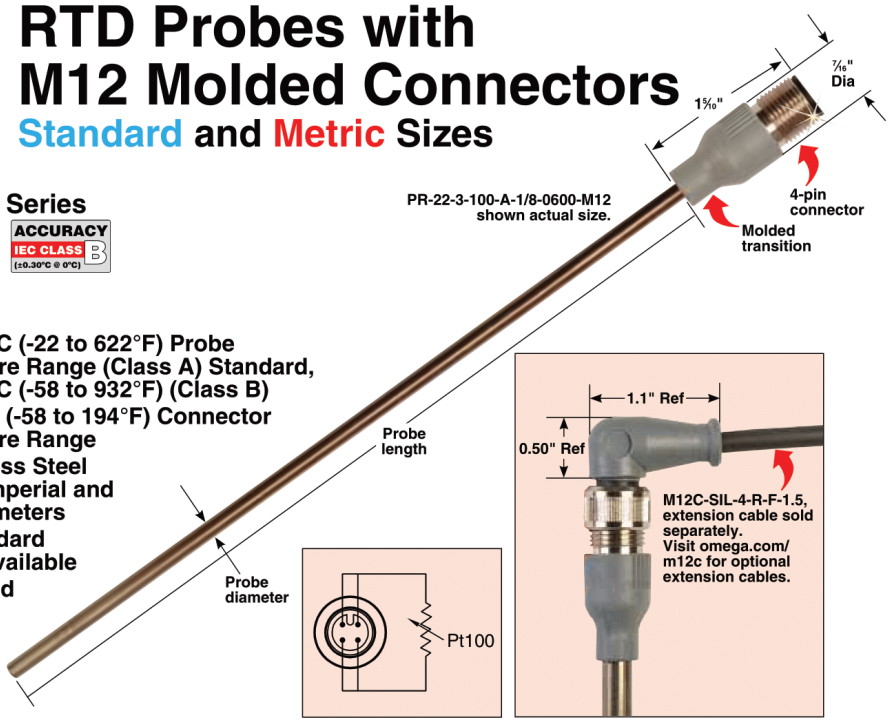

Standard

To Order *Visit omega.com/pr-22 for Pricing and Details*		
Model Number	**Probe Length**	**Element Specification**
PR-22-3-100-A-(*)-0600-M12	6"	Pt100, Class A
PR-22-3-100-A-(*)-0900-M12	9"	Pt100, Class A
PR-22-3-100-A-(*)-1200-M12	12"	Pt100, Class A
PR-22-3-100-A-(*)-1800-M12	18"	Pt100, Class A
PR-22-3-100-A-(*)-2400-M12	24"	Pt100, Class A

(*) *= Insert probe diameter of ⅛ of ¼ inches.*
For Class B, change ***"-A"*** *in model number to* ***"-B"*** *and visit omega.com/pr-22 for pricing.*
Ordering Examples: PR-22-3-100-A-1/8-0600-M12, *⅛" diameter by 6" long Pt100 Class A RTD sensor with molded M12 connector.*
PR-22-3-100-A-1/4-1200-M12, *¼" diameter by 12" long Pt100 Class A RTD sensor with molded M12 connector.*

Metric

Model Number	Probe Length	Element Specification
PR-22-3-100-A-(*)-100-M12	100 mm	Pt100, Class A
PR-22-3-100-A-(*)-150-M12	150 mm	Pt100, Class A
PR-22-3-100-A-(*)-250-M12	250 mm	Pt100, Class A
PR-22-3-100-A-(*)-350-M12	350 mm	Pt100, Class A
PR-22-3-100-A-(*)-500-M12	500 mm	Pt100, Class A
PR-22-3-100-A-(*)-750-M12	750 mm	Pt100, Class A
PR-22-3-100-A-(*)-1000-M12	1000 mm	Pt100, Class A

(*) *= Insert probe diameter of* ***"M2", "M3"*** *or* ***"M6"*** *for 2 mm, 3 mm or 6 mm probe diameters shown in table. (M2 only available in 150 mm and 250 mm lengths.*
For Class B, change ***"-A"*** *in model number to* ***"-B"*** *and visit omega.com/pr-22 for pricing.*
Ordering Examples: PR-22-3-100-A-M3-250-M12, *3 mm diameter by 250 mm long Pt100 Class A RTD sensor with molded M12 connector.*
PR-22-3-100-A-M6-500-M12, *6 mm diameter by 500 mm long Pt100 Class A RTD sensor with molded M12 connector.*

15 Liter Refrigerated Circulator, -30°C

SD15R-30

Key Specifications

Description	-30, 15 L Ref. Circulator
Controller Type	Standard Digital
Display	3.75" Touch-Pad LCD
Connectivity	RS232
Swivel 180 Rotating Controller	Yes
Working Temperature Range °C	-30° to 170°
Temperature Stability °C	±0.04°
Fluid Optimization/Specific Heat Tuning	Automatic
Temperature Calibration Capability	1-point
Working Access (L x W x D) (cm)	21.2 x 27.6 x 14 cm
Pump Type	Pressure
Flammability Class (DIN 12876-1)	I (NFL)
Electrical Plug Options	Part numbers listed are Standard U.S. and European types. Country specific plug types available. Contact your regional distributor to order.

Key Features

Standard Digital Controller

Key Features

- Large, universal icon and English display
- Swivel 180™ Rotating Controller
- On-board connectivity: RS-232 serial output
- On-screen prompts
- Automatic performance optimization
- Single-point calibration capability

Common Specifications

Working Temperature Range °F	-22° to 338°
Working Temperature Range °C	-30° to 170°
Nominal Cooling Capacity @ +20C (W)	915
Reservoir Capacity (gallons)	3.96
Reservoir Capacity (liters)	15
Reservoir/Tank Material	Stainless Steel
Reservoir Cover	Included
DuraTop	Yes
LidDock	Yes
Cleanable Air Filter	Yes
Working Access (L x W x D) (inches)	8.35 x 10.88 x 5.5 in
Working Access (L x W x D) (cm)	21.2 x 27.6 x 14 cm
Temperature Stability °F	±0.08°
Temperature Stability °C	±0.04°
Display	3.75" Touch-Pad LCD
Display Resolution (Set)	0.1
Display Resolution (Read)	0.1
Pump Type	Pressure
Pump Speed	Two
Process Connections	1/4" (F) NPT
Flammability Class (DIN 12876-1)	I (NFL)
Over-Temperature Protection / Failsafe Heater Control	Yes
Low Liquid Level Protection	Yes
WhisperCool Environmental Control Technology	Yes
Cool Command Refrigeration Technology	Yes
Reservoir Drain	Yes

Maximum Ambient Temperature °F	95°
Maximum Ambient Temperature °C	35°
Overall Dimensions (L x W x H) (inches)	22.4 x 14.5 x 26.9 in
Overall Dimensions (L x W x H) (cm)	56.9 x 36.8 x 68.3 cm
Refrigerant	R404A
Environmental Compliance	RoHS, WEEE
Shipping Weight (pounds)	118.0
Shipping Weight (kilograms)	53.5
Catalog Page Number	42-43

60 Hz Only

Part Number	SD15R-30-A11B
Maximum Pressure (psi)	3.5
Maximum Pressure (bar)	0.24
Maximum Pressure Flow Rate (gpm)	2.90
Maximum Pressure Flow Rate (l/min)	11.0
Cooling Capacity @ -20°C (W)	165
Cooling Capacity @ 0°C (W)	505
Cooling Capacity @ +20°C (W)	915
Cooling Capacity @ +100°C (W)	915
Included Hardware	Nylon hose adapters for 3/8", 1/4", and 3/16"
Heater Wattage	1100
Electrical Requirements (VAC/Hz/Ph/A)	120/60/1/13
Regulatory Approvals	ETL

50 Hz Only

Part Number	SD15R-30-A12E
Maximum Pressure (psi)	2.9
Maximum Pressure (bar)	0.20
Maximum Pressure Flow Rate (gpm)	2.70
Maximum Pressure Flow Rate (l/min)	10.2
Cooling Capacity @ -20°C (W)	165
Cooling Capacity @ 0°C (W)	505
Cooling Capacity @ +20°C (W)	915
Cooling Capacity @ +100°C (W)	915
Included Hardware	Nylon hose adapters for 3/8", 1/4", and 3/16", and 1/4" NPT to M16 adapter
Heater Wattage	2200
Electrical Requirements (VAC/Hz/Ph/A)	240/50/1/13

Foam insulation specs

FOAMULAR NGX C-200 XPS Rigid Foam Insulation Board; 1/2-inch x 24-inch x 96-inch R-2.5 Butt Edge

FOAMULAR® NGX Extruded Polystyrene Rigid Insulation, is a moisture-resistant, rigid foam insulation, which can be installed on the interior or exterior of walls, foundation walls and under concrete floor slabs. With a thermal resistance of R-5 per inch of thickness, it can reduce heating and cooling costs and increase the home's comfort. Lightweight, durable and impact-resistant, FOAMULAR® NGX products are easy to handle and install, and made in Canada. Choose FOAMULAR® NGX Rigid Insulation for your next renovation.

- Used for above/below grade exterior walls, basement walls or basement floor slab (20 psi)
- Excellent energy efficiency in the form of a high R-5 per inch; available in a wide choice of sizes, thicknesses and edges
- Lightweight, durable and moisture-resistant
- Easy to cut, score and install
- Only XPS with a limited lifetime warranty that guarantees a minimum 90% of R-value for the life of the product; see warranty for complete details.
- GREENGUARD Gold certified; contributes to indoor air quality and certified by Scientific Certification Systems (SCS) to contain a minimum of 20% recycled content. Made with 100% renewable electricity, through power purchase agreements.

Details

Certified	✓	**Country of Origin**	CA-Canada
Coverage Area (sq. ft.)	16	**Faced or Unfaced**	Unfaced
Insulation Wall Size	2 x 6 Walls	**Product Length (ft.)**	8
R Value	5	**Sheathing Type**	XPS
Sound Barrier	✓		

Specifications

Dimensions

Assembled Depth (in inches)	24	**Assembled Height (in inches)**	0.5
Assembled Weight (in lbs)	1.26	**Assembled Width (in inches)**	96
Packaged Depth (in inches)	96	**Packaged Height (in inches)**	0.5
Packaged Weight (In lbs)	0.14	**Packaged Width (in inches)**	24

Foil insulation specs

Overview

Model # DW12025 Store SKU # 1000167782

Reflectix Duct Insulation consists of two outer layers of aluminum foil that reflect 97% of radiant heat. Each layer of foil is bonded to a tough layer of polyethylene for strength. Two inner layers of insulating bubbles resist conductive heat flow while a center layer of polyethylene gives Reflectix high reliability and strength. Reflectix Duct Insulation may be installed by wrapping rectangular or round ductwork in HVAC applications and has an R-Value of R-6 with an airspace. Heating costs can be greatly reduced. Eliminate unnecessary heat loss/gain and air leakage. Helps to ensure consistent temperatures.

- An R-4.2 results when installed directly to the duct
- Inhibits condensation
- Installs clean and no itchy fibers
- Only basic tools are required; scissors/utility knife, tape measure and safety glasses
- Class A/Class 1 fire rating
- No nesting characteristics for birds, insects or rodents

Details

Country of Origin	US-United States	**Coverage Area (sq. ft.)**	25
Product Length (ft.)	25	**R Value**	4
Roll Length (ft.)	25	**Roll Width**	12
Sound Barrier	No	**Type**	Roll

Specifications

Dimensions

Assembled Depth (in inches)	11	**Assembled Height (in inches)**	12
Assembled Weight (in lbs)	1.56	**Assembled Width (in inches)**	11
Packaged Depth (in inches)	11	**Packaged Height (in inches)**	12
Packaged Weight (In lbs)	1.5	**Packaged Width (in inches)**	11

FIBERGLAS insulation specs

Overview

Model # 657368 Store SKU # 1000789365

Help keep your home warm in the winter and cool in the summer with EcoTouch PINK FIBERGLAS insulation from Owens Corning; providing a comfortable home and can save you money on heating and cooling costs*. The friction fit batts are easy to install and available in a full range of R-values, offering outstanding thermal and noise control solutions for every project. From the attic overhead, to the basement below, and the walls in between for new construction or adding to your existing insulation, there's an Owens Corning PINK insulation comfort solution for every part of the home.

- For 2" x 4" walls
- Outstanding thermal performance
- Save on your heating and cooling costs*
- Safe for your home; non-combustible
- Friction fit batts easy to install
- Made in Canada with a 73% recycled glass content, SCS Certified and GREENGUARD Gold certified for indoor air quality, and validated to be formaldehyde free
- Price and product availability may vary across markets and stores

Details

Certified	✓	**Colour Family**	Pink
Country of Origin	CA-Canada	**Coverage Area (sq. ft.)**	40
Faced or Unfaced	Unfaced	**Insulation Wall Size**	2 x 4 Walls
Product Length (ft.)	32	**R Value**	12
Roll or Batt	Batt	**Sound Barrier**	✓

Specifications

Dimensions

Assembled Depth (in inches)	19	**Assembled Height (in inches)**	15
Assembled Weight (in lbs)	7.68	**Assembled Width (in inches)**	19
Packaged Depth (in inches)	15	**Packaged Height (in inches)**	15
Packaged Weight (In lbs)	9.69	**Packaged Width (in inches)**	19

Specifications

Table 1. Specifications

Range	–5 °C to 125 °C (23 °F to 257 °F)
Accuracy	±0.25 °C
Stability	±0.015 °C at –5 °C (oil, 5010) ±0.03 °C at 121 °C (oil, 5010)
Uniformity	±0.02 °C
Resolution	0.01 °C/F
Operating Temperature	5 °C to 45 °C (41 °F to 113 °F)
Heating Time	25 °C to 100 °C (77 °F to 212 °F): 30 minutes
Cooling Time	25 °C to 0 °C (77 °F to 32 °F): 30 minutes
Well Size	64 x 139 mm deep (2.5 in dia. x 5.5 in) (access opening is 48 mm [1.9 in] in diameter)
Exterior Dimension	31 cm x 18 cm x 24 cm (12 in H x 7.2 in W x 9.5 in D)
Weight	6.8 kg (15 lb) with fluid
Power	115/230 VAC (±10 %), 50/60 Hz, 300 VA
Fuse Rating	T, 4 A, 250 V
Readout	Switchable °C or °F
Controller	Digital controller with data retention
Thermal Electric Devices (TED)	150 W
Cooling	Fan and Thermal Electric Devices (TED)
Environmental Conditions	
Ambient Temperature Range	5 °C to 45 °C (41 °F to 113 °F)
Ambient Relative Humidity	maximum 80 % for temperature <31 °C, decreasing linearly to 35 % at 45 °C
Altitude	<2000 m
Fault Protection	Sensor burnout and short protection
Safety **General** **Heating**	 IEC 61010-1: Overvoltage Category II, Pollution Degree 2 IEC 61010-2-010
Electromagnetic Compatibility (EMC)	International.....IEC 61326-1: Basic Electromagnetic Environment CISPR 11: Group 1, Class A *Group 1: Equipment has intentionally generated and/or uses conductively-coupled radio frequency energy that is necessary for the internal function of the equipment itself. Class A: Equipment is suitable for use in all establishments other than domestic and those directly connected to a low-voltage power supply network that supplies buildings used for domestic purposes. There may be potential difficulties in ensuring electromagnetic compatibility in other environments due to conducted and radiated disturbances. Caution: This equipment is not intended for use in residential environments and may not provide adequate protection to radio reception in such environments.* Korea (KCC).....Class A Equipment (Industrial, Broadcasting, & Communication Equipment) *Class A: Equipment meets requirements for industrial electromagnetic wave equipment and the seller or user should take notice of it. This equipment is intended for use in business environments and not to be used in homes.* USA (FCC) .....47 CFR 15 subpart B. This product is considered an exempt device per clause 15.10

Appendix-C Copyright License

ELSEVIER LICENSE
TERMS AND CONDITIONS

Dec 13, 2023

This Agreement between Dalhousie University -- Ryan Callaghan ("You") and Elsevier ("Elsevier") consists of your license details and the terms and conditions provided by Elsevier and Copyright Clearance Center.

License Number	5687140214921
License date	Dec 13, 2023
Licensed Content Publisher	Elsevier
Licensed Content Publication	Applied Energy
Licensed Content Title	An effectiveness-NTU model of a packed bed PCM thermal storage system
Licensed Content Author	N.A.M. Amin,M. Belusko,F. Bruno
Licensed Content Date	Dec 1, 2014
Licensed Content Volume	134
Licensed Content Issue	n/a
Licensed Content Pages	7
Start Page	356
End Page	362

Type of Use	reuse in a thesis/dissertation
Portion	figures/tables/illustrations
Number of figures/tables/illustrations	1
Format	electronic
Are you the author of this Elsevier article?	No
Will you be translating?	No
Title of new work	EFFECT OF PCM SELECTION ON THE THERMAL PERFORMANCE OF A COIL-IN-SHELL STORAGE SYSTEM
Institution name	Dalhousie University
Expected presentation date	Dec 2023
Portions	figure 1 page 358
Requestor Location	Dalhousie University 5885 Spring Garden Road Apt. 1016 Halifax, NS B3H 1Y3 Canada Attn: Dalhousie University
Publisher Tax ID	GB 494 6272 12
Total	0.00 CAD
Terms and Conditions	

INTRODUCTION

ELSEVIER LICENSE
TERMS AND CONDITIONS

Dec 09, 2023

This Agreement between Dalhousie University -- Ryan Callaghan ("You") and Elsevier ("Elsevier") consists of your license details and the terms and conditions provided by Elsevier and Copyright Clearance Center.

License Number	5685001277960
License date	Dec 09, 2023
Licensed Content Publisher	Elsevier
Licensed Content Publication	Solar Energy Materials and Solar Cells
Licensed Content Title	Fatty acids and related phase change materials for reliable thermal energy storage at moderate temperatures
Licensed Content Author	Samer Kahwaji,Michel B. Johnson,Ali C. Kheirabadi,Dominic Groulx,Mary Anne White
Licensed Content Date	Aug 1, 2017
Licensed Content Volume	167
Licensed Content Issue	n/a
Licensed Content Pages	12
Start Page	109
End Page	120

Type of Use	reuse in a thesis/dissertation
Portion	figures/tables/illustrations
Number of figures/tables/illustrations	2
Format	both print and electronic
Are you the author of this Elsevier article?	No
Will you be translating?	No
Title of new work	EFFECT OF PCM SELECTION ON THE THERMAL PERFORMANCE OF A COIL-IN-SHELL STORAGE SYSTEM
Institution name	Dalhousie University
Expected presentation date	Dec 2023
Portions	Figure 2 on page 112
Requestor Location	Dalhousie University 5885 Spring Garden Road Apt. 1016 Halifax, NS B3H 1Y3 Canada Attn: Dalhousie University
Publisher Tax ID	GB 494 6272 12
Total	0.00 CAD
Terms and Conditions	

INTRODUCTION

ELSEVIER LICENSE
TERMS AND CONDITIONS

Dec 13, 2023

This Agreement between Dalhousie University -- Ryan Callaghan ("You") and Elsevier ("Elsevier") consists of your license details and the terms and conditions provided by Elsevier and Copyright Clearance Center.

License Number	5687131138505
License date	Dec 13, 2023
Licensed Content Publisher	Elsevier
Licensed Content Publication	Energy Conversion and Management
Licensed Content Title	Enhance heat transfer for PCM melting in triplex tube with internal–external fins
Licensed Content Author	Sohif Mat,Abduljalil A. Al-Abidi,K. Sopian,M.Y. Sulaiman,Abdulrahman Th Mohammad
Licensed Content Date	Oct 1, 2013
Licensed Content Volume	74
Licensed Content Issue	n/a
Licensed Content Pages	14
Start Page	223
End Page	236

Type of Use	reuse in a thesis/dissertation
Portion	figures/tables/illustrations
Number of figures/tables/illustrations	1
Format	electronic
Are you the author of this Elsevier article?	No
Will you be translating?	No
Title of new work	EFFECT OF PCM SELECTION ON THE THERMAL PERFORMANCE OF A COIL-IN-SHELL STORAGE SYSTEM
Institution name	Dalhousie University
Expected presentation date	Dec 2023
Portions	figure 1 page 224
Requestor Location	Dalhousie University 5885 Spring Garden Road Apt. 1016 Halifax, NS B3H 1Y3 Canada Attn: Dalhousie University
Publisher Tax ID	GB 494 6272 12
Total	0.00 CAD
Terms and Conditions	

INTRODUCTION

ELSEVIER LICENSE
TERMS AND CONDITIONS

Dec 13, 2023

This Agreement between Dalhousie University -- Ryan Callaghan ("You") and Elsevier ("Elsevier") consists of your license details and the terms and conditions provided by Elsevier and Copyright Clearance Center.

License Number	5687140416836
License date	Dec 13, 2023
Licensed Content Publisher	Elsevier
Licensed Content Publication	Applied Energy
Licensed Content Title	Experimental evaluation of commercial heat exchangers for use as PCM thermal storage systems
Licensed Content Author	M. Medrano,M.O. Yilmaz,M. Nogués,I. Martorell,Joan Roca,Luisa F. Cabeza
Licensed Content Date	Oct 1, 2009
Licensed Content Volume	86
Licensed Content Issue	10
Licensed Content Pages	9
Start Page	2047
End Page	2055

Type of Use	reuse in a thesis/dissertation
Portion	figures/tables/illustrations
Number of figures/tables/illustrations	1
Format	electronic
Are you the author of this Elsevier article?	No
Will you be translating?	No
Title of new work	EFFECT OF PCM SELECTION ON THE THERMAL PERFORMANCE OF A COIL-IN-SHELL STORAGE SYSTEM
Institution name	Dalhousie University
Expected presentation date	Dec 2023
Portions	table 2 page 2049
Requestor Location	Dalhousie University 5885 Spring Garden Road Apt. 1016 Halifax, NS B3H 1Y3 Canada Attn: Dalhousie University
Publisher Tax ID	GB 494 6272 12
Total	0.00 CAD
Terms and Conditions	

INTRODUCTION

ELSEVIER LICENSE
TERMS AND CONDITIONS

Dec 13, 2023

This Agreement between Dalhousie University -- Ryan Callaghan ("You") and Elsevier ("Elsevier") consists of your license details and the terms and conditions provided by Elsevier and Copyright Clearance Center.

License Number	5687130723395
License date	Dec 13, 2023
Licensed Content Publisher	Elsevier
Licensed Content Publication	Journal of Energy Storage
Licensed Content Title	Recent progress in phase change materials storage containers: Geometries, design considerations and heat transfer improvement methods
Licensed Content Author	Mohamed E. Zayed,Jun Zhao,Wenjia Li,Ammar H. Elsheikh,Ahmed Mohamed Elbanna,Liu Jing,A.E. Geweda
Licensed Content Date	Aug 1, 2020
Licensed Content Volume	30
Licensed Content Issue	n/a
Licensed Content Pages	1
Start Page	101341

End Page	0
Type of Use	reuse in a thesis/dissertation
Portion	figures/tables/illustrations
Number of figures/tables/illustrations	1
Format	electronic
Are you the author of this Elsevier article?	No
Will you be translating?	No
Title of new work	EFFECT OF PCM SELECTION ON THE THERMAL PERFORMANCE OF A COIL-IN-SHELL STORAGE SYSTEM
Institution name	Dalhousie University
Expected presentation date	Dec 2023
Portions	figure 1 page 2
Requestor Location	Dalhousie University 5885 Spring Garden Road Apt. 1016 Halifax, NS B3H 1Y3 Canada Attn: Dalhousie University
Publisher Tax ID	GB 494 6272 12
Total	0.00 CAD